STOCHASTIC AND DETERMINISTIC INVERSION METHODS FOR HISTORY MATCHING OF PRODUCTION AND TIME-LAPSE SEISMIC DATA

A Dissertation

by

SHINGO WATANABE

Submitted to the Office of Graduate and Professional Studies of
Texas A&M University
in partial fulfillment of the requirements for the degree of

DOCTOR OF PHILOSOPHY

Chair of Committee,	Akhil Datta-Gupta
Committee Members,	Michael J. King
	Eduardo Gildin
	Luc T. Ikelle
Head of Department,	A. Daniel Hill

December 2013

Major Subject: Petroleum Engineering

ABSTRACT

Automatic history matching methods utilize various kinds of inverse modeling techniques. In this dissertation, we examine ensemble Kalman filter as a stochastic approach for assimilating different types of production data and streamline-based inversion methods as a deterministic approach for integrating both production and time-lapse seismic data into high resolution reservoir models.

For the ensemble Kalman filter, we developed a physically motivated phase streamline-based covariance localization method to improve data assimilation performance while capturing geologic continuities that affect the flow dynamics and preserving model variability among the ensemble of models.

For the streamline-based inversion method, we derived saturation and pressure drop sensitivities with respect to reservoir properties along streamline trajectories and integrated time-lapse seismic derived saturation and pressure changes along with production data using a synthetic model and the Brugge field model. Our results show the importance of accounting for both saturation and pressure changes in the reservoir responses in order to constrain the history matching solutions.

Finally we demonstrated the practical feasibility of a proposed structured workflow for time-lapse seismic and production data integration through the Norne field application. Our proposed method follows a two-step approach: global and local model calibrations. In the global step, we reparameterize the field permeability heterogeneity with a Grid Connectivity-based Transformation with the basis coefficient as parameters and use a Pareto-based multi-objective evolutionary algorithm to integrate field cumulative production and time-lapse seismic derived acoustic impedance change data. The method generates a suite of trade-off solutions while fitting pro-

duction and seismic data. In the local step, first the time-lapse seismic data is integrated using the streamline-derived sensitivities of acoustic impedance with respect to reservoir permeability incorporating pressure and saturation effects in-between time-lapse seismic surveys. Next, well production data is integrated by using a generalized travel time inversion method to resolve fine-scale permeability variations between well locations.

After model calibration, we use the ensemble of history matched models in an optimal rate control strategy to maximize sweep and injection efficiency by equalizing flood front arrival times at all producers while accounting for geologic uncertainty. Our results show incremental improvement of ultimate recovery and NPV values.

DEDICATION

To the lord, who gives me strength through my life and is faithful to his promises of all my successes. Praise his glorious name forever. To my parents, who raised me and supported me unconditionally throughout my life. To my wife, who respects me and commits her life to me with all her love and trust in me.

ACKNOWLEDGEMENTS

I would like to express my sincere gratitude to my committee chair, Dr. Datta-Gupta for his academic guidance and financial support throughout the course of this research. His continuous encouragement and critical teaching assisted me to finish this PhD degree study. Also his generous support for industry opportunities through internship and conferences was extremely helpful for my future career.

I would also like to extend my sincere appreciation to my committee members: Dr. King, Dr. Gildin, and Dr. Ikelle for their thoughtful discussions and suggestions that improved the contents of this dissertation.

I would also like to extend my deepest gratitude to Dr. Arihara who recommended me for the graduate study at Texas A&M University with his trust in my successful completion.

Thanks also go to all the faculty and staff members of Harold Vance department of petroleum engineering for their outstanding graduate study education program and student supports. Especially, I appreciate Dr. Moridis for his scholarship to support my research work.

Special thanks to MCERI alumni and current students for their mentorship, partnership and friendship though my study life.

Also, I would like to thank Statoil (operator of the Norne field) and its license partners ENI and Petoro for the release of the Norne data. Further, I acknowledge the Center for integrated Operations at NTNU for cooperation and coordination of the Norne license partners.

Finally, thanks to my mother and father for their support and to my wife for her patience and love.

NOMENCLATURE

RB/D	Reservoir Barrel Per Day
Q_o	Standard Oil Production Rate
Q_g	Standard Gas Production Rate
$Q_{g,free}$	Reservoir Free Gas Production Rate
R_s	Solution Gas Ratio
k_{ro}	Oil Relative Permeability
k_{rg}	Gas Relative Permeability
μ_o	Oil Viscosity
μ_g	Gas Viscosity
B_o	Oil Formation Volume Factor
B_g	Gas Formation Volume Factor
RMS	Root Mean Square
OBS	Observation Data
OWC	Oil Water Contact
NPV	Net Present Value
N_p	Incremental Oil Production Volume

TABLE OF CONTENTS

Page

ABSTRACT ii

DEDICATION iv

ACKNOWLEDGEMENTS v

NOMENCLATURE vi

TABLE OF CONTENTS vii

LIST OF FIGURES x

LIST OF TABLES xvii

1. INTRODUCTION AND STUDY OBJECTIVES 1

    1.1 Reservoir Modeling 1
    1.2 History Matching 3
    1.3 Research Objectives and Dissertation Outline 5

2. USE OF PHASE STREAMLINES FOR COVARIANCE LOCALIZATION IN ENSEMBLE KALMAN FILTER FOR THREE-PHASE HISTORY MATCHING 6

    2.1 Summary 6
    2.2 Introduction 7
    2.3 Background and Methodology 11
        2.3.1 EnKF Formulation 11
        2.3.2 EnKF Forecast and Update 12
        2.3.3 Cross-Covariance Localization: Current Approaches 14
        2.3.4 Distance Dependent Localization 15
        2.3.5 Streamline-Based Localization 15
        2.3.6 Hierarchical Ensemble-Filter Localization 16
    2.4 Approach 17
        2.4.1 An Illustrative Example 18
        2.4.2 Spurious Correlations 20
        2.4.3 The Proposed Phase-Streamline-Based Localization and Its Validation 21

2.5 Applications . . . 28
2.5.1 Nine-Spot Synthetic Model . . . 28
2.5.2 Comparison of EnKF With and Without Localization . . . 29
2.5.3 PUNQ-Model Application . . . 40
2.6 Conclusions . . . 43

3. STREAMLINE-BASED TIME LAPSE SEISMIC DATA INTEGRATION INCORPORATING PRESSURE AND SATURATION EFFECTS . . . 48

3.1 Summary . . . 48
3.2 Introduction . . . 49
3.3 Background and Methodology . . . 56
3.3.1 Streamline-Based Data Integration: Literature Review . . . 57
3.3.2 Quantifying Data Misfit: Amplitude vs. Travel-Time Inversion 61
3.3.3 Time of Flight Sensitivity Calculation . . . 63
3.3.4 Saturation Front Arrival Time Sensitivity . . . 66
3.3.5 Generalized Travel Time Sensitivity . . . 67
3.3.6 Water Saturation Sensitivity Calculation . . . 68
3.3.7 Pressure Data Integration . . . 69
3.3.8 Pressure Drop Sensitivity Calculation . . . 70
3.3.9 Objective Function Minimization Formulation . . . 72
3.4 Sensitivity Calculation Validations . . . 73
3.4.1 Water Saturation Sensitivity Validation . . . 73
3.4.2 Pressure Drop Sensitivity Validation . . . 77
3.5 History Matching Applications . . . 79
3.5.1 Five-Spot Synthetic Case . . . 79
3.5.2 The Brugge Field Case . . . 85
3.6 Conclusions . . . 92

4. INTEGRATION OF 4D SEISMIC AND PRODUCTION DATA FOR RESERVOIR MANAGEMENT-APPLICATION TO THE NORNE FIELD 93

4.1 Summary . . . 93
4.2 Introduction . . . 94
4.3 Approach . . . 95
4.3.1 Petro-Elastic Model . . . 95
4.3.2 Seismic Data Processing . . . 99
4.3.3 Global to Local Hierarchical History Matching Workflow . . . 102
4.3.4 Time-Lapse Acoustic Impedance Change and Production Data Integration . . . 106
4.3.5 Streamline-Based Rate Optimization . . . 114
4.4 Conclusions . . . 121

5. CONCLUSIONS AND RECOMMENDATIONS 122

5.1 Conclusions 122
5.2 Recommendations 123

REFERENCES 126

APPENDIX A. WATER SATURATION CHANGE SENSITIVITY 138

APPENDIX B. TIME-LAPSE SEISMIC DATA ANALYSIS 140

B.1 Correlation 142
B.2 Phase Extension 145
B.3 The Signal-To-Noise Ratio 145
B.4 Norne Field Seismic Data Cross Correlation 148

APPENDIX C. SEISMIC DATA PROCESSING 153

LIST OF FIGURES

FIGURE Page

2.1 Homogeneous reference model and ensemble of realizations of permeability fields 19

2.2 Reference-model responses of water cut at producer (top left), bottomhole pressure at producer (top right), bottomhole pressure at injector (bottom left), and GOR at producer (bottom right) 20

2.3 Cross-covariance map comparisons with various ensemble sizes (20, 200, and 2,000 members from left). Permeability and bottomhole pressure of P1 at 300 days (top row), permeability and bottomhole pressure of I1 at 300 days (middle row), and permeability and water cut of P1 at 300 days (bottom row) 22

2.4 Cross-covariance map comparisons with various ensemble sizes (20, 200, and 2,000 members from left). Permeability and GOR of P1 at 300 days (top row), permeability and GOR of P1 at 750 days (middle row), and permeability and GOR of P1 at 1,350 days (bottom row) . 23

2.5 Cross-covariance map comparisons with ensemble size of 2,000 members at different times (300, 750, and 1,350 days, from top). From left, permeability and bottomhole pressure of P1, permeability and bottomhole pressure of I1, permeability and water cut of P1, and permeability and GOR of P1 25

2.6 Cross-covariance of permeability and GOR map, as well as pressure, gas-saturation, and water-saturation contour maps at different times (300, 600, 900, and 1,200 days, from left) 26

2.7 Cross-covariance of permeability and GOR map and gas-phase streamlines at different times (300, 600, 900, and 1,200 days, from left) . . . 26

2.8 Comparison of total-phase streamlines and gas-phase streamlines with cross-covariance of permeability and GOR map at different times (300, 600, and 1350 days, from left) 27

2.9 Heterogeneous reference model and ensemble realizations of permeability fields 29

2.10 True-model responses (red line) and initial-ensemble model response (gray lines) for water cut, bottomhole pressure, and GOR for three wells. (From left: P3, P5, and P7.) 30

2.11 History-matching comparisons of Plain EnKF and EnKF-PST. True-model response (red line) and initial- and updated ensemble model responses (gray lines) for water cut of P5, bottomhole pressure of P5, and GOR of P5 32

2.12 Updated permeability comparisons of Plain EnKF and EnKF-PST. True-model permeability field (top left) and three realizations of initial permeability fields (top row), Plain EnKF updated permeability fields (middle row), and EnKF-PST updated permeability fields (bottom row) 33

2.13 History-matching comparisons of EnKF-PST, EnKF-DT1 (Case 1), and EnKF-HC1 (Case 1). True-model response (red line) and updated-ensemble model responses (gray lines) for water cut of P5, bottomhole pressure of P5, and GOR of P5 35

2.14 Updated permeability comparisons of EnKF-PST, EnKF-DT1 (Case 1), and EnKF-HC1 (Case 1). True-model permeability field (top left) and three realizations of EnKF-PST updated permeability fields (top row), EnKF-DT1 updated permeability fields (middle row), and EnKF-HC1 updated permeability fields (bottom row) 36

2.15 Updated mean permeability histogram comparisons. From top left, true-model permeability field, initial model, and Plain EnKF are shown. From bottom left, EnKF-PST, EnKF-DT1 (Case 1), and EnKF-HC1 (Case 1) are shown 37

2.16 RMS of history-matching and forecasting comparisons of water cut (left), bottomhole pressure (right), and GOR (bottom). From left, initial models, Plain EnKF, EnKF-PST, EnKF-DT1 (Case 1), EnKF-DT2 (Case 2), EnKF-HC1 (Case 1), and EnKF-HC2 (Case 2) 38

2.17 Eigen spectrum of updated parameter-covariance matrix: Plain EnKF, EnKF-PST, EnKF-DT1 (Case 1), EnKF-DT2 (Case 2), EnKF-HC1 (Case 1), and EnKF-HC2 (Case 2), from top legend 38

2.18 Localization multiplier for EnKF-DT1 (Case 1), EnKF-HC1 (Case 1), and EnKF-PST. (a) Localization multiplier for cross-covariance of permeability and GOR of P1, P2, and P5 at 500 days. (b) Localization multiplier for cross-covariance of permeability and water cut of P1, P2, and P4 at 1,200 days 39

2.19 PUNQ-S3 model: (a) top-structure map (from Floris et al.) and (b) simulation model 41

2.20 Gas-phase streamlines at 181 days and 1,091 days (left) and water-phase streamlines at 1,091 days and 2,373 days (right). Coloring is with respect to the production well 41

2.21 History-matching comparison of Plain EnKF, EnKF-PST, and EnKF-DT. True-model response (red line) and initial- and updated-ensemble model responses (gray lines) for water cut of P4, bottomhole pressure of P12, and GOR of P1 43

2.22 RMS of history-matching and forecasting comparisons of water cut (top left), bottomhole pressure (top right), GOR (bottom left), and OPR (bottom right). (From left: initial models, Plain EnKF, EnKF-PST, and EnKF-DT 44

2.23 Updated-ensemble mean permeability comparisons of EnKF-PST and EnKF-DT for selected layers (from left: reference model, permeability field, EnKF-PST updated permeability fields, EnKF-DT with correlation length a=500 m updated permeability fields, and EnKF-DT1 with correlation length a=200 m updated permeability fields). 45

2.24 Updated-ensemble mean permeability histogram comparisons for EnKF-PST and EnKF-DT for selected layers (from left: reference-model permeability field, initial, and EnKF-PST updated permeability fields, EnKF-DT with correlation length a=500 m updated permeability fields, and EnKF-DT1 with correlation length a=200 m updated permeability fields) 45

3.1 Seismic data integration levels, (1) reservoir simulation level of data integration, (2) petro-elastic modeling level of data integration, and (3) seismic forward modeling level of data integration 53

3.2 Illustration of (a) travel-time inversion, (b) amplitude inversion, (c) generalized travel-time inversion, and (d) best time shift (from Cheng et al. 2005a) 64

3.3 A streamline between well pairs connecting gridblocks 70

3.4 A 1-D simulation model 73

3.5 Relative permeability curves 75

3.6 Water saturation sensitivity with respect to reservoir permeability comparisons. (a) Sensitivity values with respect to the permeability of gridblock no. 15 at a time of 25 days. Red line is the analytic streamline based calculation, green line is the numerical perturbation. (b) Water saturation profile at a time of 25 days. (c) Sensitivity values with respect to permeability of gridblock no. 15 at a time of 50 days. (d) Water saturation profile at a time of 50 days 76

3.7 Pressure drop sensitivity with respect to reservoir permeability comparisons. (a) Sensitivity values with respect to the permeability of gridblock no. 15 at a time of 25 days. Red line is the analytic streamline based calculation, green line is the numerical perturbation. (b) Pressure profile at a time of 25 days. (c) Sensitivity values with respect to permeability of gridblock no. 15 at a time of 50 days. (d) Water saturation profile at a time of 50 days 78

3.8 Five-spot permeability models. (a) Reference model, and (b) Initial model 80

3.9 Time-lapse observation data between 260 days and 1560 days. (a) Pressure change map, and (b) Water saturation change map 80

3.10 Objective functions during inversion iterations. (a) Pressure change data integration, (b) Saturation change data integration and (c) Generalized travel time production data integration 82

3.11 Updated permeability fields comparisons. (a) Reference model, (b) Initial model, and (c) After pressure change data integration, (d) After water saturation change data integration, and (e) Final model after generalized travel time production data integration 82

3.12 Time-lapse pressure change comparisons. (a) Reference model, (b) Initial model, and (c) After pressure change data integration, (d) After water saturation change data integration, and (e) Final model after generalized travel time production data integration 83

3.13 Time-lapse water saturation change comparisons. (a) Reference model, (b) Initial model, and (c) After pressure change data integration, (d) After water saturation change data integration, and (e) Final model after generalized travel time production data integration 83

3.14 Bottomhole pressure data history matching results. Reference model responses are plotted as dot points, initial model responses are in blue lines, and final updated model responses are in red lines 84

3.15 Water cut data history matching results. Reference model responses are plotted as dot points, initial model responses are in blue lines, and final updated model responses are in red lines 84

3.16 Structure of the Brugge field showing the elevation depth (in feet) and 30 wells: producers (red color), and injectors (blue color) 85

3.17 Four realizations of the selected layers: namely Realization 1, 33, 67, and 103 87

3.18 Time-lapse pressure and water saturation changes vertically averaged over the four reservoir zones (from top Scheld, Maas, Waal, and Schie formations) 87

3.19 Streamlines during the 10 years of production depicting reservoir flow dynamics: primary depletion (initial to 625 days) to secondary recovery with down-dip water injection (940 days to 10 years) 88

3.20 Objective functions during inversion iterations. (a) Pressure change data integration, (b) Saturation change data integration, and (c) Generalized travel time production data integration 88

3.21 Water cut data history matching results. Data misfit comparisons between the initial models and the final updated models for four realizations 89

3.22 Production data history matching comparisons between the initial model and the final updated model of realization No. 67 90

3.23 Four final updated models of the selected layers: namely realization 1, 33, 67, and 103 90

3.24 Time-lapse pressure change comparisons between initial models and final updated models (from Waal formation) 91

3.25 Time-lapse water saturation change comparisons between initial models and final updated models (from Wall formation) 91

4.1 Structure of the Norne field showing reservoir permeability 95

4.2 Acoustic impedance calculation sensitivity by PEM model in oil and water 2 phase system, (a) with respect to water saturation changes under a fixed pressure (270 bar) and (b) with respect to pressure changes under a fixed saturation value (Sw=0.5) 99

4.3 Time to depth data conversion. (a) Reservoir model intersected by the depth domain seismic amplitude inline and crossline slices, (b) the Inline slice with reservoir model layer horizons, and (c) the crossline slice with reservoir model layer horizons 100

4.4 The acoustic impedance log comparisons. The calculated acoustic impedance log (black) and the response extracted from the acoustic-impedance cube as a result of genetic inversion (red). 101

4.5 Acoustic impedance change data in an inline slice between 2003 and 2001 surveys from genetic inversion. Water oil contact interpretations are superimposed (red line is at 2001 survey and black line is at 2003 survey). The water saturation and pressure changes from the initial model are compared 101

4.6 Global to local hierarchical history matching workflow 104

4.7 Parameterization of the permeability multiplier field as the weighted linear combination of leading GCT basis vectors 105

4.8 Multi-objective function comparisons between initial models and the final models in the global step model calibration 106

4.9 Local step streamline-based model calibration workflow 108

4.10 The objective function misfit for acoustic impedance change data integration comparisons among the prior model, global step calibrated model, and the final updated model from the local step calibration . . 108

4.11 Water cut production data history matching comparisons between the initial model and the final updated model 109

4.12 Permeability model update comparison by layers. The prior model (Top), The final updated model (middle), and the model changes between the prior and the final models 110

4.13 Time-lapse acoustic impedance changes comparisons in selected layers among the observation data, the prior model responses and the final updated model responses 111

4.14 Time-lapse acoustic impedance changes between 2003 and 2004 comparisons in selected layers among the observation data, the prior model responses and the final updated model responses and corresponding pressure change responses 112

4.15 Time-lapse acoustic impedance changes between 2004 and 2006 comparisons in selected layers among the observation data, the prior model responses and the final updated model responses and corresponding gas saturation change responses 113

4.16 Streamline-based rate optimization under geologic uncertainty workflow 118

4.17 Rate optimization results: (a) ultimate recovery factor comparisons of base case and two optimized cases: $\eta = 0$ and $\eta = 100$, (b) final NPV comparisons of base case and two optimized cases: $\eta = 0$ and $\eta = 100$ 119

4.18 Rate optimization results: (a) NPV comparison with respect to optimization period for base case and two optimized cases: $\eta = 0$ and $\eta = 100$, (b) Incremental oil production comparison with respect to optimization period from base case and two optimized cases: $\eta = 0$ and $\eta = 100$ 120

4.19 Rate optimization results: Cumulative production rate comparison from each case 121

B.1 Geophysical models: (a) at baseline survey time, (b) at monitoring survey time, (c) differences between two survey times 141

B.2 Geophysical model responses: (a) baseline survey, (b) monitoring survey and (c) differences between two surveys 141

B.3 Geophysical model responses of differences between two surveys affected by different errors in the receiver positions: (a), (b), and (c) . . 142

B.4 Time delay between the baseline survey and the monitoring surveys affected by different errors in the receiver positions: (a), (b), and (c) . 144

B.5 The correlation energy between the baseline survey and the monitoring surveys affected by different errors in the receiver positions: (a), (b), and (c) 144

B.6 Different angle stacking data processing configurations 149

B.7 An inline slice of near-offset staked seismic amplitude data: (a) baseline survey at 2001, (b) monitoring survey at 2003 151

B.8 Cross correlation calculations of an inline slice of near-offset staked seismic amplitude data between baseline survey at 2001 and monitoring survey at 2003: (a) time delay (b) coherence correlation 152

LIST OF TABLES

TABLE Page

2.1 RMS of history-matching and forecasting comparisons in nine-spot model 35

2.2 RMS of history-matching and forecasting comparisons in the PUNQ model 44

3.1 Rock and fluid properties 74

3.2 Simulation specifications of saturation sensitivity validation case . . . 74

3.3 Simulation specifications of pressure sensitivity validation case 77

3.4 Rock and fluid properties 79

3.5 Simulation specifications of five-spot synthetic case 80

4.1 Input parameters for the petro-elastic model in Norne field 98

4.2 Economic parameters 114

4.3 Production constraints 114

4.4 Rate optimization results 120

1. INTRODUCTION AND STUDY OBJECTIVES

In this section, first reservoir modeling is generally described. Second, history matching problem is stated for the scope of this study. Finally, study objectives and the outline of this dissertation are summarized.

1.1 Reservoir Modeling

Reservoir modeling is an essential tool for petroleum engineers and geoscientists to approach to the uncertain subsurface phenomena. Under complex geological environment, one needs to rely on the numerical simulation to identify or visualize the flow dynamics in order to control or optimize the field production development.

Reservoir modeling usually begins with the exploration stage where seismic surveys search for the potential reservoir location with hydrocarbon trap structures in the subsurface. After the reservoir location and fluid types are identified from seismic images, the reservoir simulation grid domain will be defined. After a few wells are drilled in the early stage of production, local information such as well logging data and core data are integrated into the model to include the stratigraphic petrophysical properties such as rock permeability and porosity, the initial fluid saturation distributions, and the hydrostatic pressure and temperature gradient profiles. At this point the resolution of the grid needs to be determined because the scale of grid defines the simulation model size and the computation expense. Usually, the resolution of the geological model identified by seismic data and well log data are higher than computationally affordable resolution, we need to upscale the grid resolution in order to conduct flow simulation. At this stage, also the spatial petrophysical properties such as permeability and porosity values at each grid needs to be populated by utilizing geostatistical tools and conditioning the available data at well locations or

seismic derived data away from well locations. As PVT data and core analysis data becomes available from laboratory experiments, the rock and fluid properties such as relative permeability curves, fluid viscosity, and rock and fluid compressibility etc. are assigned in the reservoir model.

With the initial estimates of grid properties, rock and fluid properties and available reservoir condition data, we can initialize the reservoir equilibrium conditions which are the primary variables of flow simulation such as fluid pressures and saturations. After the production strategies are decided or planned, the boundary conditions of production rates and pressure constraints during the simulation are defined and finally one can conduct the reservoir simulation.

Over the decades of the development of reservoir simulation, variety of field-scale applications are possible to this date. Multi-phase/multi component flow simulation, geothermal simulation, CO_2 sequestration and chemical flooding, fractured reservoir and geomechanics coupling simulation are a few examples of field applications in practice. Also, recently more complex reservoir structure needs to be modeled such as mix of structure and unstructured grids, and this is becoming the current standard of the commercial simulators. With the advancement of the computer capability, the size of the model increases from multi-million cells to multi-billion-cells (Giga cell), and such simulation is currently feasible. High performance computing with the parallel processing and new solver algorithms also expand the capability of reservoir simulation to the computational limit. As the affordable simulation grid size increases, the scale of the spatial discretization approaches to the scale of geological model. The demand of coupling seismic data and reservoir simulation has been increasing and petroleum engineers and geoscientists need to collaborate tightly for developing the accurate reservoir characterization.

1.2 History Matching

History matching is a process of reservoir model calibration by reconciling the simulation responses to the actual field observation data. The aims of history matching are identifying the sensitive reservoir model parameters in order to match the model responses to the observation data such as production rates and pressure, reducing the uncertainty of the model descriptions, and increasing the accuracy of model predictions for the future field development. During the process of history matching, the previous reservoir modeling is continuously reviewed and vast amount of available data are utilized to eliminate uncertain model assumptions and modeling mistakes. This is a demanding process especially for the case of manual procedures of changing model parameters. Therefore computer guided workflows are necessary to reduce systematically the workload of the engineers in operational environment.

Over the decades of the inverse modeling development, various automatic history matching methods have been developed. To the best of the author's knowledge, the majority of methods are categorized broadly into three distinctive classes; deterministic and stochastic, and heuristic methods.

First, deterministic methods utilize the model sensitivity which quantifies the model changes to the model response changes and formulate the linearized equation to solve for the optimal model changes to minimize the misfit between observation data and simulation responses. Gradient descent is an example of this category. Second, stochastic methods utilize the probabilistic point of view to pose the minimization problem as maximizing a posterior probability from model prior probability with likelihood probability via Bayes' theorem. In the scope of reservoir history matching problem, we characterize prior model probability by using multiple reservoir models and likelihood will be estimated by each model responses with observation

data and select or update solutions to maximize the posterior probability by any statistical estimators. Monte Caro method is an example of this category. Third, heuristic methods utilize computational power to search for the best combinations of model parameters or to construct relationship between model parameters and model responses by linking input and output of reservoir simulation and alter the model parameters in a systematic way to reduce objective functions in the history matching problem. Genetic algorithm is one example of this category.

There are more variants of approaches in each category and hybrid ones between categories, but ultimately the objectives of history matching will determine which method is suitable, and both advantages and limitations of the selected method needs to be recognized. Some of general advantages and limitations of each category of method are as follows.

First, deterministic methods suffer from trapping at local minima of the solution space because the model sensitivity at local minima becomes zero and cannot improve solution from there. Also the computation of sensitivity calculation needs to be efficient to achieve fast history matching process. One advantage of deterministic approach is the ability of incorporating model physics into model calibration. As a result, the improvement of model can be justified by physical insights on model changes. Second, stochastic methods suffer from computation expenses for dealing with multiple reservoir simulation models. For a field scale model, one forward simulation time can be days or a week long and evaluations of multiple model response are computationally demanding. Also limiting the number of model size degrades sample statistics and fails to capture accurate posterior probability estimates. One advantage of stochastic method is that one can introduce the prior knowledge of the model with associated probabilities, and after calibration process, the suites of calibrated model are available and one can easily assess the uncertainty of the model

parameters and model predictions. As for heuristic methods, similar to stochastic methods, they will require computational expenses to search solutions in solution space. Therefore, identifying the sensitive parameters to model response is an important step to make the entire process efficient. One advantage of heuristic methods is the flexibility of the application. For example, one can apply the method to calibrate any parameters even for the situation in which the physics in the system is difficult or unknown.

1.3 Research Objectives and Dissertation Outline

This research focuses on developing efficient history matching methods for production data and 4-D seismic data. Specifically, the developments of automatic history matching methods are ensemble Kalman filter as the stochastic method and streamline-based inversion technique as the deterministic method. Main objectives of this research and corresponding sections of this dissertation are as follows.

- Develop and validate a phase streamline-based localization method of ensemble Kalman filter for history matching production data **(Section 2)**
- Develop and validate streamline-based fluid saturation and pore pressure sensitivity calculation algorithms and integrate seismic derived saturation and pressure map data into reservoir models **(Section 3)**
- Generate and validate acoustic impedance data by processing a real field seismic amplitude data and utilize a petro-elastic model to simulate acoustic impedance accounting for pressure and saturation effects **(Section 4)**
- Develop a structured workflow for a real field application of 4-D seismic and production history matching and apply the developed streamline-based inversion algorithms **(Section 4)**

2. USE OF PHASE STREAMLINES FOR COVARIANCE LOCALIZATION IN ENSEMBLE KALMAN FILTER FOR THREE-PHASE HISTORY MATCHING*

2.1 Summary

The ensemble Kalman filter (EnKF) has gained increased popularity for history matching and continuous reservoir-model updating. It is a sequential Monte Carlo approach that works with an ensemble of reservoir models. Specifically, the method uses cross-covariance between measurements and model parameters estimated from the ensemble. For practical field applications, the ensemble size needs to be kept small for computational efficiency. However, this leads to poor approximations of the cross-covariance and can cause loss of geologic realism from unrealistic model updates outside the region of the data influence and/or loss of variance leading to ensemble collapse. A common approach to remedy the situation is to limit the influence of the data through covariance localization.

In this study, we show that for three-phase-flow conditions, the region of covariance localization strongly depends on the underlying flow dynamics as well as on the particular data type that is being assimilated, for example, water cut or gas/oil ratio (GOR). This makes the traditional distance-based localizations suboptimal and, often, ineffective. Instead, we propose the use of water- and gas-phase streamlines as a means for covariance localization for water-cut and GOR data assimilation. The phase streamlines can be computed on the basis of individual phase velocities which are readily available after flow simulation. Unlike the total velocity stream-

*Part of this section is reprinted with permission from "Use of Phase Streamlines for Covariance Localization in Ensemble Kalman Filter for Three-Phase History Matching" by Watanabe, S., Datta-Gupta, A. 2012. SPE Reservoir Evaluation & Engineering **15** (3): 273-289. Copyright 2012 Society of Petroleum Engineers.

lines, phase streamlines can be discontinuous. We show that the discontinuities in water-phase and gas-phase streamlines naturally define the region of influence for water-cut and GOR data and provide a flow-relevant covariance localization during EnKF updating.

We first demonstrate the validity of the proposed localization approach using a waterflood example in a quarter-five-spot pattern. Specifically, we compare the phase streamline trajectories with cross-covariance maps computed using an ensemble size of 2,000 for both water-cut and GOR data. The results show a close correspondence between the time evolution of phase streamlines and the cross-covariance maps of water cut and GOR data. A small-size industrial reservoir engineering production forecasting with uncertainty quantification (the PUNQ-S3) (Floris et al. 2001) model application shows that our proposed localization outperforms a distance-based localization method. The updated models show improved forecasts while preserving geologic realism.

2.2 Introduction

There has been a great deal of progress in developing automatic history matching methods for reservoir characterization problem during the last couple of decades. A relatively recent development that combines the uncertainty in the reservoir description and the reservoir performance predictions is the Ensemble Kalman Filter (EnKF) (Evensen 1994). Although the amount of literature is overwhelming, the review of the method in the scope of petroleum engineering was recently published (Aanonsen et al. 2009).

In the EnKF framework, an ensemble of model realizations is progressively updated as the observation data becomes available using an assimilation sequence comprising of a forecast step that propagates the ensemble forward in time and an update

step that modifies the reservoir variables in order to match the current observations.

Although the EnKF has been applied to field-scale reservoir characterization and history matching studies (Nævdal et al. 2005; Skjervheim et al. 2007, Seiler et al. 2009, Chen and Oliver 2010a), there are several outstanding difficulties associated with the use of the EnKF. The cause of the difficulties roots from the severe non-linearity of the problem and non-uniqueness of the ill-posed inverse problem in general. Especially, in the context of history matching problem, Gaussian statistics is underlying assumption for updating models which can be violated in many situations for the reservoir characterization such as multi-modal multi-facies or channelized permeability distribution. Some reperameterization techniques were proposed to address this issue (Jafarpour and McLaughlin 2009; Sarma and Chen 2009).

Several authors have addressed the non-linearity issue and developed variants of EnKF such as iterative formulations (Gu and Oliver 2007; Li and Reynolds 2009) and a hybrid formulation (Watanabe et al. 2009). In this study, however, we use the conventional EnKF formulation to investigate the fundamental issue of inadequate estimation of cross-covariance because of small ensemble size. The results from this study also apply to other forms of EnKF.

The EnKF relies on an accurate representation of the ensemble-derived statistical measures, such as the cross-covariance between the reservoir responses (e.g. flow rates, bottomhole pressures, gas-oil ratios, and water cuts) and the reservoir variables (e.g. porosity and permeability) to update geological models. However, sampling error in the ensemble-based estimates can significantly degrade the quality of model updating, especially with modest ensemble sizes. As a consequence, the ensemble model responses can collapse towards a single response leading to 'ensemble collapse' and/or the final model responses deviate from the true model trajectory in a phenomenon known as 'filter divergence'. One approach to mitigate these effects

is through covariance localization (Houtekamer and Mitchell 1998).

The commonly applied 'Distance dependent localization' originated in the atmospheric science literature. Houtekamer and Mitchell (1998) first used a cutoff distance such that only the parameters within the specified distance of the observation were updated. In most practical applications, the distance dependent localization utilizes a fifth-order compactly supported correlation function of Gaspari and Cohn (1999) to eliminate spurious correlations far away from the observation points.

In reservoir characterization applications, Arroyo-Negrete et al. (2008) and Devegowda et al. (2010) introduced streamline-based localization approaches that utilize streamline trajectories to identify the region of 'influence' associated with the observed data. Such flow-relevant localization has been shown to naturally follow the prior geological model heterogeneity and the underlying displacement phenomena. By targeting and limiting the model updates, the streamline-based approach could also preserve the prior geological model characteristics and mitigate the parameter over and undershooting problems.

Anderson (2007) proposed a statistical localization approach based on a hierarchical ensemble Kalman filter. The goal here is to minimize the sampling error in the Kalman gain using 'groups' of ensembles that are used to estimate Kalman gain error. A minimization of the estimation error results in localization multipliers. One disadvantage of the approach is the computational cost for practical applications because of the need for multiple ensembles.

Previous studies on cross-covariance estimation with localization have been mostly limited to two phase flow conditions. Chen and Oliver (2010b) analyzed cross correlation profiles for different types and assimilation times in an attempt to define appropriate distance based localization functions. They concluded that distance based localization can eliminate spurious correlations with the knowledge of data sensitivity

and the prior covariance for model variables and the past history of data assimilation. However, no clear criterion was proposed to define an appropriate distance measure for localization under dynamic conditions. Emerick and Reynolds (2011) combined well drainage areas and prior covariance information to define localization for a two phase synthetic example. Their approach is related to the streamline-based localization approach; however, they artificially alter the well drainage regions, making the localization scheme inconsistent with the underlying flow dynamics.

In this study, we focus on three-phase data assimilation using EnKF. We show that for three phase flow conditions, the region of covariance localization strongly depends on the underlying flow dynamics and also, on the particular data type that is being assimilated viz. water cut or gas-oil ratio. This makes the traditional distance-based localizations suboptimal and often, ineffective. Unlike previous streamline-based localization that utilizes total velocity streamlines, we propose the use of water and gas phase streamlines as a means for covariance localization for water-cut and GOR data assimilation. The phase streamlines can be computed based on individual phase velocities which are readily available after flow simulation. Unlike the total velocity streamlines, phase streamlines can be discontinuous. We show that the discontinuities in water phase and gas phase streamlines naturally define the region of influence for water-cut and GOR data and provide a flow-relevant covariance localization during EnKF updating.

The outline of this section is as follows. First, we give mathematical background to introduce the EnKF formulation and brief descriptions of various localization methods. Second, we describe and validate our proposed localization approach by using an illustrative three-phase synthetic example. Finally, we apply EnKF history matching for a waterflood example and the benchmark PUNQ-S3 model (Floris et al. 2001). We compare different localization techniques and examine the performance of

each localization approach to demonstrate the utility and advantage of our proposed approach.

2.3 Background and Methodology

This section briefly discusses the EnKF formulation and introduces various localization methods. We first review the classical EnKF formulation and introduce the relevant terminologies. We then discuss localization approaches, mainly categorized into three groups: distance dependent localization, streamline-based localization, and statistically-derived localization or hierarchical EnKF.

2.3.1 EnKF Formulation

The EnKF, first introduced by Evensen (1994, 2003), is a sequential Monte Carlo technique for data assimilation. In the EnKF approach, an ensemble of model states is recursively conditioned to dynamic data as it becomes available. The details of the derivation of the EnKF can be found in Evensen (2006). Below, we will focus on some of the key features of the EnKF equations.

In the EnKF formulation, each ensemble member or realization is represented by a state vector, $\mathbf{y}_k$, at time k, and containing the following: a vector of static variables $\mathbf{m}_k^s$ (e.g. permeability, porosity) of length N_s, a vector of dynamic variables $\mathbf{m}_k^d$ (e.g. pressure, phase saturations) of length N_d, and a vector of model predictions $\mathbf{d}_k$ (e.g. bottomhole pressure, water cut and gas-oil ratio at the wells) of length M:

$$\mathbf{y}_k^p = \begin{bmatrix} \mathbf{m}_k^s \\ \mathbf{m}_k^d \\ \mathbf{d}_k \end{bmatrix}. \tag{2.1}$$

Here the superscript p denotes the prediction state. The model predictions at time k

is related to the state vector through the use of a measurement matrix, $\mathbf{H}$ as follows:

$$\mathbf{d}_k = \mathbf{H}\mathbf{y}_k^p. \tag{2.2}$$

Thus the mapping matrix $\mathbf{H}$ is a trivial matrix given by Eq. (2.3) as follows:

$$\mathbf{H} = \begin{bmatrix} \mathbf{0}_{N_s} & \mathbf{0}_{N_d} & \mathbf{I}_M \end{bmatrix}, \tag{2.3}$$

where $\mathbf{0}_{N_s}$ and $\mathbf{0}_{N_d}$ are zero matrix of size $M \times N_s$ and $M \times N_d$, and $\mathbf{I}_M$ is the identity matrix of size $M \times M$ respectively. The EnKF works with an ensemble of state vectors denoted as

$$\mathbf{\Psi}_k^p = \begin{bmatrix} \mathbf{y}_{k,1}^p & \mathbf{y}_{k,2}^p & \dots & \mathbf{y}_{k,N_e}^p \end{bmatrix}, \tag{2.4}$$

where N_e is the ensemble size. Each state vector represents an individual member of an infinite ensemble of possible states that are consistent with the initial measurements from cores, well-logs, seismic surveys and geologic interpretation studies.

2.3.2 EnKF Forecast and Update

The EnKF comprises of two main steps: a forecast step and an update step. The forecast step can be written as

$$\begin{bmatrix} \mathbf{m}_k^d \\ \mathbf{d}_k \end{bmatrix} = \mathrm{g}(\mathbf{m}_{k-1}^s, \mathbf{m}_{k-1}^d), \tag{2.5}$$

where the forward model operator g $(\circ)$ represents a numerical solution of the porous media fluid flow equations moving forward from time $k-1$ to time k when new observations become available. At this time, the update step modifies the reservoir state

vector for each ensemble member, $j = 1, 2, \ldots, N_e$, using the well-known Kalman update equation as follows (Evensen 2003):

$$\mathbf{y}_{k,j}^{u} = \mathbf{y}_{k,j}^{p} + \mathbf{K}_k(\mathbf{d}_{obs,k,j} - \mathbf{H}\mathbf{y}_{k,j}^{p}). \tag{2.6}$$

The superscript u denotes the updated model. The matrix $\mathbf{K}_k$ is known as the Kalman gain matrix and relates the data misfit to the changes required in the reservoir state vector. In Eq. (2.6), $\mathbf{d}_{obs,k,j}$ represents a vector of perturbed observations as defined by the following equation:

$$\mathbf{d}_{obs,k,j} = \mathbf{d}_{obs,k} + \boldsymbol{\varepsilon}_j, \tag{2.7}$$

where $\boldsymbol{\varepsilon}_j$ represents the noise in the observation for the ensemble member j. The noise associated with the measurements, $\boldsymbol{\varepsilon}$, is assumed to be Gaussian with a zero mean and covariance, $\mathbf{C_D}$. The Kalman gain matrix $\mathbf{K}_k$ is expressed as follows:

$$\mathbf{K}_k = \mathbf{C}_{\Psi,k}^{p}\mathbf{H}^{\top}(\mathbf{H}\mathbf{C}_{\Psi,k}^{p}\mathbf{H}^{\top} + \mathbf{C_D})^{-1}, \tag{2.8}$$

where $\mathbf{C}_{\Psi,k}^{p}$ represents an estimate of the state vector covariance matrix at time k and does not need to be computed from the ensemble explicitly. Instead, we compute the products of the cross-covariance matrix $\mathbf{C}_{\Psi,k}^{p}\mathbf{H}^{\top}$ and the prediction-error covariance matrix $\mathbf{H}\mathbf{C}_{\Psi,k}^{p}\mathbf{H}^{\top}$. From Eq. (2.8) in particular, it is obvious that EnKF updating is largely governed by the cross-covariance term $\mathbf{C}_{\Psi,k}^{p}\mathbf{H}^{\top}$, estimated from the ensemble by the following expression:

$$\mathbf{C}_{\Psi,k}^{p}\mathbf{H}^{\top} = \frac{1}{N_e - 1}\sum_{i,j=1}^{N_e}(\mathbf{y}_{k,i}^{p} - \overline{\mathbf{y}_k^{p}})(\mathbf{H}\mathbf{y}_{k,j}^{p} - \overline{\mathbf{H}\mathbf{y}_k^{p}}) \tag{2.9}$$

where

$$\overline{\mathbf{y}_k^p} = \frac{1}{N_e}\sum_{j=1}^{N_e}\mathbf{y}_{k,j}^p \tag{2.10}$$

and

$$\overline{\mathbf{H}\mathbf{y}_k^p} = \frac{1}{N_e}\sum_{j=1}^{N_e}\mathbf{H}\mathbf{y}_{k,j}^p. \tag{2.11}$$

2.3.3 Cross-Covariance Localization: Current Approaches

The main aim of covariance localization schemes is to eliminate spurious terms in the cross-covariance matrix arising from sampling errors caused by finite and small ensemble sizes and to increase the effective number of ensemble members (Hamill et al. 2001). In the absence of localization, the covariance matrix is rank deficient which leads to the spurious correlation and the loss of variance (ensemble collapse). Mathematically, the EnKF update equation with covariance localization can be expressed on the basis of Eq. (2.6) as

$$\mathbf{y}_{k,j}^u = \mathbf{y}_{k,j}^p + (\boldsymbol{\rho} \circ \mathbf{C}_{\Psi,k}^p\mathbf{H}^\top)(\mathbf{H}\mathbf{C}_{\Psi,k}^p\mathbf{H}^\top + \mathbf{C}_\mathbf{D})^{-1}(\mathbf{d}_{obs,k,j} - \mathbf{H}\mathbf{y}_{k,j}^p). \tag{2.12}$$

where the localizing function $\boldsymbol{\rho}$ operates on the cross-covariance matrix. The operator ($\circ$) is an element-by-element multiplication also called the 'Schur product'. The various localization functions differ in the way we calculate this multiplier $\boldsymbol{\rho}$. In this study we investigate three categories of localization methods: distance dependent localization, streamline-based localization and statistically derived hierarchical localization methods. It is worthwhile to mention that in the absence of covariance localization, the solution from the EnKF updating is restricted to a linear combination of the initial ensemble members (Evensen 2003). However, with covariance localization as in Eq. (2.12), a much larger basis can be accessed and the solution

is no longer limited to a linear combination of the initial members (Evensen 2003). Brief descriptions of each localization method are next.

2.3.4 Distance Dependent Localization

Distance based covariance localization schemes (Houtekamer and Mitchell 2001; Hamill et al. 2001) rely on the assumption that the correlation between model grid cells and well observation data is a function of the distance between the grid cell and the observation location. Various distance-based correlation functions have been discussed by Gaspari and Cohn (1996). In this study, we have used the following form of the localization function:

$$\Omega(a,b) = \begin{cases} -\frac{1}{4}\left(\frac{b}{a}\right)^5 + \frac{1}{2}\left(\frac{b}{a}\right)^4 + \frac{5}{8}\left(\frac{b}{a}\right)^3 - \frac{5}{3}\left(\frac{b}{a}\right)^2 + 1, & 0 \le b \le a; \\ \frac{1}{12}\left(\frac{b}{a}\right)^5 - \frac{1}{2}\left(\frac{b}{a}\right)^4 + \frac{5}{8}\left(\frac{b}{a}\right)^3 + \frac{5}{3}\left(\frac{b}{a}\right)^2 - 5\left(\frac{b}{a}\right) + 4 - \frac{2}{3}\left(\frac{b}{a}\right)^{-1}, & a < b \le 2a; \\ 0, & b > 2a. \end{cases} \tag{2.13}$$

where $a = \sqrt{10/3}l_c$, l_c is a length scale, and b is a distance between an observation point and a grid point (i, j).

2.3.5 Streamline-Based Localization

The assumption that correlation solely depends on the distances is not appropriate for reservoirs with strong underlying heterogeneity that often dominates the flow dynamics. To account for the flow dynamics, Arroyo-Negrete et al. (2008) proposed a streamline based localization method. The basic idea is utilize the streamline trajectories derived from the total velocities (sum of phase velocities) which are

naturally obtained as part of the forward flow simulation. To identify the localization region for a given well data at a given time, only the streamlines leading to the well at the time of interest are considered. The localization region now consists of the grid cells intersected by these streamlines. A common localization region is defined for all ensemble members by the intersection of the localization regions of all individual members. The covariance calculations are limited to the localization region only.

Devegowda et al. (2010) extended the streamline trajectory based localization by defining a weighting function that relies on the magnitude of the parameter sensitivity values derived analytically from the streamline formulations (Vasco et al. 1999; He et al. 2002; Cheng et al. 2007; Datta-Gupta and King 2007; Oyerinde et al. 2009).

We can trace streamline trajectories from any finite difference simulator by extracting the flux information. All these previous works on streamline-based localization have utilized the total flux (sum of all phase fluxes) to trace the streamline trajectories. The advantage of using the total flux is that the streamline trajectories are continuous. In this work, we will utilize phase streamlines which are trajectories obtained based on individual phase fluxes. Thus, there will be a set of streamlines for each individual phase (Kumar et al. 2009).

2.3.6 Hierarchical Ensemble-Filter Localization

Anderson (2007) proposed a hierarchical ensemble filter which estimates sampling errors in Kalman gain matrix from a group of N_g ensemble and compute a regression confidence (weighting) factor α_n between 0 and 1 to minimize sampling error at each assimilation timestep n. The factor α_n is defined to minimize the expected root mean

square (RMS) difference in Kalman gain amongst the group as

$$\textbf{min } O(\alpha_n) = \textbf{min} \sqrt{\sum_{l=1}^{N_g} \sum_{\substack{k=l \\ k \neq l}}^{N_g} (\alpha_n K_k - K_l)^2}, \tag{2.14}$$

where K_k is an element of the Kalman gain matrix for the k th group at time n. This minimization results in the following:

$$\alpha_{min,n} = \textbf{max}\Big(\Big\{\Big[\Big(\sum_{i=1}^{N_g} K_i\Big)^2 / \Big(\sum_{i=1}^{N_g} K_i^2\Big)\Big] - 1\Big\}/(N_g - 1), 0\Big). \tag{2.15}$$

The localization multiplier matrix $\boldsymbol{\rho}$ is constructed element by element using $\alpha_{min,n}$. The modified Kalman update for each group of the ensemble is given as

$$\mathbf{y}_{k,j}^u(i) = \mathbf{y}_{k,j}^p(i) + (\boldsymbol{\rho} \circ \mathbf{K}_k)(\mathbf{d}_{obs,k,j} - \mathbf{H}\mathbf{y}_{k,j}^p(i)). \tag{2.16}$$

where $i = 1, 2, \ldots, N_g$ and the localization multiplier is acting not on the cross-covariance but on the Kalman gain matrix directly.

2.4 Approach

Main objectives of our proposed localization scheme are summarized as follows:

- Eliminating spurious cross correlation calculations arising from small ensemble statistics
- Localizing the observation data to regions that are based on flow dynamics
- Preserving geological realism through targeted parameter updating
- Maintaining model variability and preventing ensemble collapse and filter divergence

The major steps in our proposed approach are outlined as follows:

- **Ensemble Prediction Step.** Given an ensemble of static reservoir simulation model realizations generated from prior geologic information and/or geostatistical analysis, we conduct reservoir simulation on each of ensemble member up to the next available observation time. The outcome of this step is the predictions of the observed data from each ensemble member.

- **Phase Streamline Tracing.** Based on each ensemble member forward simulation results, we extract individual phase fluxes for each gridblock. Utilizing the phase fluxes at the gridblock faces, we trace phase streamline trajectories for water, oil and gas phases. For streamline tracing, we have used the algorithm proposed by Jimenez et al. (2007) for its ease of implementation and applicability to corner point grids. The streamline trajectories from each ensemble member are stored and used to identify the flow relevant regions contributing to the observed data at the current time for localization purposes.

- **Localizing Cross-Covariance Matrix.** Using the ensemble model predictions, model parameters and the flow relevant regions identified by the phase streamline trajectories, we compute the cross-covariance matrix only for the localized gridblocks.

- **Ensemble Correction Step.** Finally, we update the ensemble members using the localized cross-covariance matrix and the Kalman update equation. We repeat all steps for the next available observation data.

2.4.1 An Illustrative Example

This section illustrates the importance of covariance localization for EnKF using a simple two dimensional homogeneous reservoir model with a mesh size of 21×21

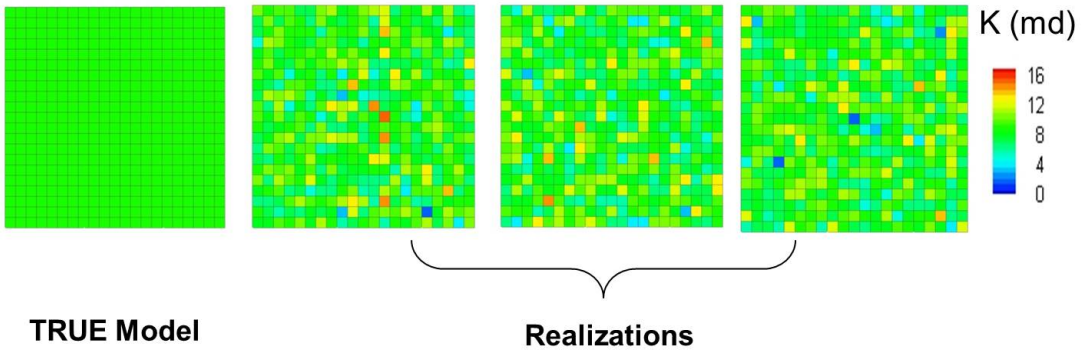

Fig. 2.1—Homogeneous reference model and ensemble of realizations of permeability fields.

having permeability of 8.12 md and porosity of 0.1 as shown in **Fig. 2.1**. To generate the initial ensemble of realizations, the permeability at each gridblock is perturbed with an uncorrelated Gaussian noise having variance of 2 md. We generate a total of 2,000 realizations. Some realizations are shown in Fig. 2.1. This set of 2,000 realizations will constitute our reference case with which we will compare various other ensemble sizes for the following numerical experiments.

As an initial condition, the reservoir is saturated with oil at the bubble point pressure of 3,000 psi. A quarter five-spot well configuration with an injector and a producer is used for this example. The wells are controlled by reservoir rate constraints with a production rate of 50 RB/D and an injection rate of 45 RB/D. Our goal is to create three-phase flow conditions by causing the reservoir pressure to decline because of the excess production, resulting in the liberation of the solution gas. The simulation timestep is fixed as 150 days for the total of 1,500 days. The reference model responses are shown in **Fig. 2.2**.

In Fig. 2.2, we have the water breakthrough at approximately 250 days and water cut increases as production proceeds. A comparison of the bottomhole pressure and

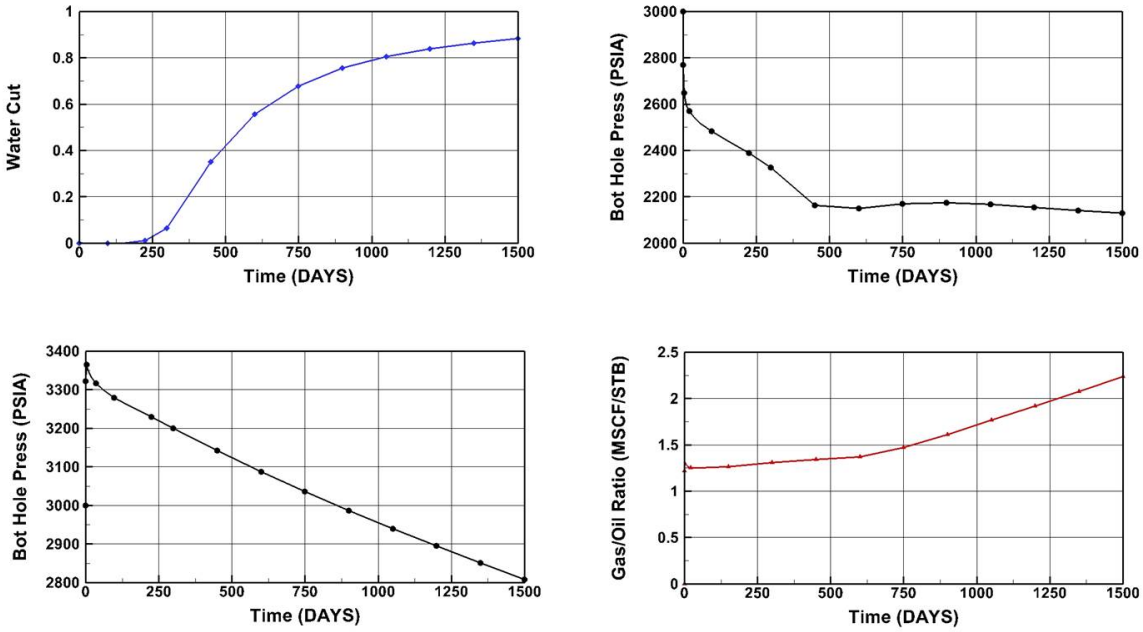

Fig. 2.2—Reference-model responses of water cut at producer (top left), bottomhole pressure at producer (top right), bottomhole pressure at injector (bottom left), and GOR at producer (bottom right).

GOR responses indicates that in the early period of production, the gas production is mainly from the dissolved gas from the oil production and results in a flat value of the response. Once the free gas evolves in the reservoir, the gas production is from both the dissolved-gas and the free-gas volume that results in increasing GOR.

2.4.2 Spurious Correlations

The fundamental problem of the EnKF that we address here is the accuracy of the cross-correlation calculations with respect to the ensemble size. Specifically, we examine the quality of the sample cross-covariance calculations between the gridblock permeabilities and three different observation data types, (e.g., water cut, bottomhole pressure and GOR) by changing the ensemble size.

The cross-covariance map is calculated at every assimilation step of the EnKF.

From these, we select 3 times for comparison purposes: early time (300 days), intermediate time (750 days), and late time (1,350 days). The cross-covariance is computed by the standard statistical means using the ensemble members and the model predictions in Eq. (2.9). We varied the ensemble size to be 20, 200 and 2,000 members and the results are shown in **Figs. 2.3 and 2.4**.

Fig. 2.3 shows that the bottomhole pressure and water-cut covariance shows a severe degradation for the ensemble size of 20 members. This is obvious when we compare it with the results from 2,000 members (the reference case). The 20-member results show significant spurious correlations and fail to capture much of the dominant characteristics of the reference case. If we apply this cross-covariance in the Kalman update, the updating will result in parameter over- and undershooting (Arroyo-Negrete et al. 2008). The 200-member case shows some correspondence in the spatial features with the 2,000-member reference case. However, there are still spurious correlations away from production and injection wells for the bottomhole-pressure covariance, and the water-cut covariance is not well defined as in the case of 2,000 members. As for the GOR correlations in Fig. 2.4, similar characteristics are observed with changing ensemble size, although the profile of the correlation is quite different from ones in water cut and bottomhole pressure. The role of covariance localization is to eliminate these spurious correlation calculations while capturing the dominant characteristics of the data influence.

2.4.3 The Proposed Phase-Streamline-Based Localization and Its Validation

Our validation of the proposed phase-streamline-based localization starts by examining the characteristics of the cross-correlation between permeability distribution and different data types: water cut, bottomhole pressure, and GOR. For this, we review the cross-covariance computed for the 2,000-member case for the synthetic example

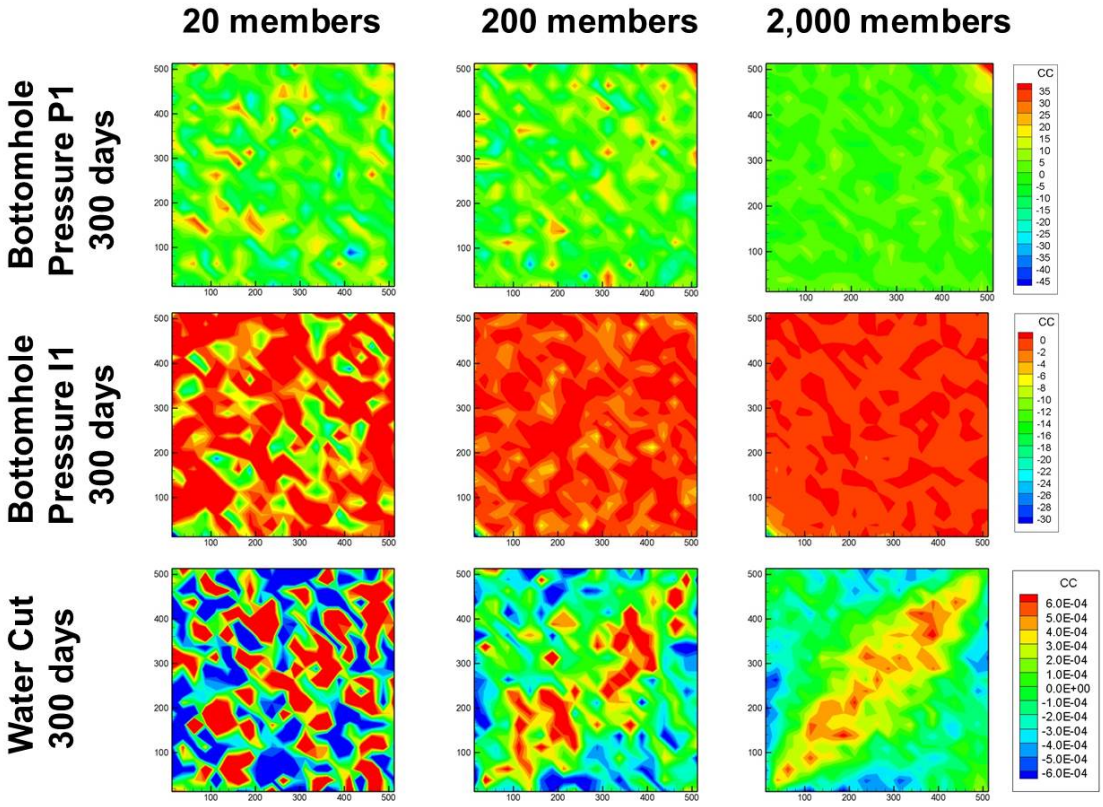

Fig. 2.3—Cross-covariance map comparisons with various ensemble sizes (20, 200, and 2,000 members from left). Permeability and bottomhole pressure of P1 at 300 days (top row), permeability and bottomhole pressure of I1 at 300 days (middle row), and permeability and water cut of P1 at 300 days (bottom row).

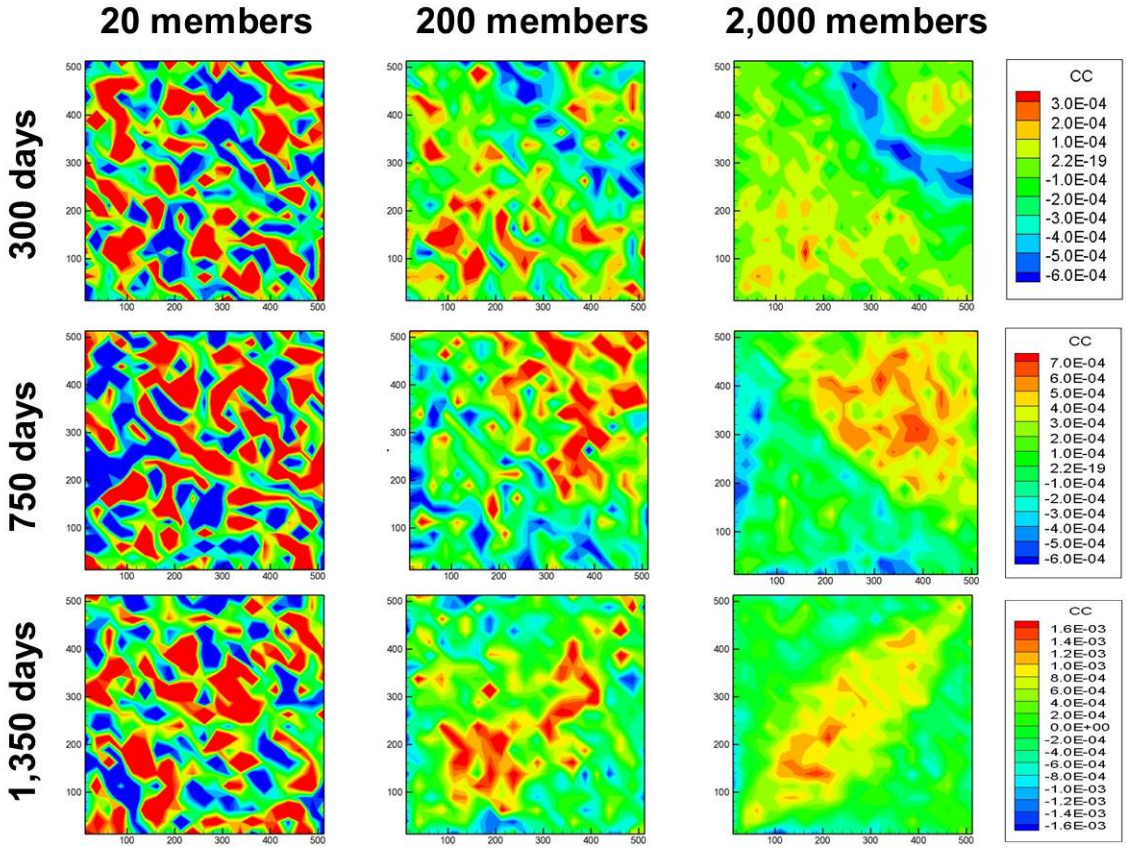

Fig. 2.4—Cross-covariance map comparisons with various ensemble sizes (20, 200, and 2,000 members from left). Permeability and GOR of P1 at 300 days (top row), permeability and GOR of P1 at 750 days (middle row), and permeability and GOR of P1 at 1,350 days (bottom row).

discussed before (**Fig. 2.5**). The results show that the bottomhole-pressure and permeability-correlation profiles are mostly concentrated in the vicinity of the observation wells and do not change significantly over time. The water-cut correlation shows positive values along the diagonal direction between injector and producer wells.

The GOR-correlation profile is more complex and contains transitions over time. At early times, there is a negative correlation band moving radially outward. The inside and outside of the band have positive correlation values. To explain this correlation profile, we examine the corresponding pressure and saturation profiles shown in **Fig. 2.6**. Also, recall that the GOR is calculated by

$$GOR = \frac{Q_g}{Q_o} = \frac{Q_{g,free} + R_s Q_o}{Q_o} = \frac{Q_{g,free}}{Q_o} + R_s = \frac{k_{rg}\mu_o B_o}{k_{ro}\mu_g B_g} + R_s. \tag{2.17}$$

Inside the positive-correlation region near the production well, free mobile gas exists because the pressure has fallen below the bubble point pressure of 3,000 psi. Thus, the increasing permeability in this region results in increasing free-gas production and increased GOR; hence, the correlation is positive. Fig. 2.6 reveals that the negative-correlation band approximately corresponds to a gas-saturation contour of 0.03. This value is the critical gas saturation in this example. Thus, the negative-correlation band is located at the boundary of the mobile and immobile gas. Increasing the permeability in this region induces faster oil flow, and oil production will increase relative to gas production. Therefore, the correlation is negative. Outside the negative-correlation band toward the injection well, we have only oil and water phases mobile, and increasing permeability results in preferential water displacement followed by reduced oil production relative to gas production. This produces the positive correlation outside the band. As production proceeds, the location

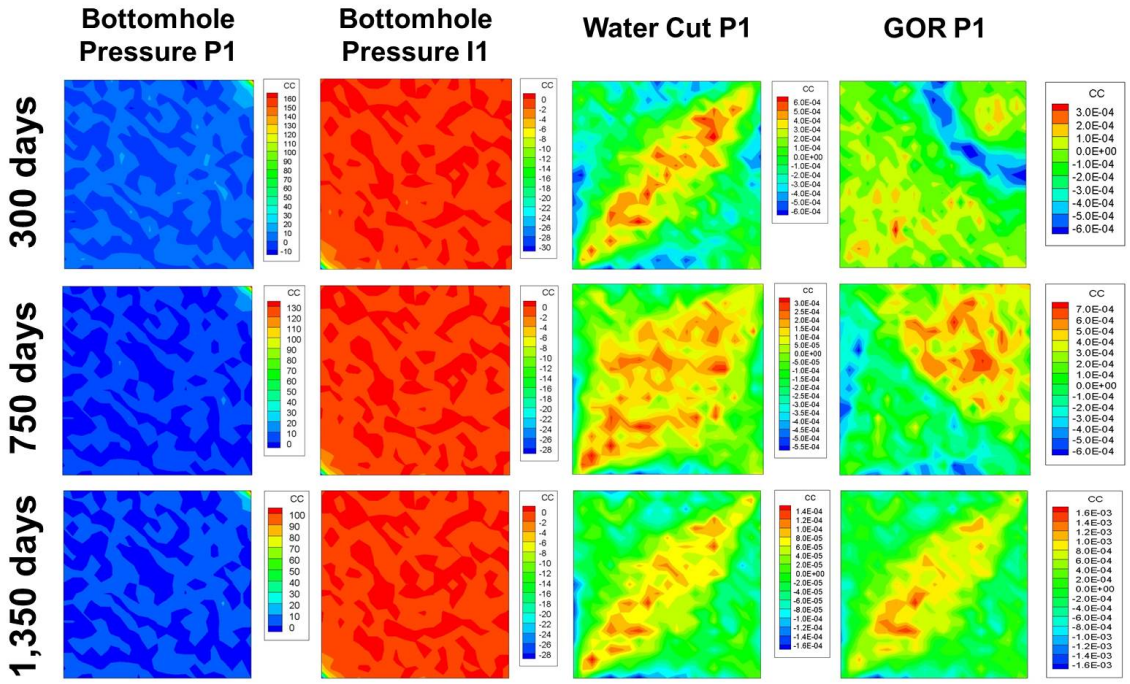

Fig. 2.5—Cross-covariance map comparisons with ensemble size of 2,000 members at different times (300, 750, and 1,350 days, from top). From left, permeability and bottomhole pressure of P1, permeability and bottomhole pressure of I1, permeability and water cut of P1, and permeability and GOR of P1.

of the negative band moves toward the injector, because the boundary between the mobile and immobile gas propagates toward the injector. By the time the mobile-gas saturation appears everywhere (within 1,200 days), the negative-correlation band no longer exists and the GOR-correlation profile shows close correspondence with that of water cut, because the flow regime becomes free-gas convective transport along preferential paths between wells.

Finally, if we compare the GOR-correlation map with the gas-phase streamlines shown in **Fig. 2.7**, we can clearly identify the correspondence between the area covered by gas-phase streamline trajectories and the progression of the location of

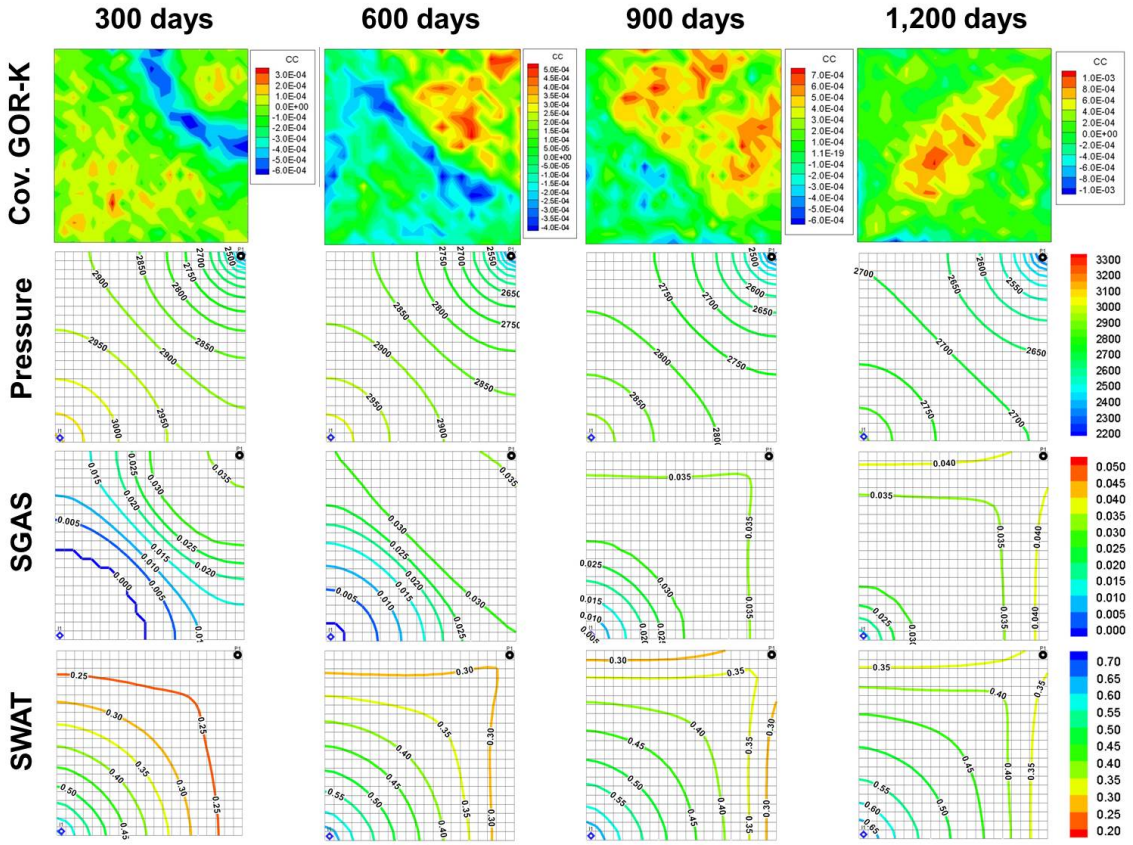

Fig. 2.6—Cross-covariance of permeability and GOR map, as well as pressure, gas-saturation, and water-saturation contour maps at different times (300, 600, 900, and 1,200 days, from left).

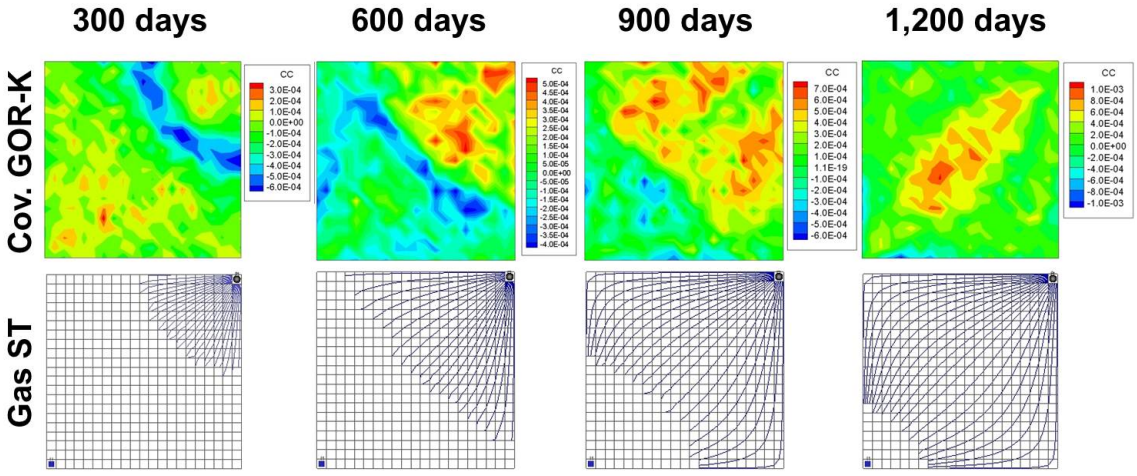

Fig. 2.7—Cross-covariance of permeability and GOR map and gas-phase streamlines at different times (300, 600, 900, and 1,200 days, from left).

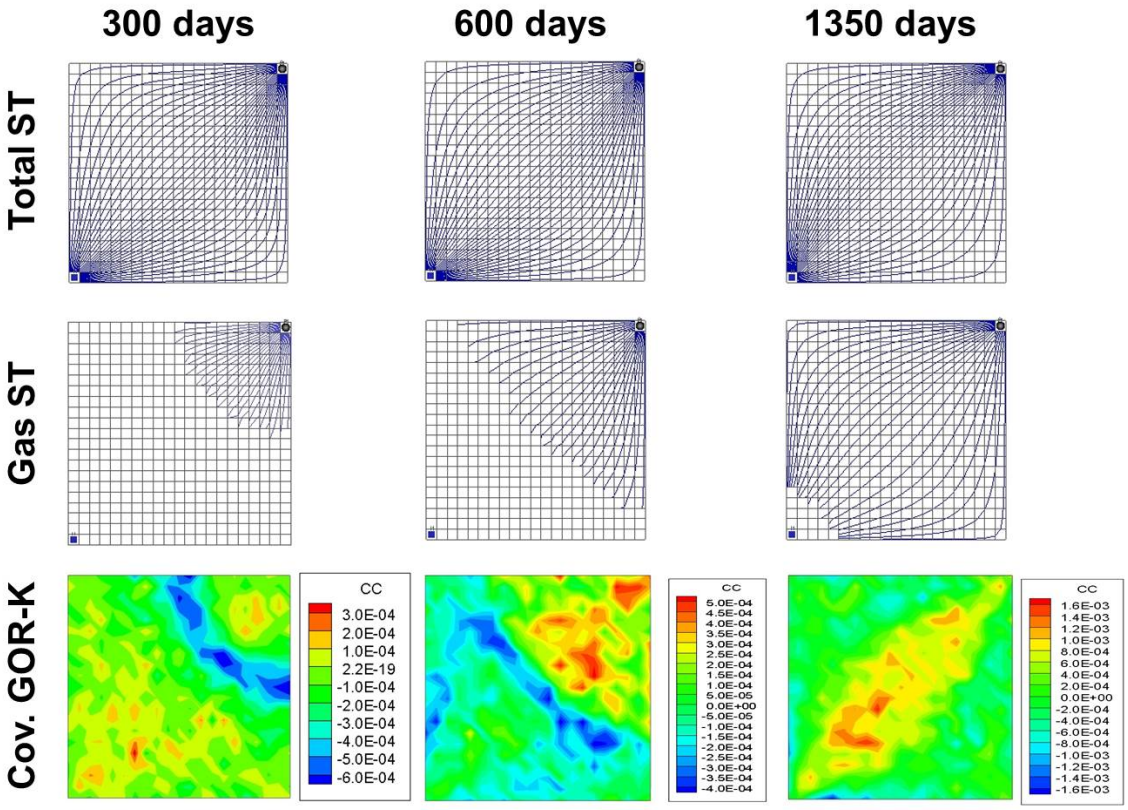

Fig. 2.8—Comparison of total-phase streamlines and gas-phase streamlines with cross-covariance of permeability and GOR map at different times (300, 600, and 1350 days, from left).

the negative correlation band over time. This is because the gas-phase streamlines are traced naturally from the producer to the boundary between the mobile- and immobile-gas saturations. For comparison purposes, we have shown in **Fig. 2.8** the total velocity streamlines as well as the gas-phase streamlines at different times. The total velocity streamlines cover the entire region between the injector and producer at all times, and they do not capture the correspondence with the cross-covariance profile as seen with the gas-phase streamlines (Fig. 2.8). This is the primary motivation in using phase streamlines for localization as opposed to the total velocity streamlines, as was done in our previous studies (Arroyo-Negrete et al. 2008).

2.5 Applications

In this section, we first present a comprehensive comparison of various localization methods using a nine-spot waterflooding example with three-phase-flow conditions. This example highlights the benefits of using phase-streamline localization over other localization methods. A variety of quality checks of the EnKF performance is presented to compare the localization methods. We also demonstrate the power and practical feasibility of the phase-streamline localization approach using a field-scale three-phase history-matching application.

2.5.1 Nine-Spot Synthetic Model

A heterogeneous reference synthetic model was generated by sequential Gaussian simulation (Deutsch and Journel 1992) with high-permeability continuity and a prior anisotropy direction, as shown in **Fig. 2.9**. The reservoir model domain is discretized into 51×51 gridblocks ($1{,}530 \times 1{,}530$ ft.) with eight producers and one injector in a nine-spot well pattern, as shown in Fig. 2.9. Similar to the previously discussed example, three-phase-flow conditions are set up by starting with undersaturated conditions and letting the reservoir pressure fall below the bubble point pressure.

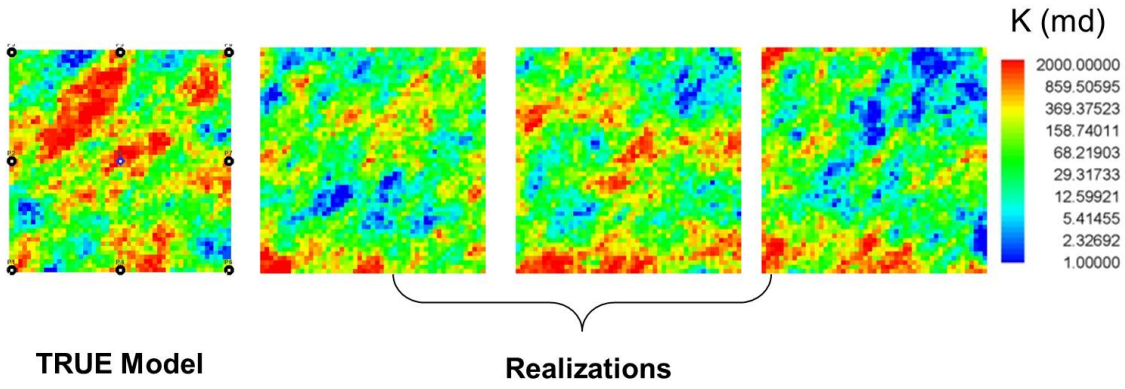

Fig. 2.9—Heterogeneous reference model and ensemble realizations of permeability fields.

The total simulation time is 4,000 days, which is split into the assimilation period of 2,000 days and the prediction period for the rest. Observation data are water cut, bottomhole pressure, and GOR. The data are assimilated at every 50 days for 40 time intervals. For EnKF, we used 50 ensemble members. Some examples of the initial members are shown in Fig. 2.9. The initial ensemble model predictions are shown in **Fig. 2.10** as gray lines and are compared with the reference-model response denoted as a red line in the figures.

2.5.2 Comparison of EnKF With and Without Localization

We conduct the EnKF with and without localizations for this synthetic case, and compare their performances.

First, we examine the distance-based localization, the most commonly used method in the literature. Because we generally do not have prior knowledge of the correlation distance, we examine two choices for a in Eq. (2.13) for the localization function: (Case 1) water cut=1,000 ft., bottomhole pressure=100 ft., GOR=1,000 ft.; (Case 2) water cut=300 ft., bottomhole pressure=100 ft., GOR=300 ft.. Our rationale for

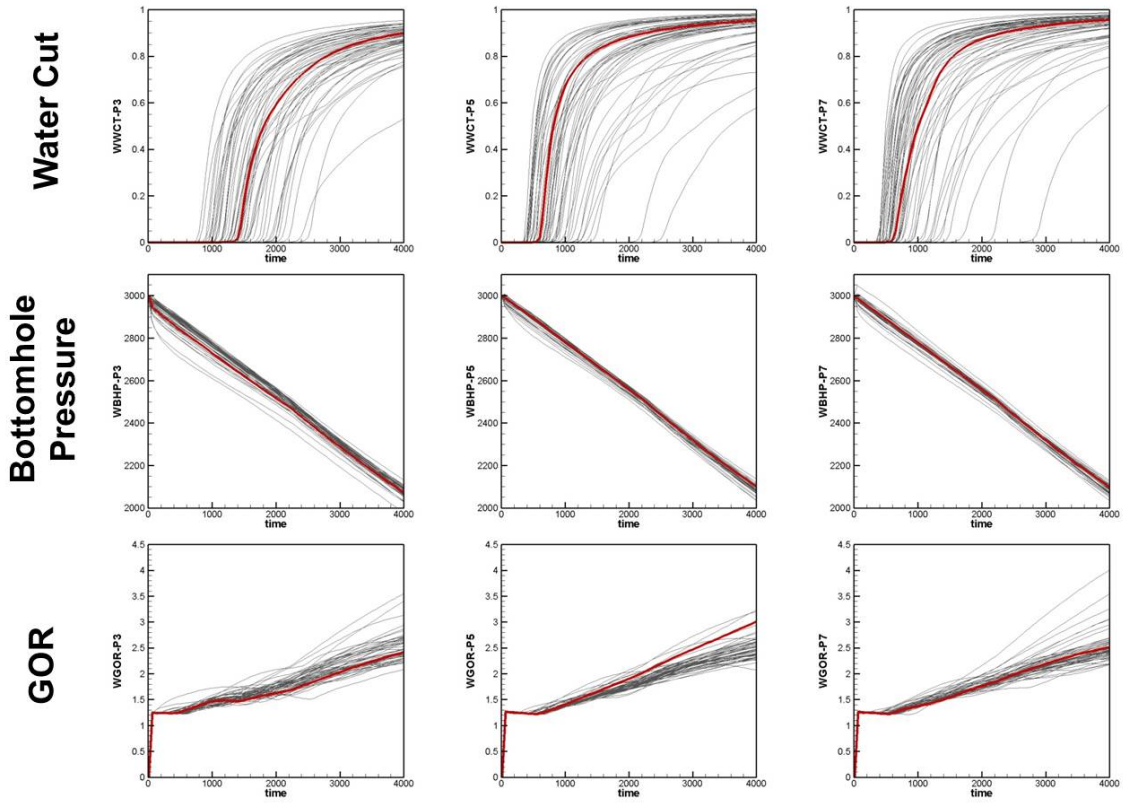

Fig. 2.10—True-model responses (red line) and initial-ensemble model response (gray lines) for water cut, bottomhole pressure, and GOR for three wells. (From left: P3, P5, and P7.)

these values is based on the previous observation that bottomhole-pressure-data influence is mainly near the well locations, and water-cut and GOR data cross-correlation tends to cover the region between the well-pair configuration.

For hierarchical EnKF, we also experiment with combinations of the number of ensemble group and the subensemble member size for two cases with a total ensemble size of 200 members: (Case 1) 10 groups of 20 members; (Case 2) four groups of 50 members. For the phase-streamline-based localization, we define a localization region for each observation data type for each ensemble member. Unlike the total-streamline-based approach (Arroyo-Negrete et al. 2008), the localization region now varies for each data type (e.g., water cut, GOR) on the basis of the intersection of the phase streamlines with the grid cells at the time of interest. A common localization region is defined by the intersection of the localization regions of all individual members, and we require that a grid cell intersected by phase streamlines for a minimum of 10 % of the total ensemble members to be included in the common localization region.

In the results that follow, we denote the conventional EnKF as Plain EnKF, while EnKF with localizations are denoted as follows: distance-dependent localization as EnKF-DT1 for Case 1 and EnKF-DT2 for Case 2; hierarchical EnKF as EnKF-HC1 for Case 1 and EnKF-HC2 for Case 2; and phase-streamline-based localization as EnKF-PST. The water-cut, bottomhole-pressure, and GOR history-matching comparisons for the Plain EnKF and EnKF-PST are shown in **Fig. 2.11**. The Plain EnKF shows evidence of ensemble collapse. Also, the GOR predictions for P5 show a systematic bias. The EnKF-PST results show reduced spread in model responses from the initial models and no systematic bias for the prediction period. The updated permeability fields are shown in **Fig. 2.12**. The Plain EnKF clearly results in ensemble collapse, where all ensemble models became almost identical. The EnKF-

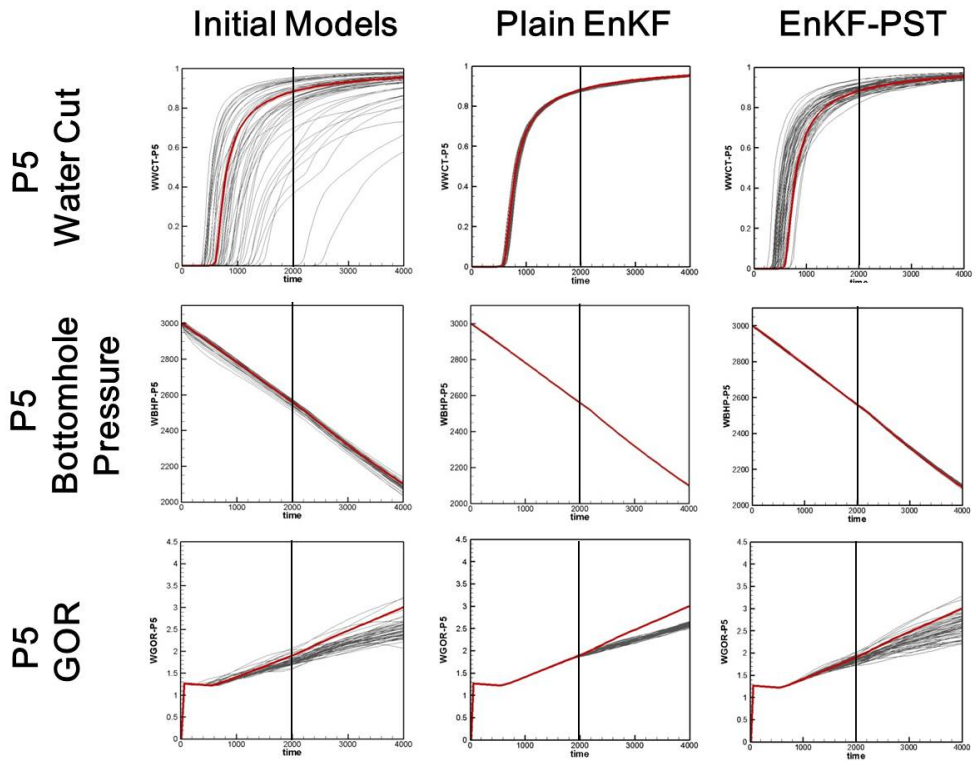

Fig. 2.11—History-matching comparisons of Plain EnKF and EnKF-PST. True-model response (red line) and initial- and updated ensemble model responses (gray lines) for water cut of P5, bottomhole pressure of P5, and GOR of P5.

PST updated ensemble models retain the variability of the permeability distribution and capture the high-permeability streak in the left upper corner.

For various localization methods, the history-match results are shown in **Fig. 2.13**, and the updated permeability fields are shown in **Fig. 2.14**. For history-matching comparisons, we consider both matching of the data and the prediction quality for computing the misfit from the true-model response in terms of RMS for the entire simulation period of 4,000 days. **Fig. 2.15** compares the ensemble mean log-permeability histograms for various localizations. The RMS error summary is listed in **Table 2.1** and shown in **Fig. 2.16**. Overall, the RMS error results show

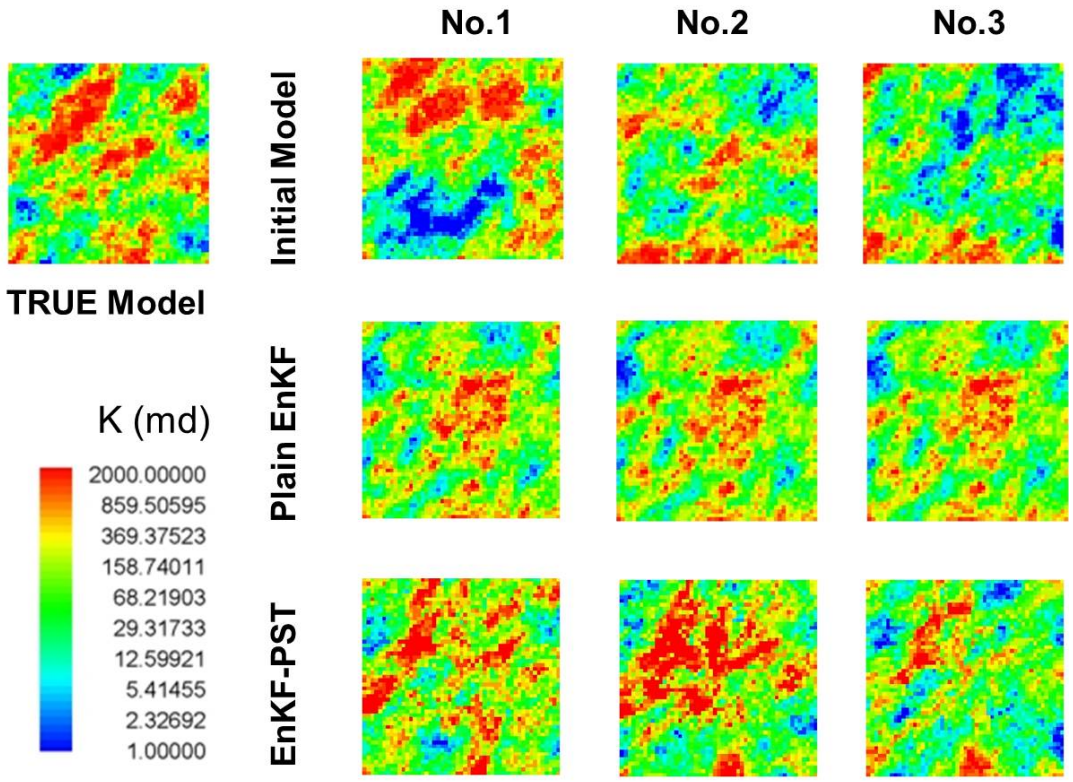

Fig. 2.12—Updated permeability comparisons of Plain EnKF and EnKF-PST. True-model permeability field (top left) and three realizations of initial permeability fields (top row), Plain EnKF updated permeability fields (middle row), and EnKF-PST updated permeability fields (bottom row).)

EnKF-DT1 as the best, followed by EnKF-PST and EnKF-HC1. When we use a shorter correlation distance as in Case 2 (EnKF-DT2), the RMS becomes worse than EnKF-PST. This clearly indicates that the choice of correlation length is critical for distance-based localization performance. All localization schemes seem to prevent ensemble collapse in this example. Eigen spectrum of the updated permeability covariance matrix is plotted for each case in **Fig. 2.17**. The results show that all localization methods maintain the model variability throughout the updating period. In terms of the updated permeability distributions, EnKF-DT1 and EnKF-HC1 fail to reproduce the continuity of the high-permeability streak in Fig. 2.14. Similar results are also obtained for Case 2. In **Fig. 2.18a**, we have compared the localization regions for the three different schemes for computing the covariance of permeability and water cut at 1,200 days. Similarly, in **Fig. 2.18b**, we have shown the localization region for computing the covariance of permeability and GOR at 500 days. Clearly, the distance-based localization uses the same localization region for both the water cut and GOR with the same correlation length. The phase-streamline-based localization accounts for the underlying physics of flow and seems to capture the dynamic change in the localization region with respect to time and space naturally. Finally, because of its statistical nature, the localization region for EnKF-HC1 appears scattered and somewhat noisy, although there is some underlying resemblance with the phase-streamline-based localization region.

Thus, localization is necessary to prevent ensemble collapse in EnKF updating, particularly when the ensemble size is relatively small. The proposed phase-streamline localization can capture the interactions between the flow dynamics and the permeability heterogeneity better than other localization schemes. Also, the method does not require the choice of optimal correlation length as in distance-based localization, because streamlines naturally define the flow-relevant regions.

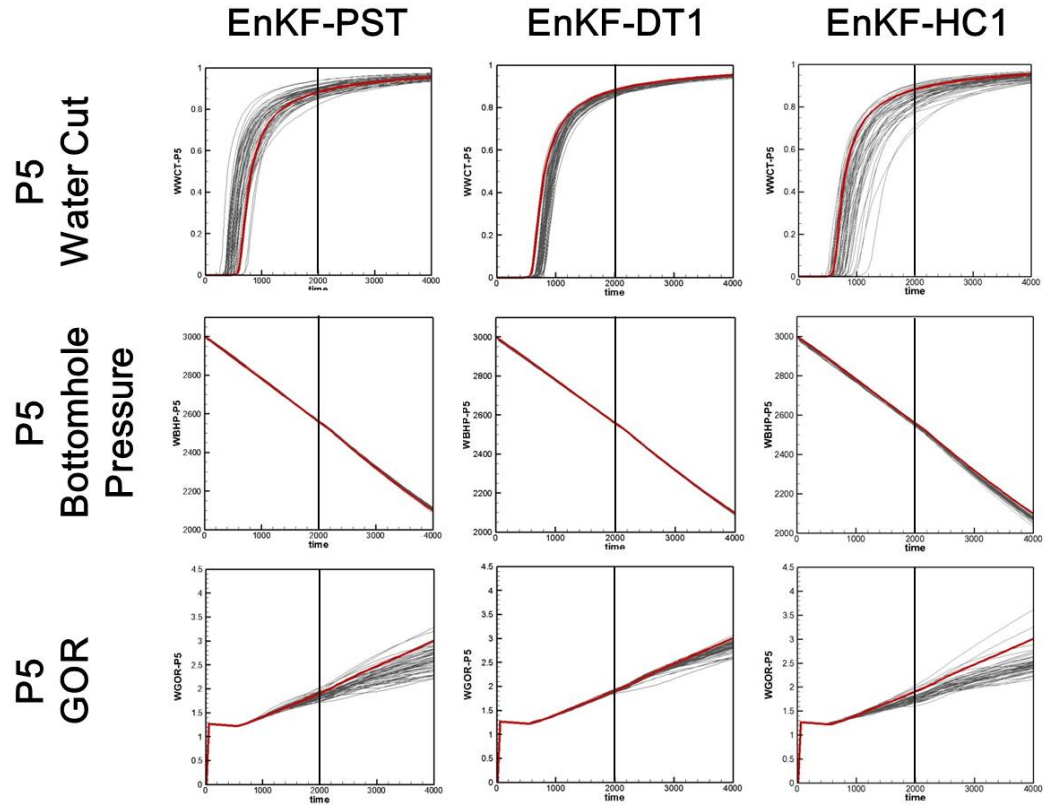

Fig. 2.13—History-matching comparisons of EnKF-PST, EnKF-DT1 (Case 1), and EnKF-HC1 (Case 1). True-model response (red line) and updated-ensemble model responses (gray lines) for water cut of P5, bottomhole pressure of P5, and GOR of P5.

TABLE 2.1—RMS OF HISTORY-MATCHING AND FORECASTING COMPARISONS IN NINE-SPOT MODEL

	Initial	Plain EnKF	EnKF-PST	EnKF-DT1	EnKF-DT2	EnKF-HC1	EnKF-HC2
WCT	2.77E+03	2.61E+01	3.01E+02	8.31E+01	8.39E+02	3.58E+02	2.46E+02
BHP	3.34E+07	5.64E+06	1.12E+07	4.25E+06	1.27E+07	8.34E+06	6.00E+06
GOR	1.29E+03	4.93E+02	8.32E+02	6.16E+02	1.27E+03	1.16E+03	1.05E+03

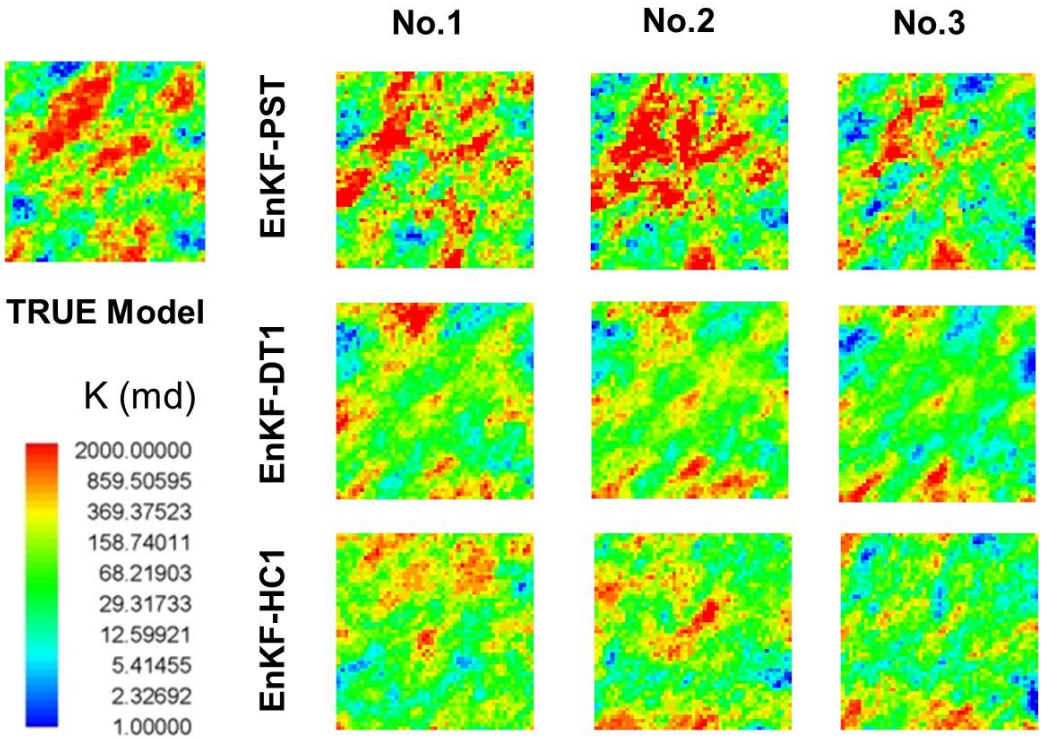

Fig. 2.14—Updated permeability comparisons of EnKF-PST, EnKF-DT1 (Case 1), and EnKF-HC1 (Case 1). True-model permeability field (top left) and three realizations of EnKF-PST updated permeability fields (top row), EnKF-DT1 updated permeability fields (middle row), and EnKF-HC1 updated permeability fields (bottom row).

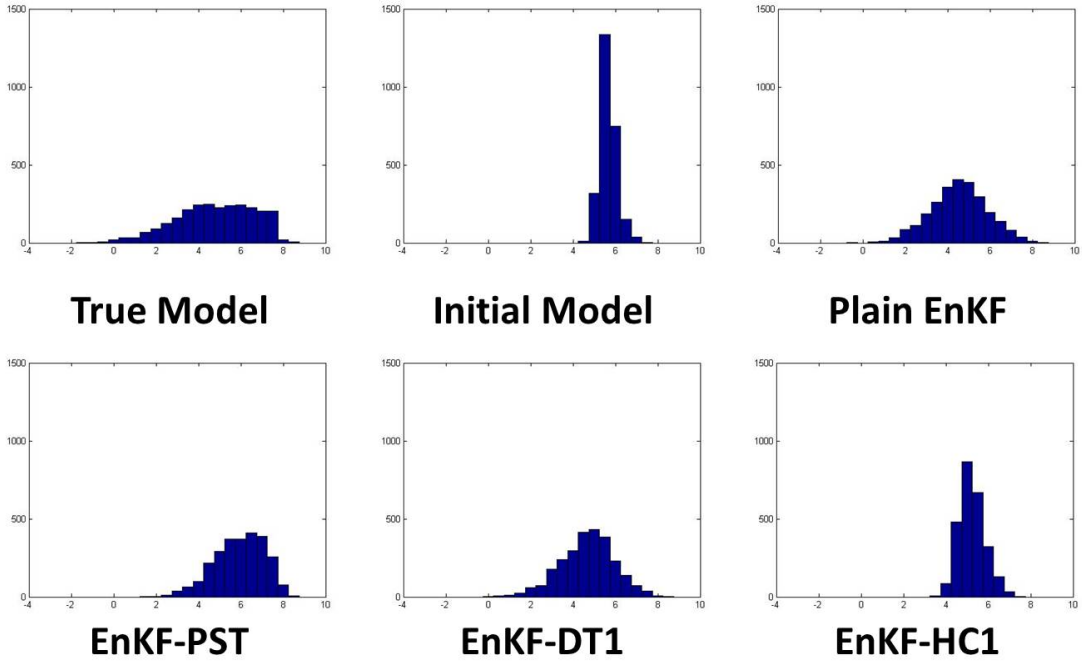

Fig. 2.15—Updated mean permeability histogram comparisons. From top left, true-model permeability field, initial model, and Plain EnKF are shown. From bottom left, EnKF-PST, EnKF-DT1 (Case 1), and EnKF-HC1 (Case 1) are shown.

Fig. 2.16—RMS of history-matching and forecasting comparisons of water cut (left), bottomhole pressure (right), and GOR (bottom). From left, initial models, Plain EnKF, EnKF-PST, EnKF-DT1 (Case 1), EnKF-DT2 (Case 2), EnKF-HC1 (Case 1), and EnKF-HC2 (Case 2).

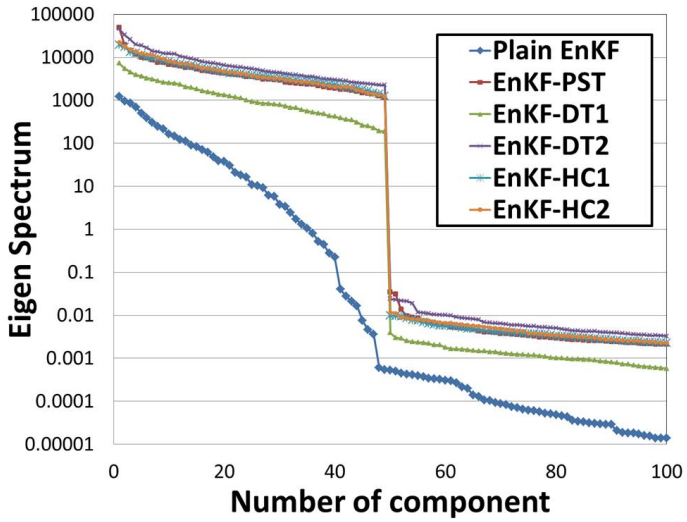

Fig. 2.17—Eigen spectrum of updated parameter-covariance matrix: Plain EnKF, EnKF-PST, EnKF-DT1 (Case 1), EnKF-DT2 (Case 2), EnKF-HC1 (Case 1), and EnKF-HC2 (Case 2), from top legend.

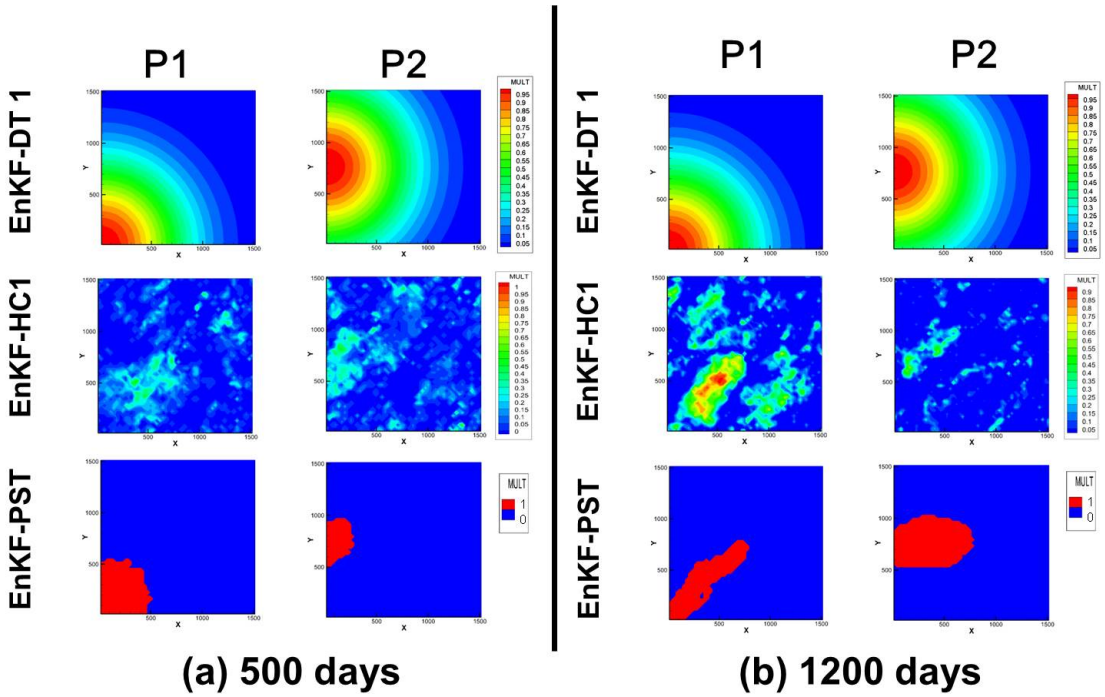

Fig. 2.18—Localization multiplier for EnKF-DT1 (Case 1), EnKF-HC1 (Case 1), and EnKF-PST. (a) Localization multiplier for cross-covariance of permeability and GOR of P1, P2, and P5 at 500 days. (b) Localization multiplier for cross-covariance of permeability and water cut of P1, P2, and P4 at 1,200 days.

2.5.3 PUNQ-Model Application

We now demonstrate the applicability of the proposed phase-streamline localization for the benchmark PUNQ-S3 model, which is designed after a real field (Barker et al. 2001). The model contains $19 \times 28 \times 5$ gridblocks, of which 1,761 are active. The top-structure map of the field shows that the field is bounded to the east and south by a fault, and is supported by a fairly strong aquifer in the north and west (**Fig. 2.19a**). A small gas cap exists in the center of the dome-shaped structure. The field initially contains six production wells drilled around the gas/oil contact. Because of the strong aquifer, no injection wells are present. A geostatistical approach has been used to generate the reservoir-permeability distribution, consistent with the geological model in each of the five layers. The production schedule contains a first year of extended well testing, followed by a 3-year shut-in period before field production starts. The well testing consists of four 3-month production periods. During field production, 2 weeks of each year are used for a shut-in test to collect shut-in pressure data at each well.

A reference "true" model was used to generate the production history. For the production data, Gaussian noise was added to mimic measurement errors. The total simulation period was 16.5 years. The bottomhole-pressure, water-cut, and GOR data were generated for each of the wells. Of the total time, we take a history-matching period of 8 years (0 to 2,936 days) and a forecast period of 8.5 years (2,937 to 6,025 days).

The simulation model is shown in **Fig. 2.19b** and has a corner point grid system. We used 40 ensemble members in the EnKF application. **Fig. 2.20** shows the phase streamlines for this case. From the gas-streamline trajectories, we can identify the communication between the gas cap and the wells with gas breakthrough. The

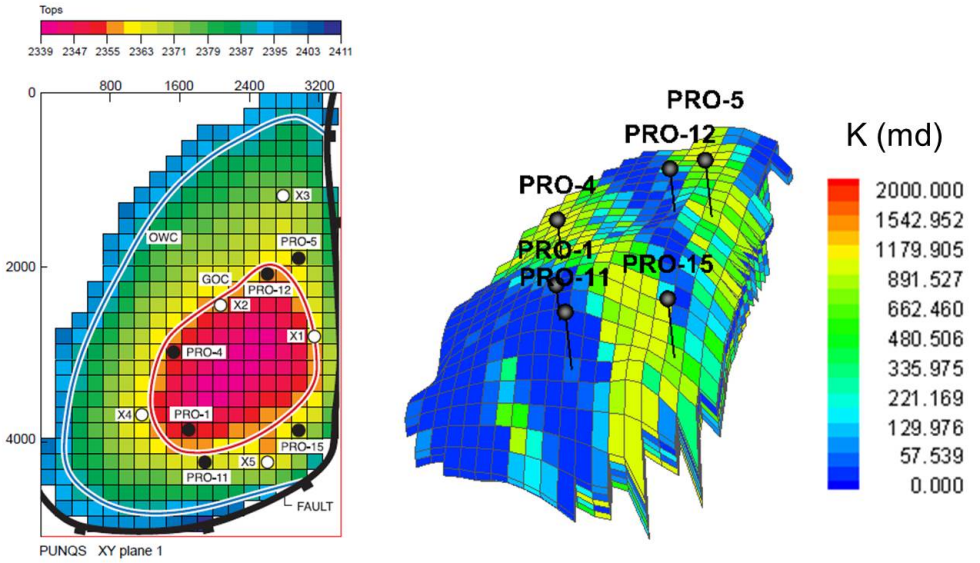

Fig. 2.19—PUNQ-S3 model: (a) top-structure map (from Floris et al.) and (b) simulation model.

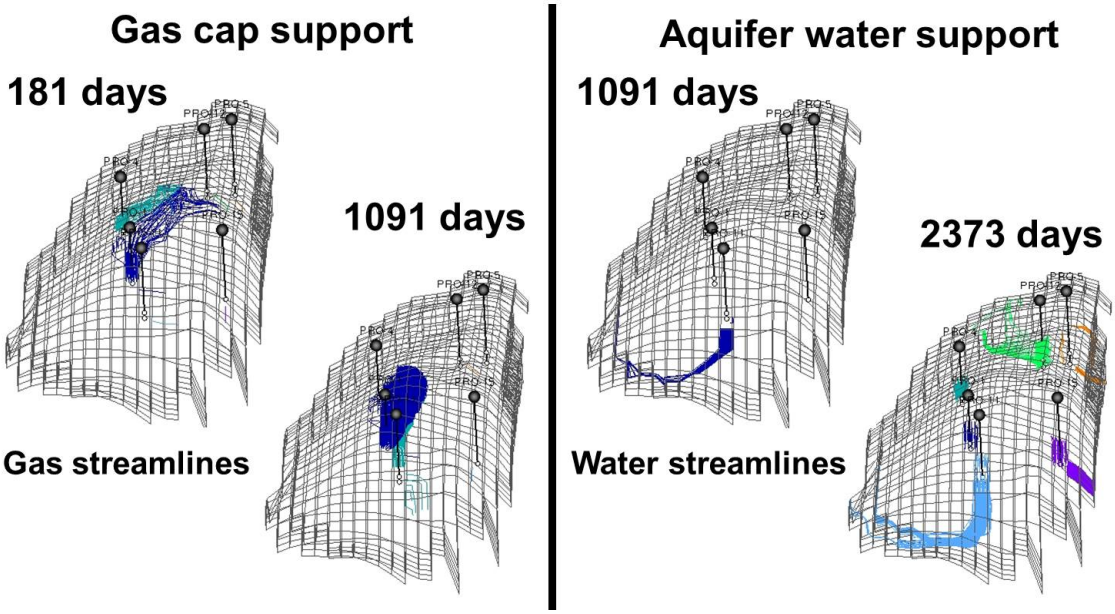

Fig. 2.20—Gas-phase streamlines at 181 days and 1,091 days (left) and water-phase streamlines at 1,091 days and 2,373 days (right). Coloring is with respect to the production well.

aquifer support is depicted by the water streamlines. We conducted Plain EnKF, EnKF-PST, and EnKF-DT for this case. Observation data for the assimilation are water cut, bottomhole pressure, and GOR at the production wells with 20 assimilation times. The model parameter updated is the gridblock permeability. For the distance-based localization, we assigned the same correlation length, a=500 m, for all data types. History-matching results are compared in **Fig. 2.21**, and the RMS errors for all three data types as well as oil-production rate (OPR) are summarized in **Table 2.2** and **Fig. 2.22**. Updated ensemble average permeabilities for EnKF-PST and EnKF-DT are shown in **Fig. 2.23**, and compared with the reference model. Plain EnKF updated permeability fields suffer from over- and undershooting problems and are not shown here. Overall, the results seem to be consistent with the nine-spot synthetic example discussed previously. As for history-matching and forecasting quality, Plain EnKF performs poorly for water-cut matching, shows evidence of ensemble collapse, and results in unsatisfactory forecast. The EnKF-DT has slightly better RMS errors than EnKF-PST, but is almost comparable for this case. However, a comparison of the updated permeability fields in Fig. 2.23 shows that the EnKF-PST outperforms EnKF-DT in terms of capturing the continuity of the permeability barriers and the channels. In particular, the EnKF-PST is able to reproduce the high permeability streaks in Layer 3 and Layer 5, contributing to aquifer support better than EnKF-DT. **Fig. 2.24** compares the corresponding layer-permeability histograms. The results show that the EnKF-PST results in a broader spread in permeability compared with the EnKF-DT. Additionally, in order to analyze the sensitivity of the choice of correlation length for distance-based localization, we rerun EnKF with a shorter correlation length, a=200 m, for all data types. We call this case EnKF-DT1. History-matching results in terms of RMS become worse, as shown in Table 2.2. The corresponding updated permeability fields are shown in

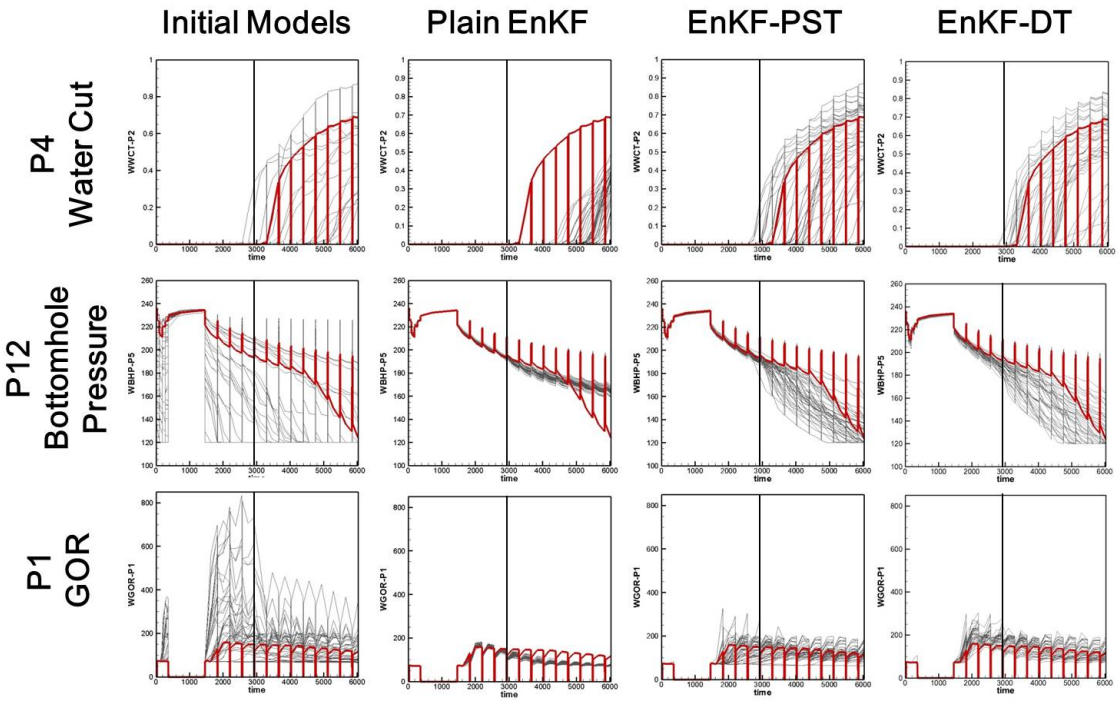

Fig. 2.21—History-matching comparison of Plain EnKF, EnKF-PST, and EnKF-DT. True-model response (red line) and initial- and updated-ensemble model responses (gray lines) for water cut of P4, bottomhole pressure of P12, and GOR of P1.

Fig. 2.23. These results indicate that the selection of correlation length is critical for distance-based localization and for dynamically changing production conditions; this is not a trivial task.

2.6 Conclusions

In this section, we have performed a series of numerical experiments to demonstrate that for three-phase-flow conditions, the region of covariance localization strongly depends on the underlying flow dynamics as well as on the particular data type that is being assimilated, for example, water cut or GOR. Thus, we advocate that the covariance localization should be physically motivated, taking into account underlying physics of flow. For our example cases, the distance-based localization worked well

TABLE 2.2—RMS OF HISTORY-MATCHING AND FORECASTING COMPARISONS IN THE PUNQ MODEL

	Initial	Plain EnKF	EnKF-PST	EnKF-DT	EnKF-DT1
WCT	4.02E+02	3.40E+02	2.90E+02	2.46E+02	3.19E+02
BHP	3.98E+07	2.10E+06	2.10E+06	1.84E+06	2.61E+06
GOR	3.61E+07	3.32E+06	7.47E+06	4.75E+06	1.42E+07
OPR	7.27E+07	1.89E+06	3.16E+06	3.56E+06	6.34E+06

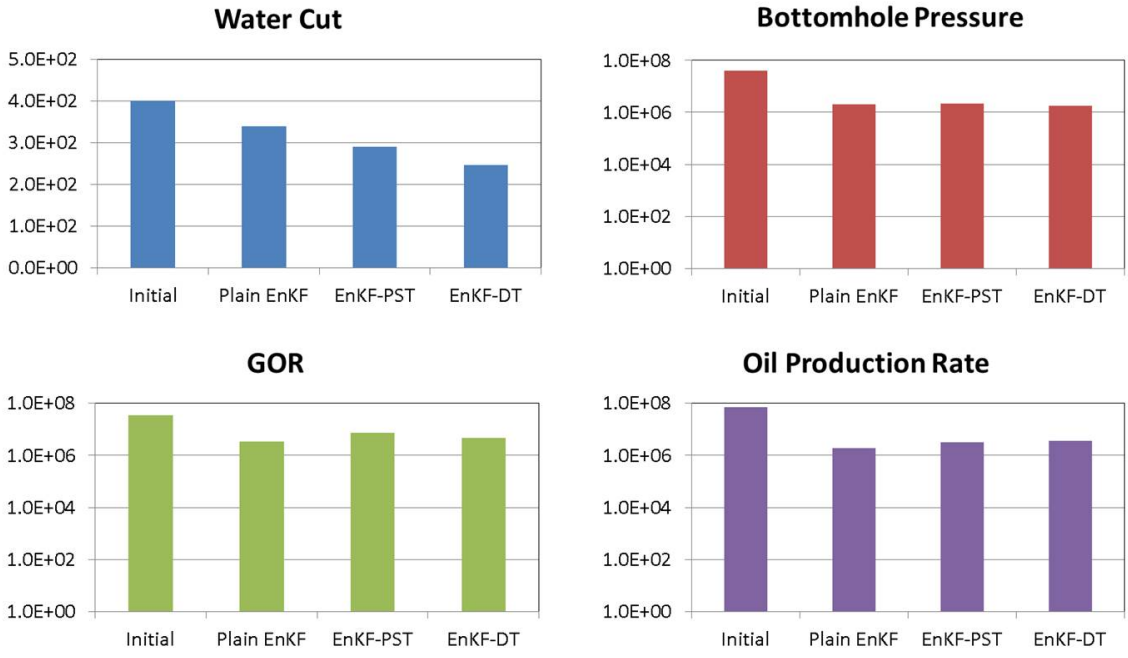

Fig. 2.22—RMS of history-matching and forecasting comparisons of water cut (top left), bottomhole pressure (top right), GOR (bottom left), and OPR (bottom right). (From left: initial models, Plain EnKF, EnKF-PST, and EnKF-DT.)

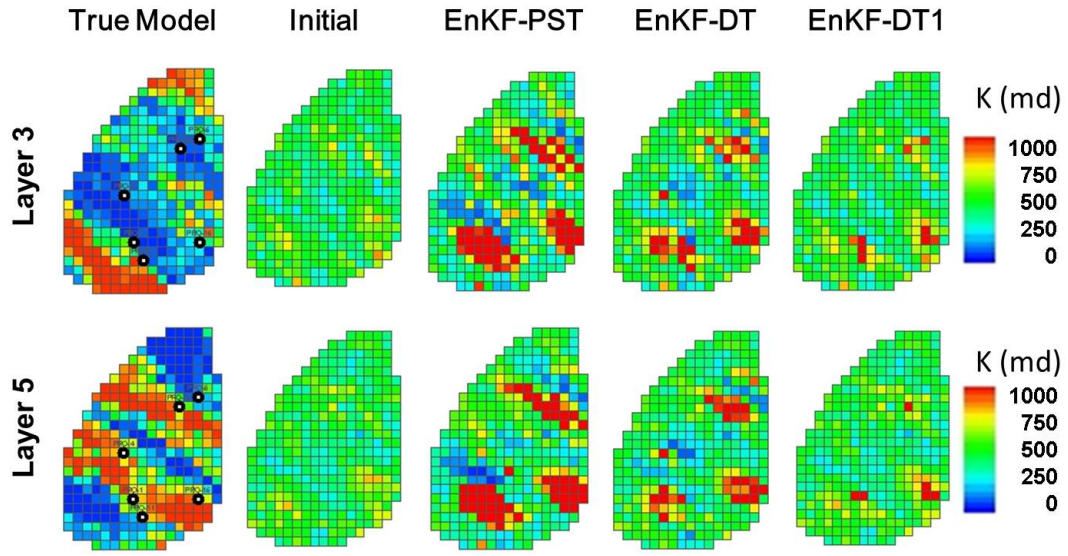

Fig. 2.23—Updated-ensemble mean permeability comparisons of EnKF-PST and EnKF-DT for selected layers (from left: reference model, permeability field, EnKF-PST updated permeability fields, EnKF-DT with correlation length a=500 m updated permeability fields, and EnKF-DT1 with correlation length a=200 m updated permeability fields).

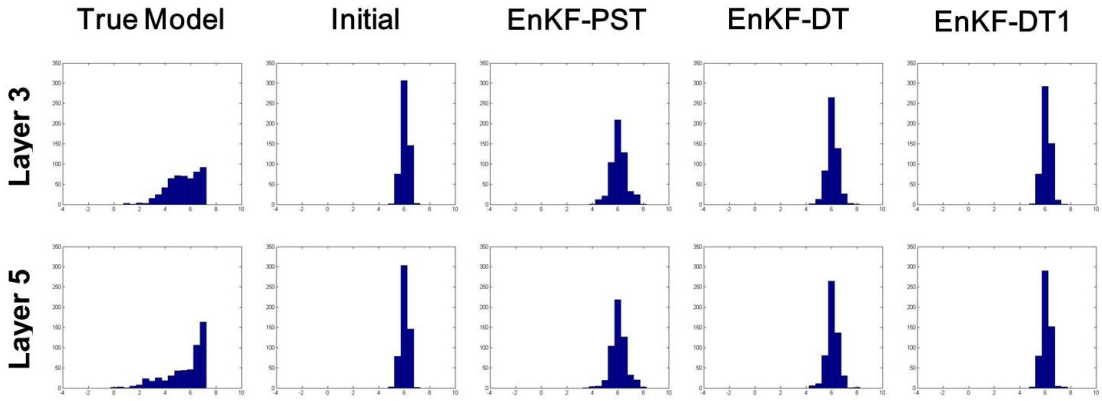

Fig. 2.24—Updated-ensemble mean permeability histogram comparisons for EnKF-PST and EnKF-DT for selected layers (from left: reference-model permeability field, initial, and EnKF-PST updated permeability fields, EnKF-DT with correlation length a=500 m updated permeability fields, and EnKF-DT1 with correlation length a=200 m updated permeability fields).

for integrating bottomhole-pressure data. However, for water-cut and GOR data, the phase-streamline-based localization seems to be a better choice because it does not rely on the selection of correlation length for localization. Also, the region of covariance localization changes with changing flow conditions such as infill drilling, and there is no natural way to account for this in distance-based localization. The hierarchical localization can be computationally demanding and tends to introduce statistical variations in the localization region. The following is a summary of the major features of this section:

- We have proposed a novel methodology for covariance localization based on the reservoir dynamics for three-phase-flow conditions. Specifically, we propose the use of water- and gas- phase streamlines as a means for covariance localization for water-cut- and GOR-data assimilation. The phase streamlines can be computed on the basis of individual-phase velocities, which are readily available after flow simulation.

- Total velocity streamlines have been used in the past for covariance localization in two-phase flow. Unlike the total velocity streamlines, phase streamlines can be discontinuous. We show that the discontinuities in water-phase and gas-phase streamlines naturally define the region of influence for water-cut and GOR data and provide a flow-relevant covariance localization during EnKF updating.

- Our numerical experiments show that the statistical sample cross correlation for water cut and GOR encompasses the underlying physics of the reservoir flow, and their spatial patterns can be explained by the phase-streamline trajectories. Also, phase-streamline-based localization can naturally capture the

dynamically changing localization regions because of changing field conditions such as infill drilling and pattern conversions.

- Our proposed approach improved EnKF performance in terms of (1) adequately matching the data while preserving the model variability without ensemble collapse and (2) quantifying the uncertainty in the forecasting period. In the updated permeability distributions, the phase-streamline-based localization seems to preserve geologic continuities affecting the flow dynamics better than other localization methods.

- The power and utility of our proposed method have been demonstrated through a synthetic model and the benchmark PUNQS3 model.

3. STREAMLINE-BASED TIME LAPSE SEISMIC DATA INTEGRATION INCORPORATING PRESSURE AND SATURATION EFFECTS*

3.1 Summary

We present an efficient history matching approach that simultaneously integrates 4-D seismic surveys with well production data. This approach is particularly well-suited for the calibration of the reservoir properties of high-resolution geologic models because the seismic data is areally dense but sparse in time, while the production data is continuous in time but averaged over interwell spacing. The joint history matching is performed using streamline-based sensitivities derived from either finite-difference or streamline-based flow simulation. Previous approaches to seismic data integration have mostly incorporated saturation effects but the pressure effects have largely been ignored.

We propose, for the first time, streamline-based analytic approaches to compute parameter sensitivities that relate the seismic derived pressure and saturation changes between two surveys to reservoir properties. The inverted seismic data (e.g., changes in pore pressure or fluid saturations), is distributed as a 3-D high-resolution grid cell property or as a vertically integrated two-dimensional map. We derive pressure drop sensitivities along streamlines in addition to our previous work of water saturation sensitivity computation. The novelty of the method lies in the analytic sensitivity computations which make it computationally efficient for high resolution geologic models.

*Part of this section is reprinted with permission from "Streamline-Based Time Lapse Seismic Data Integration Incorporating Pressure and Saturation Effect" by Watanabe, S., Han, J., Datta-Gupta, A., King, M. J., 2013. Paper 166395 prepared for presentation at the SPE Annual Technical Conference and Exhibition held in New Orleans, Louisiana, USA, 30 September-2 October.

We demonstrate the versatility of our approach by implementing it in a finite difference simulator which incorporates detailed physical processes, while the streamline trajectories provide for rapid evaluation of the sensitivities. The efficacy of our proposed approach is demonstrated with both synthetic and field applications. The synthetic example is the SPE benchmark Brugge field case. For both the synthetic and the field cases, the advantages of incorporating the time-lapse variations are clearly demonstrated through improved estimation of the permeability distribution, pressure profile, and fluid saturation evolution and swept volumes.

3.2 Introduction

Three-dimensional (3-D) reservoir simulation models play an essential role in the oil and gas industry. They are routinely utilized to plan the development strategy, calculate hydrocarbon reserves and predict future production estimates. Due to sparse well observation data coverage, reservoir models are often poorly constrained away from well locations. A key challenge for reservoir engineers and geoscientists is therefore the quantitative data integration of 3-D, and where available 4-D, seismic data to obtain a more accurate representation of reservoir properties between wells.

Geostatiscal techniques have been widely adapted in the petroleum industry to construct reservoir models and commercial and research geomodeling software packages are widespread and available (e.g., GSLIB, Deutsch and Journel 1992). For example, geostatistical techniques for constraining 3-D reservoir models with seismic information utilize co-kriging and co-simulation. There are several problems associated with integrating seismic and well data for both 3-D and 4-D reservoir characterization. First, the seismic data must be converted from time to depth, while the velocity model is only calibrated at the wells. Second, seismic data is band-limited, whereas well data has both high and low frequency components. The

seismic response must be calibrated to the well data, but loses the high frequency information. The limited vertical resolution of inverted seismic data has been a major obstacle to the widespread use of seismic information in 3-D property modeling (Doyen et al. 1997). Behrens et al. (1998) introduced a geostatistical method to incorporate seismic attribute maps into a 3-D reservoir model. The method, called sequential Gaussian simulation with block kriging (SGSBK) accounts for the volume support differences between the seismic interval-average rock properties and the well log point-rock properties.

More recently, the concept of time-lapse seismic as the dynamic observation data has emerged. Time-lapse seismic reservoir monitoring is the process of acquiring and analyzing multiple seismic surveys, repeated at the same site over months or years, in order to image fluid flow effects in a producing reservoir. If each survey is "3-D seismic", then the resulting set of time-lapse data is often termed "4-D seismic", where the extra fourth dimension is time.

The first quantitative time-lapse seismic data found in rock physics studies in mid 1980s. The laboratory measurement on heavy oil saturated core samples showed large decreases in seismic rock velocity when the viscous oil was heated (Nur et al. 1984; Wang and Nur 1988; Nur 1989). These rock physics observations have now been validated by many 4-D seismic field data with steam injection projects (Pullin et al. 1987; Eastwood et al. 1994; Jenkins et al. 1997). Early lab measurement of Domenico (1976) showed the presence of free gas in a reservoir without an associated temperature change can also significantly decrease the rock's seismic impedance and this leads to the possibility of monitoring gas-fluid contact movement and injected gases such as CO2 injection projects (Harris et al. 1996).

Monitoring oil-water system is more technically challenging because the seismic impedance contrast between oil and water-saturated rock is often much smaller than

the free-gas or heated oil effects (Wang et al. 1991). Recent developments in seismic processing that improve time-lapse repeatability with noise filtering algorithms facilitated the use of 4-D seismic for monitoring reservoir waterflood performance (Burkhart et al. 2000; O'Donovan et al. 2000; Behrens et al. 2002).

Lumley et al. (1997) and Lumley and Behrens (1998) discussed the practical issues relevant to the successful monitoring of oil-water and other reservoir fluid-flow systems, and the general technical challenges associated with time-lapse seismic reservoir monitoring were thoroughly reviewed (Lumley 2001). With these proposed guidelines, the field applications of time-lapse seismic data has evolved (Fanchi 2001; Clifford et al. 2003) and 4-D seismic is now recognized as a reservoir management tool with a number of successful field applications (Landro et al. 1999; Behrens et al. 2002; Toinet 2004; Foster 2007).

The next logical step of this technology is to use the time-lapse seismic data to infer reservoir permeability and porosity heterogeneity through the reservoir model calibration process, also known as history matching. The traditional history matching process mainly involves production data and the solution is highly non-unique, as production data provides limited information about permeability and porosity variations away from the well locations. The possibility of incorporating 4-D seismic information into history matching as additional dynamic data is therefore attractive as it provides images of fluid movements between wells, albeit at a vertically average scale compared to the layers in the flow simulation model. Time-lapse seismic images can identify the bypassed oil regions to be targeted for infill drilling, and add major reserves to production to extend a field's economic life. Also, 4-D seismic can map the reservoir compartmentalization and identify the fluid flow properties of faults (sealing versus leaking), which can be extremely useful for the optimal design of well trajectories in complex reservoir flow systems.

Previous studies have made several attempts in quantitative 4-D seismic history matching. However, the reconciliation of reservoir model heterogeneity with temporal changes in seismic attributes remains a particularly complex task (Gosselin et al. 2001). Several dynamic data integration algorithms have been proposed in the literature, which can be broadly categorized into three data integration levels: (1) reservoir simulation based integration between the pressure and saturation estimates inverted from seismic observation data and the direct simulated saturation and pressure responses, (2) petro-elastic modeling based integration between the seismic inverted rock elastic properties derived from a geophysical inversion (e.g., acoustic impedance, compressional velocity) and the simulated rock elastic responses from the simulated saturation and pressure responses via petro-elastic models, and (3) seismic forward modeling based integration between the direct seismic traces attributes (e.g., reflection amplitude) and the simulated seismic responses via seismic wave propagation modeling. The diagram of the differing seismic data integration levels is shown in **Fig. 3.1**.

The seismic forward modeling based seismic data integration approach uses direct seismic trace data, and circumvents the uncertainties associated with the seismic inversion process. The general workflow for generating synthetic seismic data from a reservoir simulation model generally involves (1) static reservoir properties on the simulation grid, (2) simulation of dynamic pressure and fluid saturations at each cell, (3) computation of seismic elastic properties (e.g., P and S wave velocities), and finally, (4) simulation of the seismic attribute (e.g., reflection amplitude) by applying a seismic wave propagation model over the reservoir interval and the overburden rock (Mavko et al. 1998; Falcone et al. 2004). This is a computationally demanding process, because it requires the iterative process between the seismic propagation modeling and flow simulation and may be prohibitively expensive for an inversion

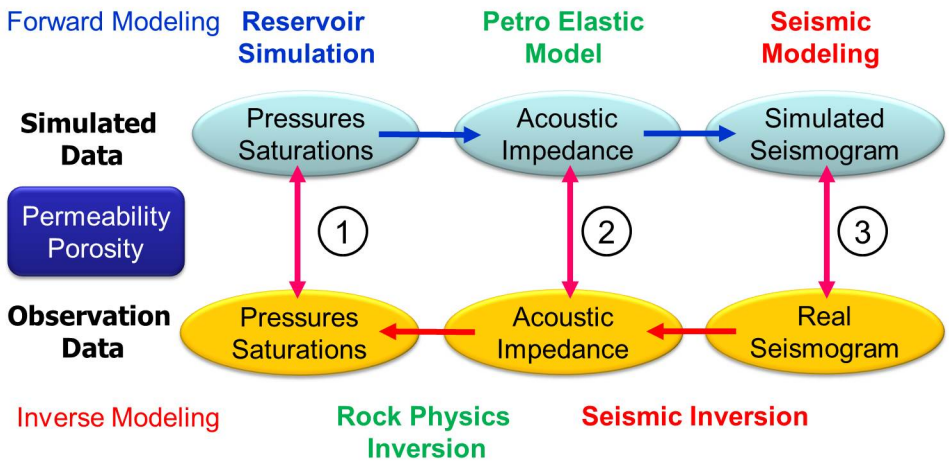

Fig. 3.1—Seismic data integration levels, (1) reservoir simulation level of data integration, (2) petro-elastic modeling level of data integration, and (3) seismic forward modeling level of data integration.

workflow (Gosselin et al. 2003). Despite this, there are a number of publications that use direct seismic attributes for model calibration. Huang et al. (1997) used the reflection amplitude obtained from seismic forward modeling over a volume of synthetic acoustic impedance and matched production and seismic data by updating porosity and permeability maps using a simulated annealing optimization method. Vasco et al. (2004) also used the reflection amplitude to update the grid cell porosity and permeability with a gradient-based algorithm in which the sensitivity of seismic amplitude to reservoir properties is analytically computed using streamline trajectories. Kjelstadli et al. (2005) used the convolution of a wavelet with the seismic reflection coefficients, creating a set of synthetic amplitude traces and generate maps of the summation of negative amplitude (SNA) as the observation data and calibrated zonal heterogeneity multipliers with a genetic algorithm. Dadashpour et al. (2008, 2009, and 2010) used the propagator-matrix method (Stovas and Arntsen 2006) to generate the seismic traces from a stack of plane layer and calibrate reservoir

properties by a Gauss-Newton optimization technique.

The petro-elastic modeling and the reservoir simulation based approaches to seismic data integration are workflows that evaluate the seismic match quality in terms of the inverted seismic responses. The type of time-lapse seismic data considered to be observation data varies among different researchers. The inverted responses can be derived from traditional post-stack data inversion techniques such as the sparse spike inversion (e.g., seismic volumes of acoustic impedance), or from the direct saturation and pressure front detection using an amplitude versus offset (AVO) inversion of pre-stack seismic data (Tura and Lumley 2000; Landro et al. 2001). From a computational standpoint, these methods are more efficient, because they perform the geophysical inversion of the seismic volumes as a separate process from the model calibration workflow. Gosselin et al. (2003) emphasized the need to maintain consistency between the geophysical inversion and the calibration workflow when the data misfit is expressed in terms of rock elastic properties. There are a significant number of publications that apply seismic inverted responses for the reservoir model calibration compared with those that apply the direct seismic attributes. For example, Landa and Horne (1997) used saturation changes obtained directly from inverted time-lapse seismic data. Gosselin et al. (2001) applied synthetic acoustic impedance maps generated with a rock physics model, and calibrate model with a heterogeneity parameterization based on the grad zone analysis. Arenas et al. (2001) used the compressional velocity to calibrate the permeability field at a set of pilot points used as conditioning data by kriging in a gradient-based optimization loop. Dong and Oliver (2005) assumed the availability of differences in acoustic impedance from a geophysical seismic inversion and calibrated the grid cell porosity and permeability using a quasi-Newton method with the objective function gradient calculated by an adjoint method. In stochastic approaches, Skjervheim et al. (2007) used the ensem-

ble Kalman smoother to assimilate the time-lapse seismic data of changes in acoustic impedance and compressional velocity. Fahimuddin et al. (2010) similarly used the seismic derived impedance data with the ensemble Kalman filter with a covariance localization method. Feng and Mannseth (2010) applied a pseudo seismic data in the form of maps of saturation changes and investigated the impact of the seismic data in the presence of noise on permeability estimation. Finally, Rey et al. (2012) applied a streamline based sensitivity calculation to integrate the seismic derived water saturation changes and the acoustic impedance differences and demonstrated field-scale applications.

Our current study examines both reservoir simulation based calibration and petro-elastic modeling based calibration. In the first instance we calibrate against both time lapse changes in pressure and in saturation and this is the scope of this section. In the second instance we calibrate against the time lapse change in acoustic impedance and this is the scope of next section. In both cases, the inversion will provide local updates to the reservoir model using analytic streamline-based sensitivity calculations. This is the major new result of our study. As with most previous studies, we will calibrate against changes in properties over the interval of the time lapse survey, instead of the properties themselves. This minimizes systematic biases introduced by lack of calibration of the initial model. In addition, we will also integrate this approach in a sequential fashion with other forms of data calibration. In both cases we will follow the seismic data integration with a fairly conventional streamline based integration of water-cut field performance. This data is high resolution in time, but only available at the production wells.

The outline of this section is as follows. First, we review the previous work of streamline-based data integration techniques in the literature. Second, we start with the mathematical background to determine the streamline-based analytic sen-

sitivities for fluid saturation and pressure data integration. These sensitivity results are validated by numerical experiments. Finally, we illustrate the history matching applications of time-lapse pressure and saturation changes by using a synthetic model and the SPE benchmark Brugge field model. This combination of examples demonstrates the utility and the effectiveness of our approach.

3.3 Background and Methodology

Our approach relies on the use of streamlines to relate the reservoir properties to the dynamic reservoir responses: production, pressure and time lapse seismic response. Establishing these relations, also called sensitivities, is crucial to the data integration process. We make extensive use of streamlines to describe the flow field and to calculate the fluid tracer time of flight along each streamline. The time of flight acts as a spatial coordinate along the lines. However, our proposed approach does not rely on the use of a streamline simulator, and is well-suited for both conventional finite difference reservoir simulators and streamline simulators. In fact, most of the examples presented in this section utilize a commercial finite difference simulator for flow simulation. For streamline simulators, the streamline trajectories and time of flight are readily available. However, for finite difference simulator, the streamline and time of flight are obtained via a post processing of the finite difference velocity field.

In this section, we first review the previous work of streamline-based data integration techniques in the literature and discuss the mathematical details related to sensitivity computations in streamline-based seismic data integration. The derivations of sensitivity formulation include time of flight sensitivity, saturation front arrival time sensitivity, generalized travel time sensitivity, water saturation sensitivity and pressure drop sensitivity. Also, we discuss the objective function formulation

for data misfit quantification and its minimization.

3.3.1 Streamline-Based Data Integration: Literature Review

Integrating dynamic data into high-resolution reservoir models typically requires the solution of an inverse problem. Such inverse modeling is computationally intensive, often requiring orders of magnitude more computational effort compared to forward modeling or flow simulation. Streamline models have shown significant potential in this respect (Datta-Gupta et al. 1998, Vasco and Datta-Gupta 1999, Vasco et al. 1999). Streamline models are advantageous primarily in two ways. First, streamline simulator offers an efficient approach to fluid flow modeling in the reservoir. Second and more importantly, sensitivities of the production response with respect reservoir parameters such as porosity and permeability can be computed analytically using a single streamline simulation. These sensitivities quantify the change in production response because of a small perturbation in reservoir parameters and constitute an integral part of most inverse modeling algorithm.

Vasco and Datta-Gupta (1999) derived an asymptotic approach to the transport equation and proposed an efficient formalism for the inversion of tracer data. The technique provides tracer concentration sensitivities to porosity, permeability, and pressure gradient variations and has several advantages over existing approaches. First, the technique utilizes an extremely efficient semi-analytic approach to transport modeling that is quite fast even for three-dimensional problem (Datta-Gupta and King 1995). Second, the sensitivities are formulated in terms of one-dimensional integrals of analytic functions along streamlines. The computation of sensitivities for all model parameters requires only a single simulation run to construct the streamlines from the velocity field.

Vasco et al. (1999) extended the analytic approach to compute the sensitivity of

water cut production data with respect to reservoir properties. They also presented a two-step linearized inversion scheme for production data. In particular, the matching of the "first arrival" or breakthrough time followed by amplitude matching speeds up computation, facilitates convergence of the algorithm.

Initial efforts towards dynamic data integration using streamline models were limited to tracer concentration history and multiphase production response such as water-cut data at the wells. This is because initial streamline formulations are particularly well-suited for modeling tracer transport and waterflooding as the velocity field remains relatively static and the streamlines need to be updated only infrequently. Under such conditions streamline models can be order of magnitude faster than conventional finite difference simulators (Datta-Gupta and King 1995; Batycky and Blunt et al. 1997). A key development in streamline modeling has been the introduction of the concept of time-of-flight that has trivialized generalization to three dimensional flows (Datta-Gupta and King 1995). The time of-flight formulation effectively decouples pressure from saturation and concentration calculations during flow simulations.

Datta-Gupta et al. (2001) exploited the analogy between streamlines and seismic ray tracing and utilized concepts from asymptotic ray theory to derive the streamline time-of-flight equations. They have then generalized the streamline approach to compressible flow by introducing a 'diffusive' time of flight based upon an asymptotic solution of the diffusion equation for integrating transient pressure data. They simply compute the 'diffusive' time of flight along streamlines and relate the 'diffusive' time of flight to the time at which the pressure response for an impulse source/sink (drawdown or build up) reaches a maximum at a location. Then they have derived the sensitivity of 'diffusive' time-of-flight with respect to reservoir permeability and porosity analytically.

Wu and Datta-Gupta (2002) and He et al. (2002) utilized the concept of "generalized travel time" from the work by Luo and Schuster (1991) in the context of waveform inversion in seismology and generalized the travel-time inversion method for production data integration and actually reduced the previously proposed two-step inversion approach (travel time and amplitude) into a single-step procedure while retaining most of the desirable features of the travel-time inversion. This "generalized travel-time inversion" reduces the entire production history misfit at a well to a single "optimal travel-time shift". Instead of matching the production data directly, they minimize a travel-time shift derived by maximizing a cross-correlation between the observed and computed production response at each well. This makes the approach extremely computationally efficient and well suited for large-scale field applications.

He et al. (2002) utilized the generalized travel-time inversion to extend streamline-based production data integration methods to changing field conditions involving rate changes and infill drilling. They analytically compute the sensitivity of generalized travel time with respect to reservoir properties such as permeability including pressure updates and gravity effects. The practical feasibility of the method has been demonstrated by a field example from the Goldsmith San Andres Unit (GSAU) in west Texas.

Vasco et al. (2004) applied the streamline trajectory based approach for inverting time lapse seismic amplitude change data. Using Gassman's equation, the seismic amplitude response in the reservoir is a function of the saturation, pressure, and porosity. One application to actual time-lapse data from Bay Marchand field in the Gulf of Mexico indicated that the method is robust in the presence of noise.

Cheng et al. (2005a) showed nonlinearities in the inverse problems related to travel time, generalized travel time, and amplitude matching during production data

integration and their impact on the solution and its convergence. They quantified that commonly used amplitude inversion can be order of magnitude more nonlinear compared to the travel time inversion. They showed that the travel time inversion exhibits superior convergence characteristics and the travel time sensitivities are more uniform between the wells compared to the amplitude sensitivities that tend to be localized near the well. They have demonstrated their results using a field application involving a multiwall, interwell tracer injection study in the McClesky sandstone of the Ranger field in Texas.

He et al. (2006) showed an efficient trajectory-based approach to integrate pressure data into high-resolution reservoir and aquifer models. The method involves alternating travel time and peak amplitude matching of pressure response using inverse modeling using hydraulic tomography or pressure interference tests. They developed analytical approaches to estimate the sensitivities for travel time and peak amplitude of pressure response to subsurface properties. In the field application to a naturally fractured reservoir, an orthogonal fracture pattern was imaged from an interference test which was found to be consistent with independent experimental observations and interpretations.

The generalized travel time history matching technique has been applied in a large number of field cases (Cheng et al. 2004; Hohl et al. 2006), however most of these applications have been limited to two phase water and oil flow under incompressible or slightly compressible conditions. Cheng et al. (2007) extended the streamline approach to history matching three-phase flow using a novel compressible streamline formulation and streamline-derived analytic sensitivities. Streamline models were generalized to include compressible flow by introducing an "effective density" of total fluids along streamlines. They formulated analytic expressions for sensitivity of water-cut and GOR to reservoir properties and combined with the generalized

travel-time inversion.

Oyerinde et al. (2009) proposed a transformation method of the field production data that facilitates the generalized travel-time inversion technique especially for the non-monotonic profile of the GOR data. Also the proposed approach incorporates matching the flowing bottomhole pressure (BHP) using a low frequency asymptotic approach (Vasco and Karasaki 2006) for computing pressure sensitivities. They showed the practical feasibility of the method using a field west Africa reservoir application.

Rey et al. (2011) proposed an efficient technique in computing travel time shift in the presence of production data discontinuity due to frequent field well intervention. The method removes the high frequency components of production data by resampling in terms of equal volumes of oil produced at surface condition and makes the production response more amenable for the travel time inversion. The proposed approach has been applied to an offshore turbidite reservoir with highly detailed production information.

3.3.2 Quantifying Data Misfit: Amplitude vs. Travel-Time Inversion

Production data integration typically involves the minimization of a least squares differences between the observed data and the calculated response from a simulator. Production data misfit is most commonly represented as

$$E_p = \sum_{j=1}^{N_w} \sum_{i=1}^{N_{dj}} w_{ij} \Big(y_j^{cal}(t_i) - y_j^{obs}(t_i) \Big)^2, \tag{3.1}$$

for $i = 1, ..., N_{dj}$ and $j = 1, ..., N_w$. In the given equation, y_j denotes the production data, for example, water cut or tracer response at the producing well j; N_{dj} represents the number of observed data at well j; and N_w is the number of producing wells, respectively. The w_{ij} are weights that can be used to increase or decrease

the influence of the data or to account for measurement errors. We refer the minimization of Eq. (3.1) as "amplitude inversion". Instead, the "travel-time inversion" attempts to match the observed data and model responses at some reference time for example, the breakthrough time or the peak arrival time. **Figs. 3.2a and 3.2b** illustrate the amplitude vs. travel time inversion for tracer response in a well.

There are several advantages of travel-time inversion compared to amplitude inversion. It can be shown that the amplitude inversion is highly nonlinear when compared with travel-time inversion, which has quasilinear properties (Cheng et al. 2005a). As a result, the travel-time inversion is more robust and is less likely to be stuck in local minima. This is well known in the geophysics and seismic tomography literature (Lou and Schuster 1991). However because the travel-time inversion entails matching only a single data point, e.g., the breakthrough time or the peak arrival time, the overall match to the production data may be less than satisfactory.

We can actually combine the travel-time inversion and amplitude inversion into one step via "generalized travel-time inversion" (He et al. 2002). In this approach, we seek an optimal time shift $\Delta\tilde{t}$ of the data at each well so as to minimize the production data mismatch at the well. This is illustrated in **Fig. 3.2c** in which the calculated tracer response is systematically shifted in small time increments toward the observed response and the data misfit is computed for each time increment. The optimal time shift will be given by the $\Delta\tilde{t}$ that minimizes the misfit function:

$$E(\Delta\tilde{t}) = \sum_{i=1}^{N_d} \left(y^{cal}(t_i + \Delta\tilde{t}) - y^{obs}(t_i) \right)^2. \tag{3.2}$$

Or, alternatively, we can maximize the coefficient of determination given by the

following:

$$R^2(\Delta\tilde{t}) = 1 - \frac{\sum_{i=1}^{N_d}\left(y^{cal}(t_i+\Delta\tilde{t}) - y^{obs}(t_i)\right)^2}{\sum_{i=1}^{N_d}\left(y^{obs}(t_i) - \overline{y^{obs}}\right)} \tag{3.3}$$

Thus, the "generalized travel time" at well j is given by the optimal time shift, $\Delta\tilde{t}_j$ that maximizes the correlation coefficient as illustrated in **Fig. 3.2d**. By defining the generalized travel time, we retain the desirable properties of the travel-time inversion and at the same time accomplish amplitude matching of the production data. It is important to note that the computation of the optimal travel-time shift does not require any additional flow simulation. It is carried out by post-processing the data at each well after the production response has been computed.

3.3.3 Time of Flight Sensitivity Calculation

We start with the definition of the streamline time of flight which is the travel time of a neutral tracer along a streamline (Datta-Gupta and King 2007),

$$\tau = \int_{\psi} s(\mathbf{x})dr. \tag{3.4}$$

Here the integral is along the streamline trajectory ψ, $\mathbf{x}$ is the vector containing position: (x, y, z), and r is distance along the streamline, and s is the slowness defined by the reciprocal of the interstitial velocity along the streamline,

$$s(\mathbf{x}) = \frac{1}{|\vec{v}(\mathbf{x})|}. \tag{3.5}$$

Using Darcy's law, the slowness can be written as

$$s(\mathbf{x}) = \frac{\phi(\mathbf{x})}{\lambda_{rt}(\mathbf{x})k(\mathbf{x})|\nabla P(\mathbf{x})|}. \tag{3.6}$$

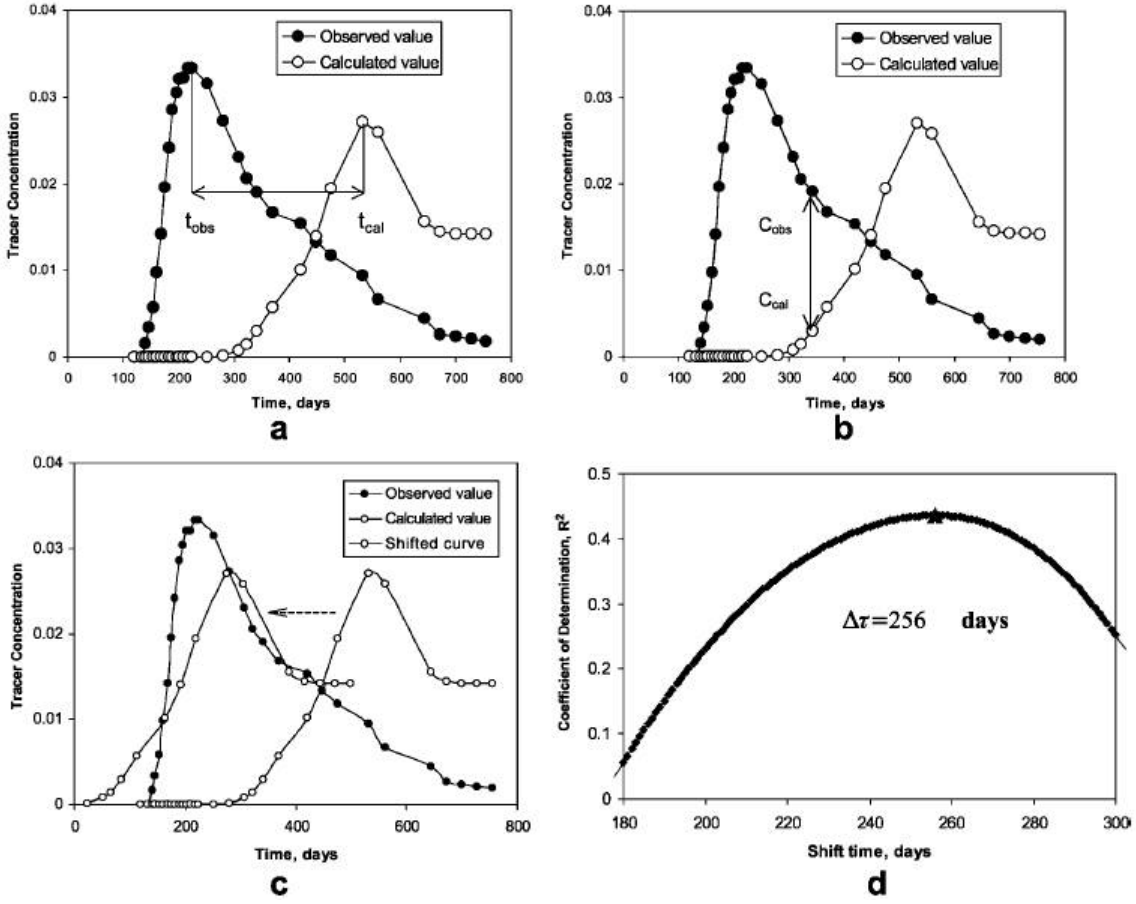

Fig. 3.2—Illustration of (a) travel-time inversion, (b) amplitude inversion, (c) generalized travel-time inversion, and (d) best time shift (from Cheng et al. 2005a).

Here $\lambda_{rt}(\mathbf{x})$ is the total relative mobility, $\lambda_{rt}(\mathbf{x}) = \lambda_{ro}(\mathbf{x}) + \lambda_{rw}(\mathbf{x}) + \lambda_{rg}(\mathbf{x})$, which is the sum of oil, water, and gas phase mobility respectively, and $|\nabla P(\mathbf{x})|$ is the pressure gradient along the streamline. Because slowness is a composite quantity involving reservoir properties, its first order variation, assuming a fixed pressure gradient, will be given by

$$\delta s(\mathbf{x}) = \frac{\partial s(\mathbf{x})}{\partial k(\mathbf{x})}\delta k(\mathbf{x}) + \frac{\partial s(\mathbf{x})}{\partial \phi(\mathbf{x})}\delta\phi(\mathbf{x}), \tag{3.7}$$

From Eq. (3.6) the partial derivatives are

$$\frac{\partial s(\mathbf{x})}{\partial k(\mathbf{x})} \approx \frac{-\phi(\mathbf{x})}{\lambda_{rt}(\mathbf{x})k^2(\mathbf{x})|\nabla P(\mathbf{x})|} = -\frac{s(\mathbf{x})}{k(\mathbf{x})}, \tag{3.8}$$

$$\frac{\partial s(\mathbf{x})}{\partial \phi(\mathbf{x})} \approx \frac{1}{\lambda_{rt}(\mathbf{x})k(\mathbf{x})|\nabla P(\mathbf{x})|} = \frac{s(\mathbf{x})}{\phi(\mathbf{x})}. \tag{3.9}$$

The approximation in Eq. (3.8) and Eq. (3.9) is that the local perturbations in permeability or porosity generate negligible pressure changes. This approximation implies that to leading order streamlines do not shift because of these small perturbations. Now we can relate the change in time of flight $\delta\tau$ to the change in slowness by integrating along each streamline trajectory as

$$\delta\tau = \int_\psi \delta s(\mathbf{x})dr = \int_\psi \left[\frac{\partial s(\mathbf{x})}{\partial k(\mathbf{x})}\delta k(\mathbf{x}) + \frac{\partial s(\mathbf{x})}{\partial \phi(\mathbf{x})}\delta\phi(\mathbf{x})\right]dr. \tag{3.10}$$

Thus, the tracer travel time sensitivity along a single streamline, ψ with respect to permeability and porosity at location $\mathbf{x}$ follows Eq. (3.10) by integrating from the inlet to the outlet of the streamline within the gridblock,

$$\frac{\delta\tau(\psi)}{\delta k(\mathbf{x})} = \int_{\text{inlet}}^{\text{outlet}} \left[-\frac{s(\mathbf{x})}{k(\mathbf{x})}\right]dr = -\frac{\Delta\tau(\mathbf{x})}{k(\mathbf{x})}, \tag{3.11}$$

$$\frac{\delta\tau(\psi)}{\delta\phi(\mathbf{x})} = \int_{\text{inlet}}^{\text{outlet}} \left[\frac{s(\mathbf{x})}{\phi(\mathbf{x})}\right]dr = \frac{\Delta\tau(\mathbf{x})}{\phi(\mathbf{x})}. \tag{3.12}$$

Here $\Delta\tau(\mathbf{x})$ is the time-of-flight across the gridblock at location $\mathbf{x}$.

3.3.4 Saturation Front Arrival Time Sensitivity

In the previous section we developed expressions for sensitivity of the streamline time of flight to reservoir porosity and permeability. We now relate the time of flight sensitivity to the travel time sensitivity of the water saturation. For two phase flow, this sensitivity is used after water breakthrough at a producing well to calibrate the reservoir properties to water cut response, and can be generalized to three phase flow. First, we consider two phase incompressible flow of oil and water described by the Buckley-Leverett equation written using the streamline time of flight as the spatial coordinate (Datta-Gupta and King 2007),

$$\frac{\partial S_w}{\partial t} + \frac{\partial F_w}{\partial \tau} = 0. \tag{3.13}$$

The velocity of a given saturation S_w along a streamline ψ is given by the slope of the fractional flow curve,

$$\left(\frac{\partial \tau}{\partial t}\right)_{S_w} = \frac{dF_w}{dS_w}. \tag{3.14}$$

This equation relates the travel time of a saturation, $t(S_w, \tau; \psi)$ to the time of flight, τ as $\dfrac{\tau}{t} = \dfrac{dF_w}{dS_w}$. We can now compute the sensitivity of the saturation arrival time using that of the streamline time of flight as follows:

$$\frac{\delta t(S_w, \tau; \psi)}{\delta k(\mathbf{x})} = \frac{\delta \tau(\psi)}{\delta k(\mathbf{x})} \Big/ \frac{dF_w}{dS_w}, \tag{3.15}$$

$$\frac{\delta t(S_w, \tau; \psi)}{\delta \phi(\mathbf{x})} = \frac{\delta \tau(\psi)}{\delta \phi(\mathbf{x})} \Big/ \frac{dF_w}{dS_w}. \tag{3.16}$$

After water breakthrough on a streamline, these arrival times are evaluated at the total time of flight, $\tau(\psi)$, for the streamline.

3.3.5 Generalized Travel Time Sensitivity

Now, consider a small perturbation in reservoir properties, $\delta\mathbf{m}$ so that it results in a time shift δt for the entire computed water cut responses at the producing well, that is, every data point of well j has a common time shift. We then have the following relationship for the observed times $(t_1, ..., t_{N_d})$:

$$\delta t = \delta t_i = \left[\frac{\partial t_i}{\partial \mathbf{m}}\right]^{\top} \delta\mathbf{m}, \tag{3.17}$$

for $i = 1, ..., N_d$ where $\mathbf{m}$ represents the reservoir parameter vector. Summing Eq. (3.17) over all the data points, we can arrive at the following simple expression for the sensitivity of the travel-time shift with reservoir parameter, m, which represents a component of the vector $\mathbf{m}$ (He et al. 2002),

$$\frac{\delta t}{\delta m} = \frac{1}{N_d}\sum_{i=1}^{N_d}\left(\frac{\delta t_i}{\delta m}\right). \tag{3.18}$$

Also, based on the definition of the generalized travel time, we have the following:

$$\frac{\delta \Delta\tilde{t}}{\delta m} = -\frac{\delta t}{\delta m}. \tag{3.19}$$

The negative sign in Eq. (3.19) reflects the sign convention adopted for defining the generalized travel-time shift, which is considered positive if the computed response is to the left of the observed data as shown in **Fig. 3.2c**. We now obtain a rather simple expression for the sensitivity of the generalized travel time with respect to reservoir parameters as follows:

$$\frac{\delta \Delta\tilde{t}}{\delta m} = -\frac{1}{N_d}\sum_{i=1}^{N_d}\left(\frac{\delta t_i}{\delta m}\right). \tag{3.20}$$

In the equation given here, the travel time sensitivity with respect to reservoir parameters, $\delta t_i/\delta m$ are given by Eq. (3.15) for permeability and Eq. (3.16) for porosity respectively.

3.3.6 Water Saturation Sensitivity Calculation

We now derive expressions for the sensitivity of water saturation with respect to variations in permeability. For two phase flow, water saturation is a function of the streamline time of flight, τ and time, t. First consider self-similar solutions to Eq. (3.13), as have just been derived. Along a streamline the saturation is a function of the dimensionless ratio τ/t. This allows us to relate the partial derivative of saturation with respect to time to the partial derivative with respect to τ as follows:

$$\frac{\partial S_w}{\partial t} = -\frac{\tau}{t^2}\frac{dS_w(\tau/t)}{d(\tau/t)}, \tag{3.21}$$

$$\frac{\partial S_w}{\partial \tau} = \frac{1}{t}\frac{dS_w(\tau/t)}{d(\tau/t)}. \tag{3.22}$$

Hence:

$$\frac{\partial S_w}{\partial \tau} = -\frac{t}{\tau}\frac{\partial S_w}{\partial t}. \tag{3.23}$$

From this we have the water saturation sensitivity by a chain rule:

$$\frac{\delta S_w(\tau,t)}{\delta k(\mathbf{x})} = \frac{\partial S_w}{\partial \tau}\frac{\delta \tau}{\delta k(\mathbf{x})} = -\frac{t}{\tau}\frac{\partial S_w}{\partial t}\frac{\delta \tau}{\delta k(\mathbf{x})}. \tag{3.24}$$

The partial derivative of water saturation with respect to time in Eq (3.24) can be calculated numerically by a backward time difference as

$$\frac{\partial S_w(\tau,t)}{\partial t} \approx \frac{S_w(\tau,t) - S_w(\tau,t-\Delta t)}{\Delta t}. \tag{3.25}$$

Here Δt is the timestep size. This requires saving the saturation information for the timestep immediately prior to the time lapse survey time. Therefore, the saturation sensitivity at location $\boldsymbol{\tau}$ at a given time t can be calculated by:

$$\frac{\delta S_w(\boldsymbol{\tau}, t)}{\delta k(\mathbf{x})} = -\frac{t}{\boldsymbol{\tau}} \frac{S_w(\boldsymbol{\tau}, t) - S_w(\boldsymbol{\tau}, t - \Delta t)}{\Delta t} \frac{\delta \boldsymbol{\tau}}{\delta k(\mathbf{x})}, \tag{3.26}$$

where the last functional variation of travel time with respect to permeability can be obtained from Eq. (3.11)

The derivation in Eq. (3.26) assumes that the streamline trajectories do not change with time. This is an incorrect assumption considering the large time intervals typically used in time lapse seismic surveys. Also, most often we are calibrating against the changes in saturation, rather than the saturation itself. The generalization of the sensitivity calculation to account for these effects is discussed in the **Appendix A**.

3.3.7 Pressure Data Integration

Pressure data integration is performed by converting the spatial distribution of pressure to a spatial distribution of the viscous pressure drop along a streamline from each location, to the producing well where that streamline terminates. Specifically, for a particular location i, and pressure P_i then the pressure drop, $\Delta P|_w^i$ along the streamline passing through the location i and leading to well w with bottomhole pressure P_w (**Fig. 3.3**) is:

$$P_i = P_w + \Delta P|_w^i. \tag{3.27}$$

This utilizes the (known) bottomhole flowing pressure at the time at which the spatial distribution of pressure data was obtained. If distributed time lapse pressure data and well bottomhole pressure are available, we can compute the pressure drop from

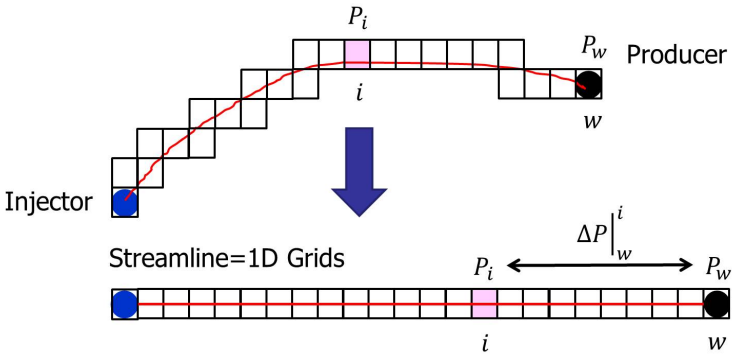

Fig. 3.3—A streamline between well pairs connecting gridblocks.

Eq. (3.27) and use it as our observation data,

$$\Delta P|^i_{w,obs} = P_{i,obs} - P_{w,obs}. \tag{3.28}$$

Now, the data misfit between the simulation response and observation can be written as

$$\begin{aligned} \delta d_i &= \Delta P|^i_{w,obs} - \Delta P|^i_{w,cal} \\ &= (P_{i,obs} - P_{w,obs}) - (P_{i,cal} - P_{w,cal}) \\ &= (P_{i,obs} - P_{i,cal}) - (P_{w,obs} - P_{w,cal}). \end{aligned} \tag{3.29}$$

The first term is the pressure difference at location i, and the second term is the bottomhole pressure difference at well w.

3.3.8 Pressure Drop Sensitivity Calculation

The pressure drop along a streamline can be expressed as

$$\Delta P = \int_{\psi} \hat{\mathbf{v}} \cdot \nabla P(\mathbf{x}) dr. \tag{3.30}$$

This is the integral of the projection of pressure gradient, $\nabla P(\mathbf{x})$ on the unit direction vector from downstream, $\hat{\mathbf{v}}$ along the streamline with r is distance along the streamline. This can be computed by simply summing up the pressure drop across the gridblocks that intersect the streamline as shown in **Fig. 3.3**. Further, we can express the local pressure drop along a streamline using Darcy's law as

$$\Delta P(\mathbf{x}) = \hat{\mathbf{v}} \cdot \nabla P(\mathbf{x}) dr = \frac{q(\mathbf{x})}{A(\mathbf{x})\lambda_{rt}(\mathbf{x})k(\mathbf{x})}, \tag{3.31}$$

where $A(\mathbf{x})$ is the cross sectional area, $q(\mathbf{x})$ is the flow rate along a streamline, $\lambda_{rt}(\mathbf{x})$ is the total relative mobility. The pressure drop is a composite quantity involving reservoir properties. We assume that the streamline trajectories, flow rate along streamline and the total mobility do not change because of small perturbations in permeability. We can now relate the change in local pressure drop to a small change in permeability as

$$\delta\Delta P(\mathbf{x}) = \hat{\mathbf{v}} \cdot \delta\nabla P(\mathbf{x}) dr = \frac{\partial \Delta P(\mathbf{x})}{\partial k(\mathbf{x})} \delta k(\mathbf{x}), \tag{3.32}$$

where the partial derivative is

$$\frac{\partial \Delta P(\mathbf{x})}{\partial k(\mathbf{x})} \approx \frac{-q(\mathbf{x})}{A(\mathbf{x})\lambda_{rt}(\mathbf{x})k^2(\mathbf{x})} = -\frac{\Delta P(\mathbf{x})}{k(\mathbf{x})}. \tag{3.33}$$

The pressure drop to a location i, $\Delta P|_w^i$ will be given by integration along the streamline trajectory passing through i to well w,

$$\delta\Delta P|_w^i = \int_\psi \hat{\mathbf{v}} \cdot \delta\nabla P(\mathbf{x}) dr = \int_\psi \frac{\partial \Delta P(\mathbf{x})}{\partial k(\mathbf{x})} \delta k(\mathbf{x}) \tag{3.34}$$

and the pressure drop sensitivity for a particular gridblock at location $\mathbf{x}$ follows from Eq. (3.34),

$$\frac{\delta \Delta P|_w^i(\psi)}{\delta k(\mathbf{x})} = \int_{\text{producer}}^{\text{location}} \left[\frac{\hat{\mathbf{v}} \cdot \delta \nabla P(\mathbf{x})}{\delta k(\mathbf{x})} \right] dr = -\frac{\Delta P(\mathbf{x})}{k(\mathbf{x})}. \tag{3.35}$$

3.3.9 Objective Function Minimization Formulation

After we compute the sensitivities of the seismic derived data and/or the production data with respect to the gridblock permeability, we perform the data integration by minimizing a penalized misfit function consisting of the following three terms (He et al. 2002):

$$o(\delta \mathbf{m}) = \|\delta \mathbf{d} - \mathbf{S}\delta \mathbf{m}\| + \beta_1 \|\delta \mathbf{m}\| + \beta_2 \|\mathbf{L}\mathbf{m}\|. \tag{3.36}$$

In the above expression, $\delta \mathbf{d}$ is the data misfit between the observation and simulated response, and $\mathbf{S}$ is the sensitivity matrix containing the sensitivities of model responses with respect to reservoir parameters. Also $\delta \mathbf{m}$ corresponds to the reservoir parameter change vector and $\mathbf{L}$ is a second spatial difference operator matrix. The first term ensures the difference between the observed and calculated model response is minimized. The second term, called a "norm constraint", penalizes deviations from the prior model. This prevents large changes and maintains geologic realism by preserving major features of the prior model during the model calibration process. Finally, the third term, a "roughness constraint", constrains the model changes to be spatially smooth. The weights β_1 and β_2 determine the relative strengths of the norm and smoothness constraints; guidelines exist in the literature for their selection. An iterative sparse matrix solver, LSQR (Paige and Saunders 1982), is used for solving the augmented linear system efficiently.

In this section, we carry out the data integration in a sequential manner starting with pressure data first followed by the saturation changes and then the well produc-

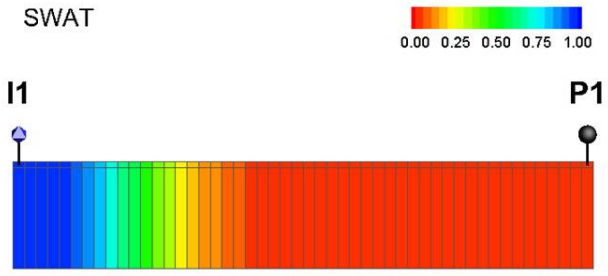

Fig. 3.4—A 1-D simulation model.

tion information. The sequential framework is analogous to the structured approach used in the industry (Williams et al. 1998; Cheng et al. 2008) and accounts for the different length scales associated with different data types. The sequential framework also facilitates convergence of the inversion algorithm. The norm constraint in Eq. (3.36) maintains consistency between different steps in the sequential process by limiting the changes and thus, preserves the calibration results from the previous step.

3.4 Sensitivity Calculation Validations

In this section, numerical experiments are conducted to verify the proposed water saturation and pressure drop sensitivity calculations.

3.4.1 Water Saturation Sensitivity Validation

We set up a simple model which is a 1-D homogeneous model with one injector and one producer at the two ends as shown in **Fig. 3.4**. It is similar to a core flood experiment. The system is two phase oil and water. Rock and fluid properties are summarized in **Table 3.1** and relative permeability curves are shown in **Fig. 3.5**. Wells are controlled by bottomhole pressure constraints. We conduct the simulation for 50 days with 10 timesteps of 5 days. Simulation specification is summarized in **Table 3.2**.

TABLE 3.1—ROCK AND FLUID PROPERTIES.	
Porosity	0.15
Permeability, mD	200
Rock compressibility, 1/psi	8.0×10^{-6}
Oil density, lb/cf	52.1
Water density, lb/cf	63.3
Oil viscosity, lb/cf	0.29
Water viscosity, cp	0.31
Oil formation volume factor	1.305
Water formation volume factor	1.04

$*$PVT values are at the reference pressure of 5,000 psi.

TABLE 3.2—SIMULATION SPECIFICATIONS OF SATURATION SENSITIVITY VALIDATION CASE.	
Grid number	50 x 1 x 1
Grid size, ft	20 x 20 x 20
Initial pressure, psi	5000
Injector location	(1,1,1)
Injector bottom hole pressure, psi	5200
Producer location	(50,1,1)
Producer bottom hole pressure, psi	5000
Total simulation time, days	50
Timestep size, days	5

We compare the proposed sensitivity calculation with a numerical perturbation method. The numerical perturbation method calculates the sensitivity as

$$d = g(m), \tag{3.37}$$

$$\frac{\partial d}{\partial m} \approx \frac{g(m + \delta m) - g(m)}{\delta m}. \tag{3.38}$$

Here d is the observed quantity, $g(\circ)$ is the non-linear function of reservoir simu-

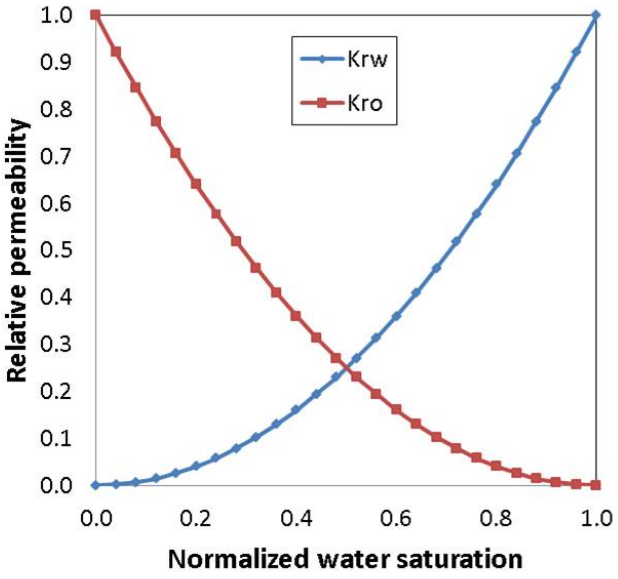

Fig. 3.5—Relative permeability curves.

lation and m is the perturbed reservoir property. Therefore the total computation requires N_g+1 simulations, where N_g is the number of gridblocks, while the proposed analytic sensitivity calculation requires only a single simulation. For the following experiment, the perturbation value is 10 % of the original parameter value for numerical sensitivity calculations.

Water saturation sensitivities with respect to reservoir permeability are shown in **Fig. 3.6**. The proposed streamline based sensitivity calculation shows very good agreement with the numerical perturbation values. The peak value of the sensitivity profile corresponds to the water saturation front location where a sharp saturation change occurs. Behind the water saturation front location, the sensitivity profile decays because the saturation changes diminish.

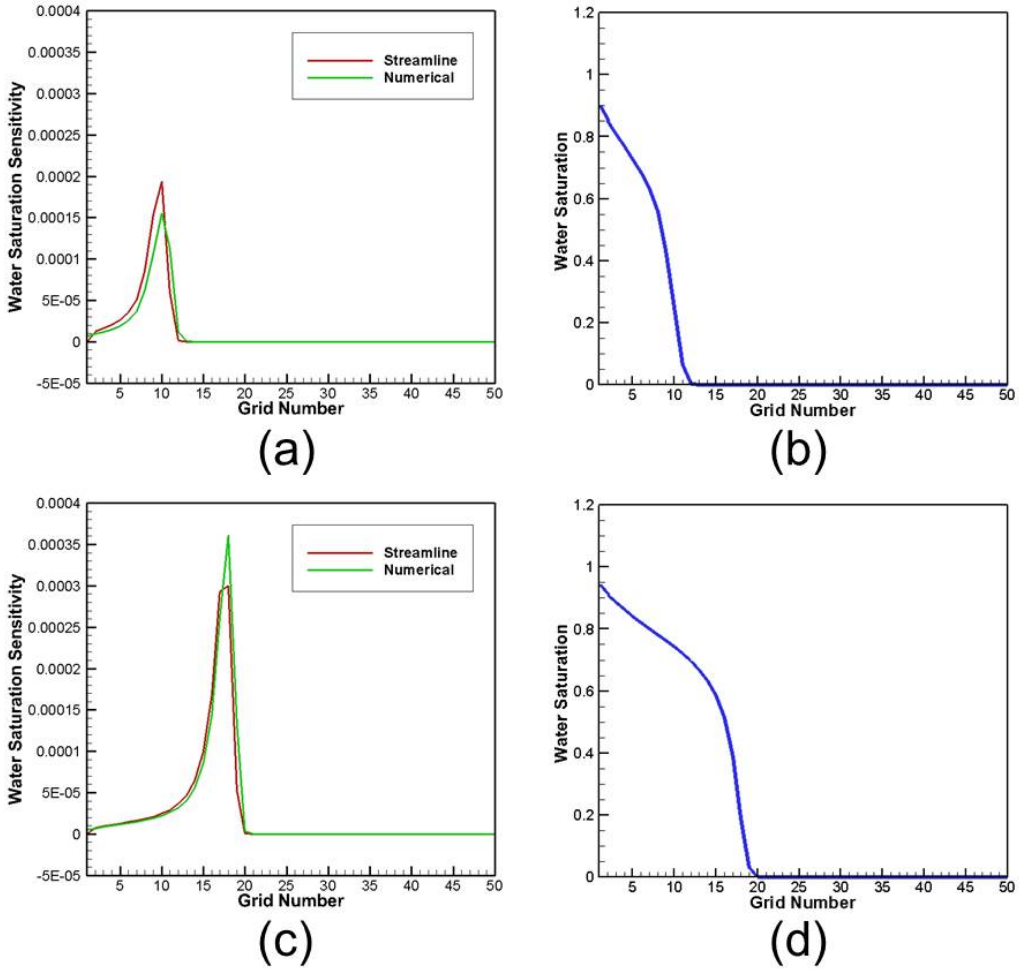

Fig. 3.6—Water saturation sensitivity with respect to reservoir permeability comparisons. (a) Sensitivity values with respect to the permeability of gridblock no. 15 at a time of 25 days. Red line is the analytic streamline based calculation, green line is the numerical perturbation. (b) Water saturation profile at a time of 25 days. (c) Sensitivity values with respect to permeability of gridblock no. 15 at a time of 50 days. (d) Water saturation profile at a time of 50 days.

TABLE 3.3—SIMULATION SPECIFICATIONS OF PRESSURE SENSITIVITY VALIDATION CASE.	
Grid number	50 x 1 x 1
Grid size, ft	20 x 20 x 20
Initial pressure, psi	5000
Injector location	(1,1,1)
Injection rate, rb/day	50
Producer location	(50,1,1)
Production rate, rb/day	50
Total simulation time, days	50
Timestep size, days	5

3.4.2 Pressure Drop Sensitivity Validation

The pressure drop sensitivity calculation is verified using the same model as in the previous section. However, the boundary condition is now changed to rate constraints as shown in **Table 3.3**. Pressure drop sensitivities with respect to reservoir permeability are shown in **Fig. 3.7**. The proposed streamline based sensitivity calculation shows very good agreement with the numerical perturbation values. The sensitivity profile shows that the sign of the sensitivity contains both positive and negative values symmetrically with respect to the perturbation point (Gridblock No. 15). Also the comparisons of sensitivity profile at different time shows that the shape of the sensitivity profile does not change significantly with time. However, the magnitude of the sensitivity value does change because the local pressure gradient changes when water displaces oil providing a change in the total mobility.

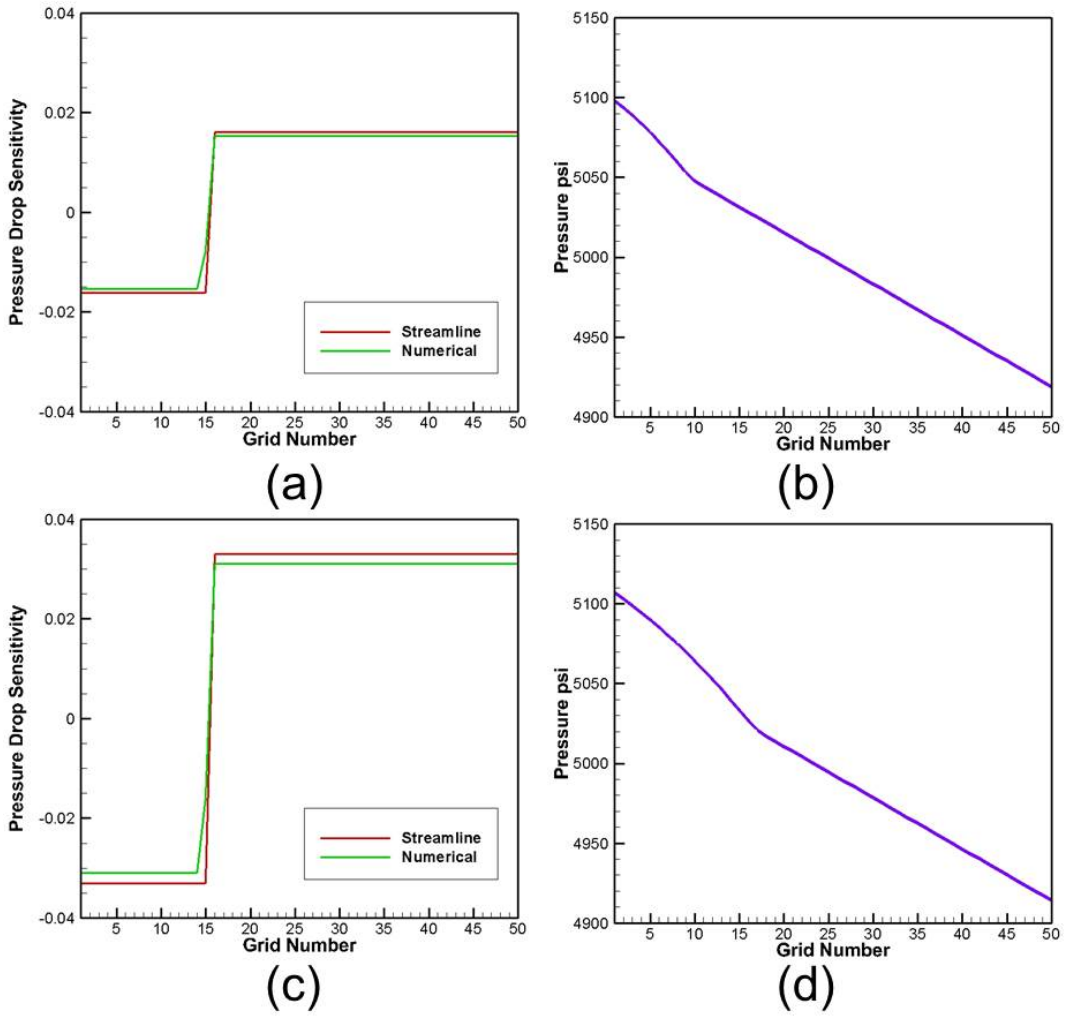

Fig. 3.7—Pressure drop sensitivity with respect to reservoir permeability comparisons. (a) Sensitivity values with respect to the permeability of gridblock no. 15 at a time of 25 days. Red line is the analytic streamline based calculation, green line is the numerical perturbation. (b) Pressure profile at a time of 25 days. (c) Sensitivity values with respect to permeability of gridblock no. 15 at a time of 50 days. (d) Water saturation profile at a time of 50 days.

TABLE 3.4—ROCK AND FLUID PROPERTIES.	
Porosity	0.25
Rock compressibility, 1/psi	8.1×10^{-6}
Oil density, lb/cf	52.1
Water density, lb/cf	63.3
Oil viscosity, cp	0.29
Water viscosity, cp	0.31
Oil formation volume factor	1.305
Water formation volume factor	1.04

∗**PVT values are at the reference pressure of 5,863.8 psi.**

3.5 History Matching Applications

3.5.1 Five-Spot Synthetic Case

Our first example of seismic history matching is a synthetic 2-D model to illustrate the proposed inversion approach. The model contains $50 \times 50 \times 1$ cells with a five-spot well configuration: one injector in the center and 4 producers at the corners. Wells are constrained by the historical (constant) reservoir flow rates. The rock and fluid properties and the simulation specifications are summarized in **Table 3.4 and Table 3.5** respectively. The relative permeability curves are the same as **Fig. 3.5**. The reference permeability model is generated by sequential Gaussian simulation with well permeability values as conditioning data as shown in **Fig. 3.8a**. The prior permeability model is shown in **Fig. 3.8b**. It is also generated by sequential Gaussian simulation but with different geostatistical parameters from the reference model. The observation data is generated from the reference model using a commercial reservoir simulator. These include well production data and 2-D maps of pressure and saturation changes between 260 days and 1,560 days from the start of production (**Fig. 3.9a and Fig. 3.9b**).

TABLE 3.5—SIMULATION SPECIFICATIONS OF FIVE-SPOT SYNTHETIC CASE.	
Grid number	50 x 50 x 1
Grid size, ft	32.8 x 32.8 x 32.8
Initial pressure, psi	5863.8
Injector location	(25,25,1)
Injector rate, rb/day	2515
Producer location	(1,1,1),(1,50,1),(50,1,1),(50,50,1)
Producer rate, rb/day	628.98
Total simulation time, days	2080
Timestep size, days	260

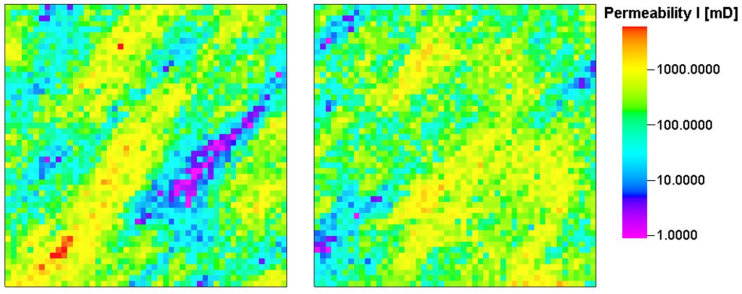

Fig. 3.8—Five-spot permeability models. (a) Reference model, and (b) Initial model.

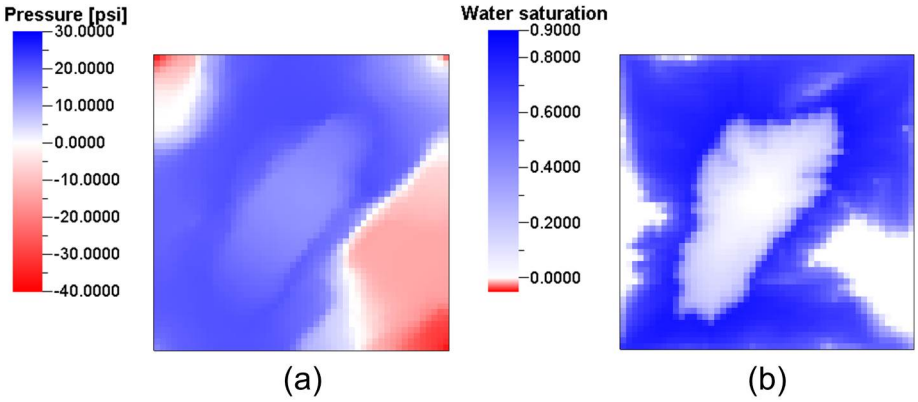

Fig. 3.9—Time-lapse observation data between 260 days and 1560 days. (a) Pressure change map, and (b) Water saturation change map.

The production data is available as water cut and bottomhole pressure at the wells. This choice of data follows that of the Brugge field case, which will be described in the next section.

Our approach involves first matching of the time-lapse pressure changes followed by matching of the saturation changes, using the pressure and saturation sensitivity calculations just discussed. Finally, well by well water cut matching is performed using the generalized travel time inversion method (He et al. 2002). Our reasoning behind the sequential approach is that the pressure data is well-suited to capture large-scale (global) variation whereas saturation and production data capture small-scale (local) variation. This is analogous to the structured approach to history matching that is widely practiced in the industry (Williams et al. 1998; Cheng et al. 2008).

Pressure change data integration results are shown in **Fig. 3.10a** and shows significant reduction in the objective function within a few iterations. The updated permeability field shown in **Fig. 3.11c** appears to identify the low permeability barrier located in the right lower side. Also, the time-lapse pressure change response improved significantly as shown in **Fig. 3.12c** compared to the initial model (**Fig. 3.12b**). Next, saturation changes are integrated into the updated model from the previous step. The reduction of the objective function with the number of iterations is shown in **Fig. 3.10b**. The time-lapse saturation change from this stage is shown in **Fig. 3.13d** and reveals further improvement over the pressure data integration as shown in **Fig. 3.13c**. Finally, the generalized travel time inversion is applied to match the well by well water cut data. The objective function reduction is shown in **Fig. 3.10c** and the production data history matching results are shown in **Figs. 3.14 and 3.15**.

The final model responses are well matched to the reference model both for bot-

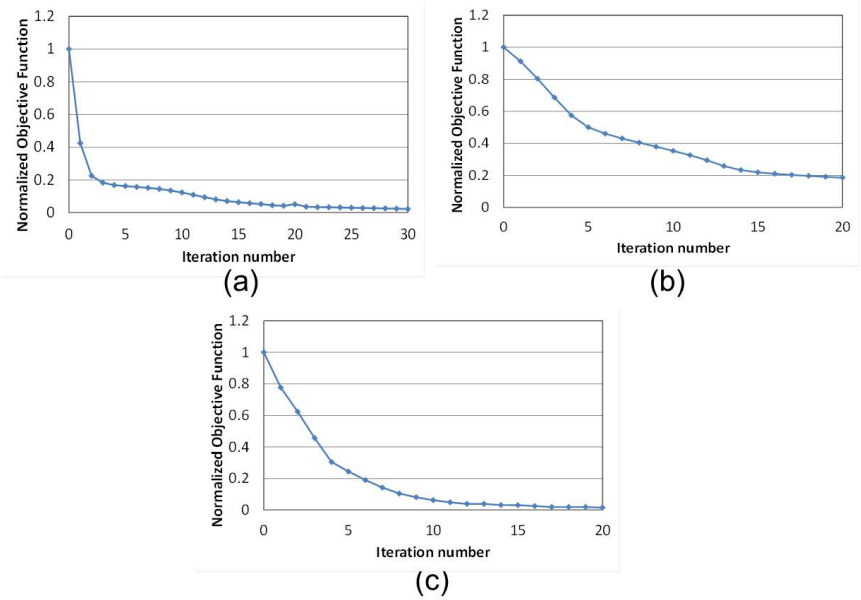

Fig. 3.10—Objective functions during inversion iterations. (a) Pressure change data integration, (b) Saturation change data integration and (c) Generalized travel time production data integration.

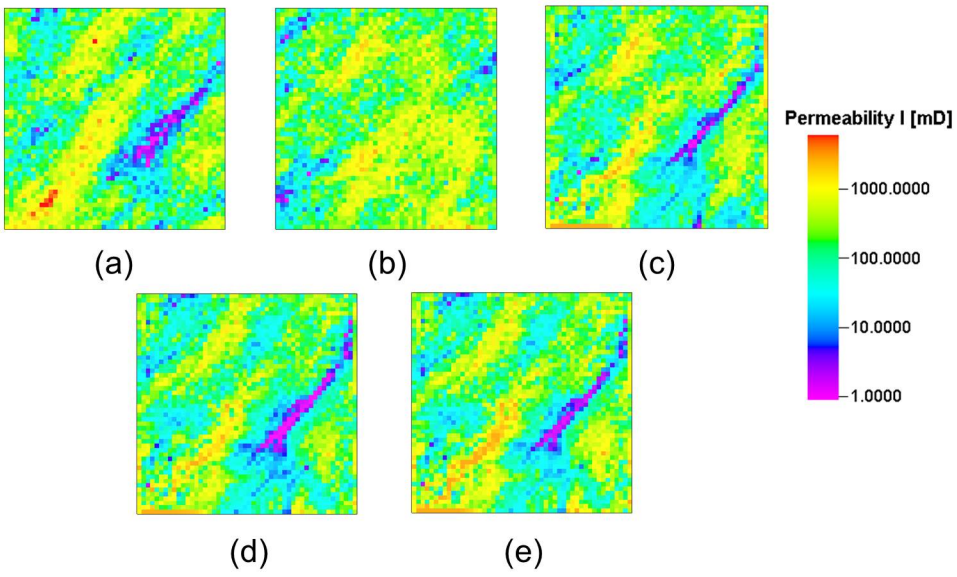

Fig. 3.11—Updated permeability fields comparisons. (a) Reference model, (b) Initial model, and (c) After pressure change data integration, (d) After water saturation change data integration, and (e) Final model after generalized travel time production data integration.

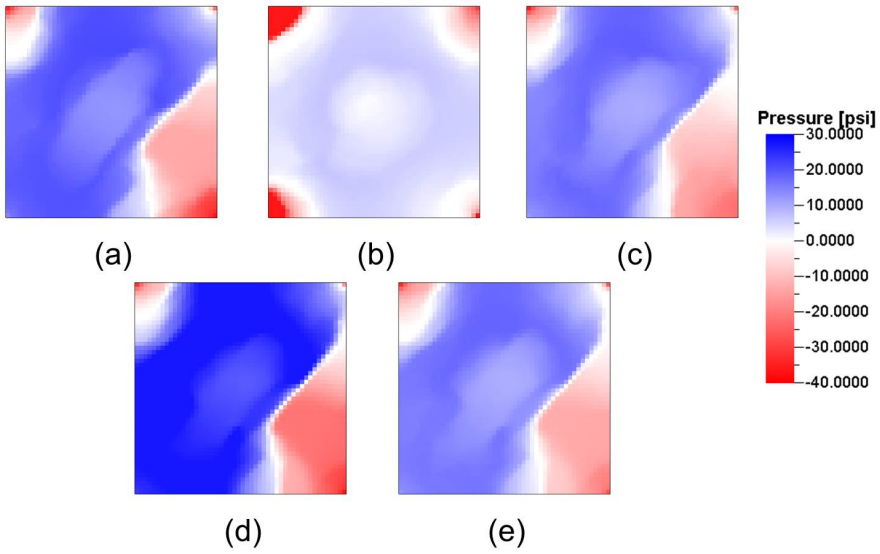

Fig. 3.12—Time-lapse pressure change comparisons. (a) Reference model, (b) Initial model, and (c) After pressure change data integration, (d) After water saturation change data integration, and (e) Final model after generalized travel time production data integration.

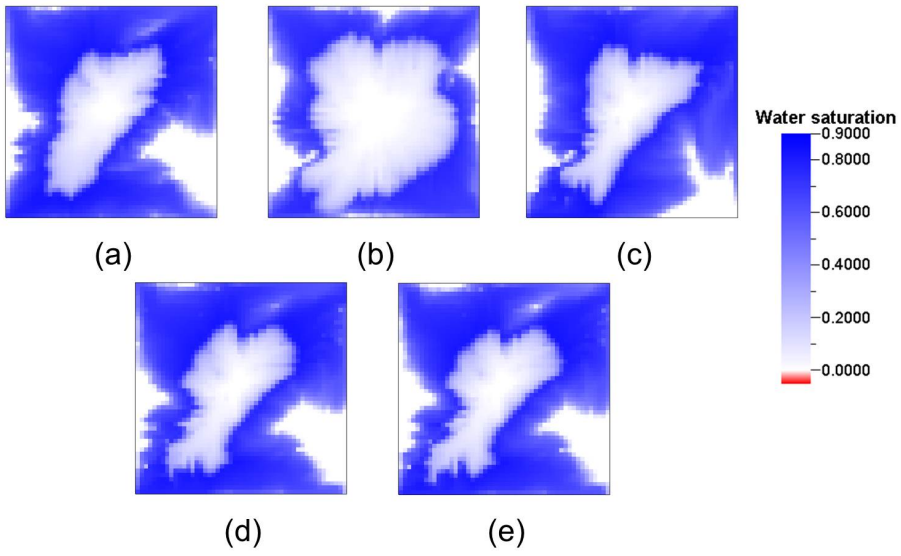

Fig. 3.13—Time-lapse water saturation change comparisons. (a) Reference model, (b) Initial model, and (c) After pressure change data integration, (d) After water saturation change data integration, and (e) Final model after generalized travel time production data integration.

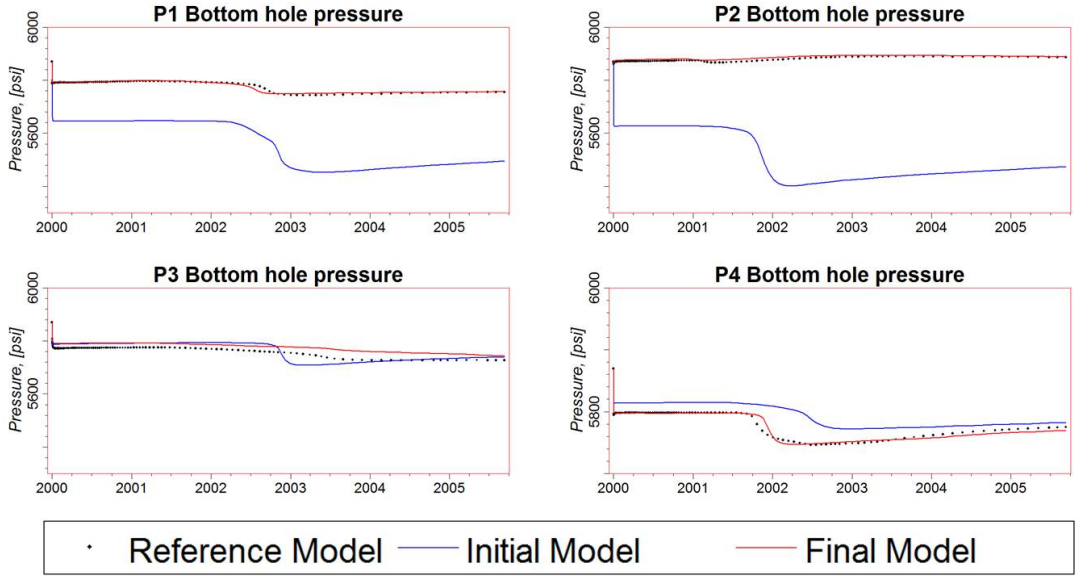

Fig. 3.14—Bottomhole pressure data history matching results. Reference model responses are plotted as dot points, initial model responses are in blue lines, and final updated model responses are in red lines.

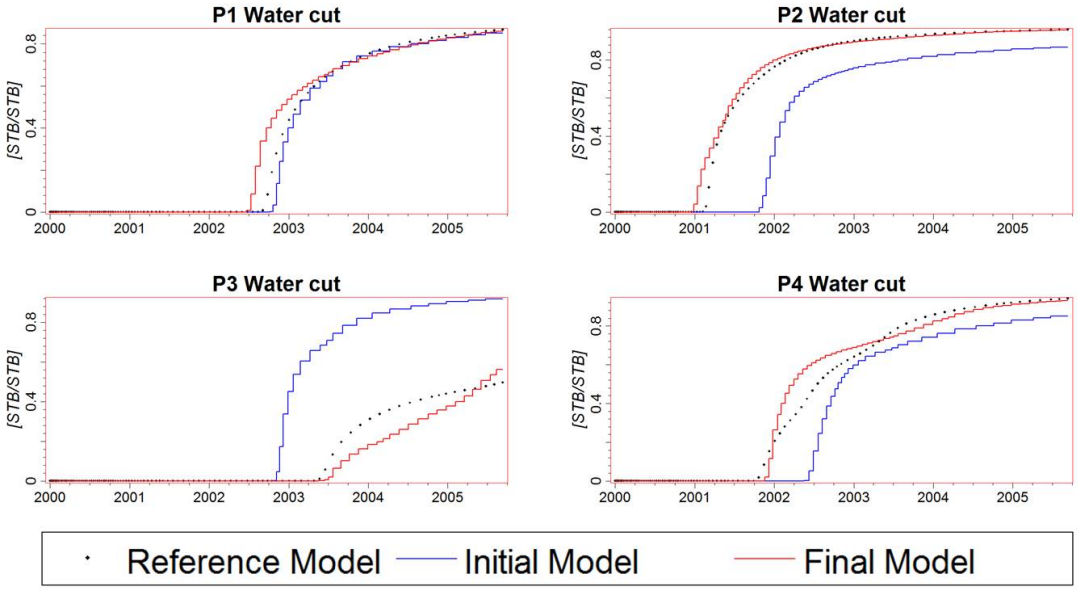

Fig. 3.15—Water cut data history matching results. Reference model responses are plotted as dot points, initial model responses are in blue lines, and final updated model responses are in red lines.

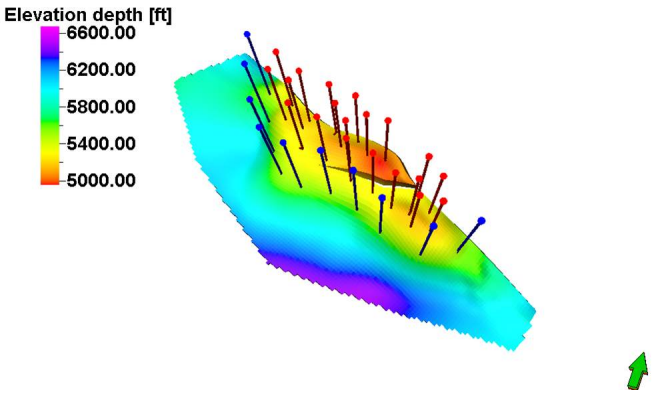

Fig. 3.16—Structure of the Brugge field showing the elevation depth (in feet) and 30 wells: producers (red color), and injectors (blue color).

tomhole pressure and water cut data with corresponding improvements of time-lapse pressure and saturation change responses as shown in **Figs. 3.12 and 3.13**. The permeability model updates during the inversion steps are compared in **Fig. 3.11**. These results confirm that the consistent integration of both time-lapse pressure and saturation changes together with production data can constrain the history matching solution effectively with our proposed approach.

3.5.2 The Brugge Field Case

The Brugge field case was designed for a SPE benchmark project to test the combined use of history matching and waterflooding optimization methods in a closed-loop workflow (Peters et al. 2010). The structure of the Brugge field consists of an east/west elongated half-dome with a large boundary fault at its northern edge and one internal fault with a modest throw as shown in **Fig. 3.16**.

The dimensions of the field are roughly 10 km × 3 km. The reservoir model contains more than 40,000 active grid cells, 20 producers located in the center of the dome and 10 infill water injectors located in the surrounding aquifer to provide additional pressure support. A total of 104 realizations were generated by four different

classes of geologic parameters: (1) facies association, (2) facies modeling, (3) porosity, and (4) permeability. The detailed descriptions of the realization construction can be found in Peters et al. (2010). In order to account for the uncertainty of the prior models in history matching, we test the proposed inversion method for four distinct realizations, namely realization 1, 33, 67 and 103 as shown in **Fig. 3.17**. Production data are given in the form of water and oil rates, and also bottom-hole pressure at each of the 20 producers for the 10 years of production. The reservoir is an under saturated oil reservoir (i.e., no solution gas). Inverted 4-D seismic data in terms of pressure and saturation changes between time-lapse of 10 years are also provided. Pressure and saturation changes were calculated as vertically averaged values over the four reservoir zones in total 9 layers (i.e., the Scheld, Maas, Wall, and Schie), representative for the seismic resolution with added noise (**Fig. 3.18**). We use these data sets as observation data to calibrate reservoir permeability to minimize the differences of the observed and simulated time-lapse pressure and saturation changes as well as the production data. One of the challenging aspects of this application is the long gap of the time-lapse data. During the 10 years of production, the reservoir drive mechanism has evolved from primary depletion to secondary recovery with the down-dip water injection. The streamlines depict this transition of the reservoir flow dynamics clearly as shown in **Fig. 3.19**. Accordingly, we need to account for the dynamic changes of the reservoir pressure and saturation to integrate the available time-lapse data (Rey et al. 2012).

First, pressure change data is utilized to calibrate the models. The inversion performance is shown in **Fig. 3.20a** for each of the four models. Next, water saturation change is integrated to update the models as shown in **Fig. 3.20b**. Finally, the generalized travel time inversion is applied to integrate water cut data into the models (**Fig. 3.20c**). The improvements in well by well production response

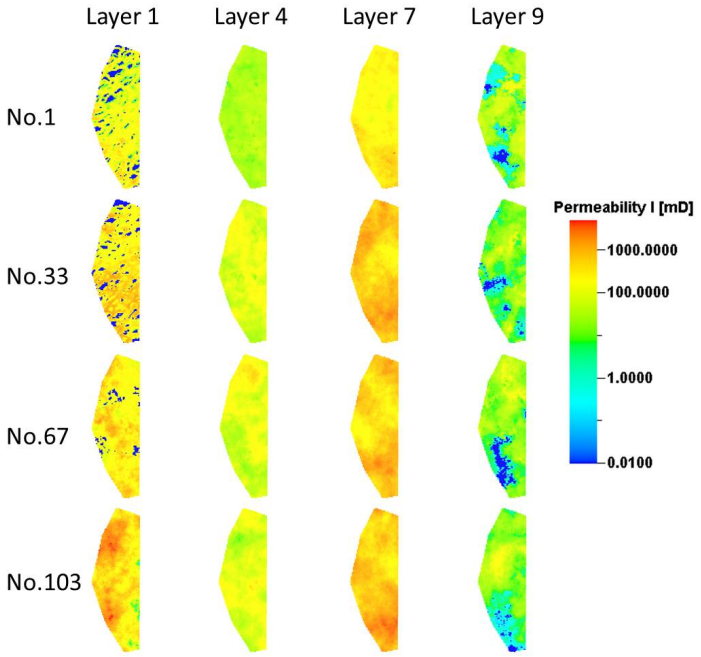

Fig. 3.17—Four realizations of the selected layers: namely Realization 1, 33, 67, and 103.

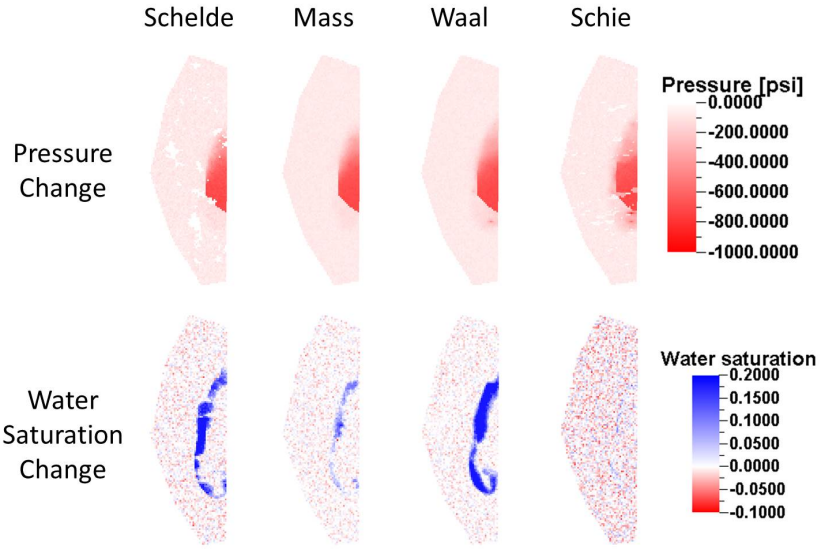

Fig. 3.18—Time-lapse pressure and water saturation changes vertically averaged over the four reservoir zones (from top Scheld, Maas, Waal, and Schie formations).

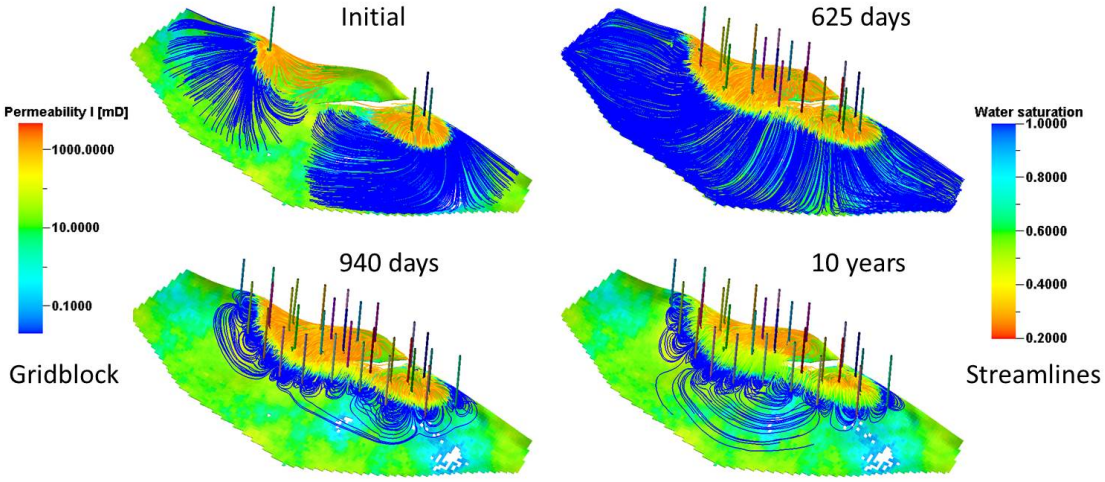

Fig. 3.19—Streamlines during the 10 years of production depicting reservoir flow dynamics: primary depletion (initial to 625 days) to secondary recovery with down-dip water injection (940 days to 10 years).

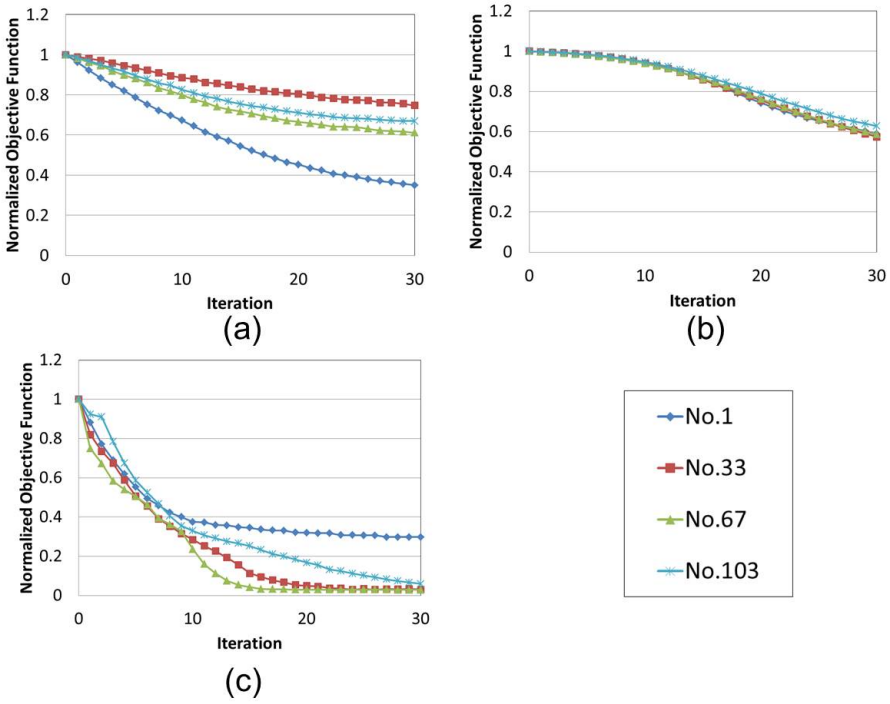

Fig. 3.20—Objective functions during inversion iterations. (a) Pressure change data integration, (b) Saturation change data integration, and (c) Generalized travel time production data integration.

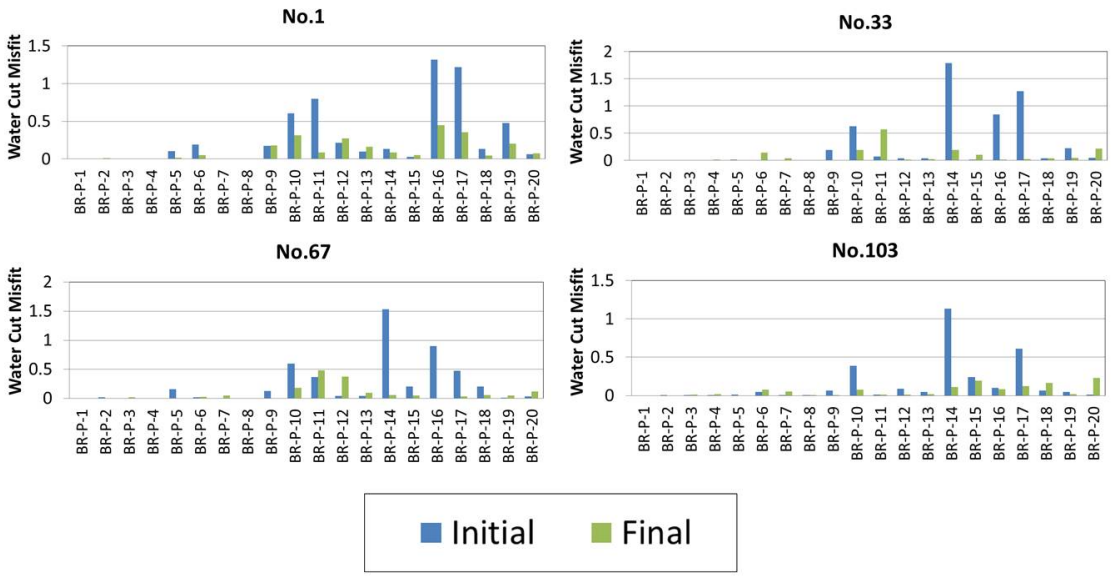

Fig. 3.21—Water cut data history matching results. Data misfit comparisons between the initial models and the final updated models for four realizations.

match are shown in **Fig. 3.21**. In particular, some improved well matching results from the realization No.67 are shown in **Fig. 3.22**. The final updated models are shown in **Fig. 3.23**. Compared to the initial models, major permeability changes occur in the Waal formation (layer 6, 7, 8), but overall geologic continuity is preserved for all realizations. The final model response in terms of pressure change and water saturation change for the Waal formation are compared in **Figs. 3.24 and 3.25**. Overall, the magnitude of pressure changes reduced from initial model responses for all realizations. As for water saturation changes, the improvements of the magnitude of changes and the distribution of water fronts are more evident in the final updated models. With these updated models, we can assess various schemes for production optimization, although this is not within the scope of this section (Alhuthali et al. 2008).

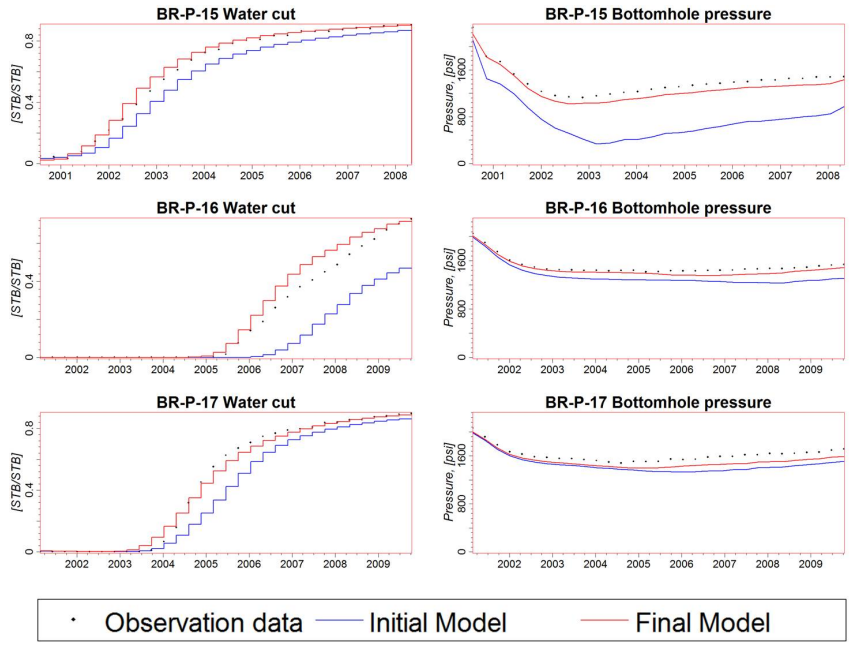

Fig. 3.22—Production data history matching comparisons between the initial model and the final updated model of realization No. 67.

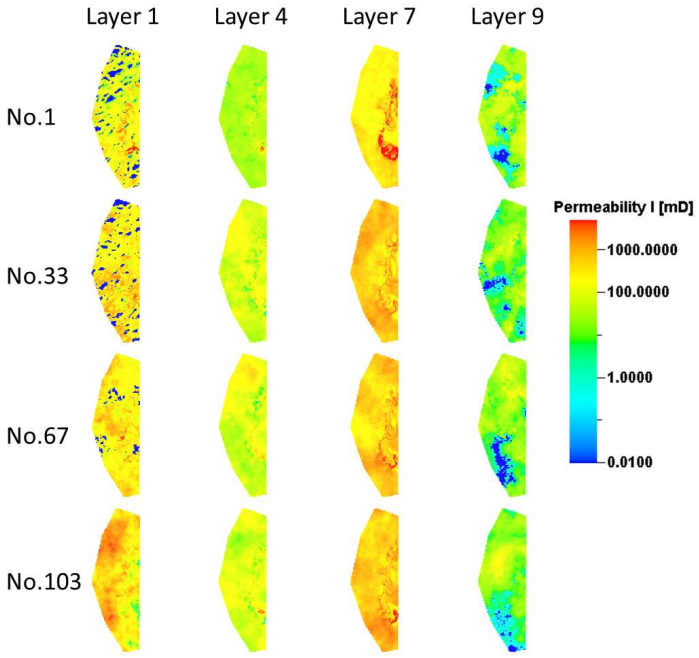

Fig. 3.23—Four final updated models of the selected layers: namely realization 1, 33, 67, and 103.

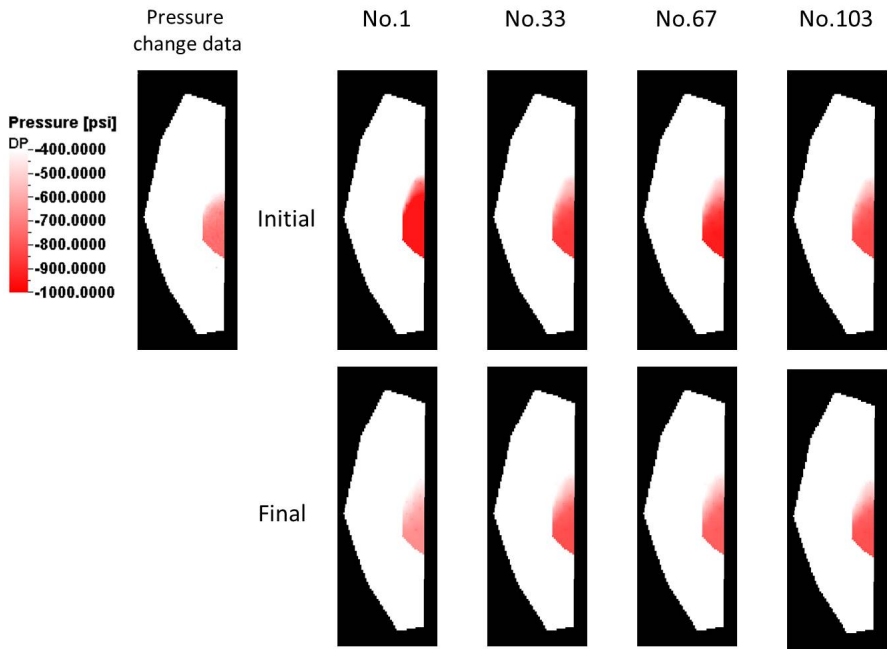

Fig. 3.24—Time-lapse pressure change comparisons between initial models and final updated models (from Waal formation).

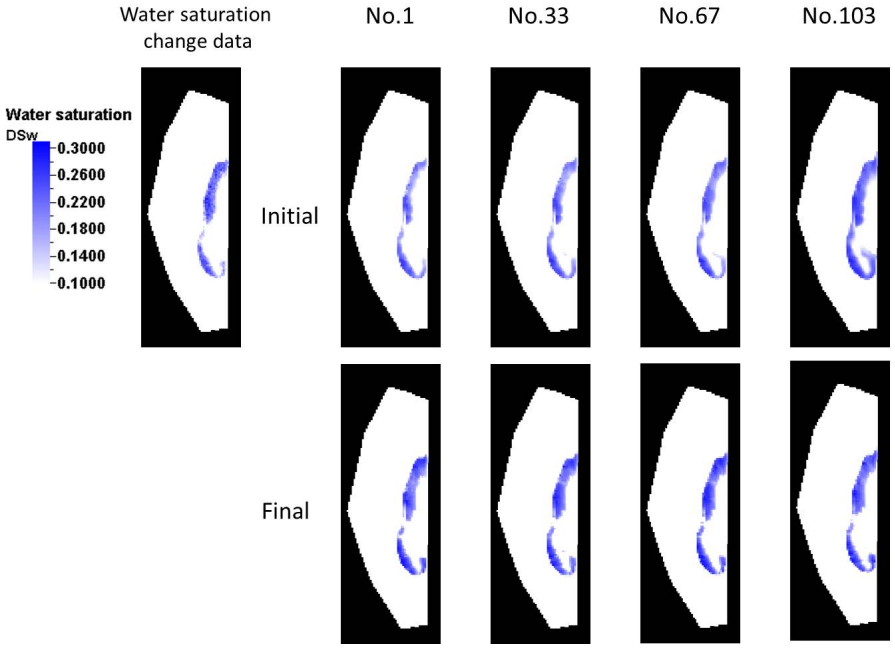

Fig. 3.25—Time-lapse water saturation change comparisons between initial models and final updated models (from Wall formation).

3.6 Conclusions

In this section we have presented an efficient history matching approach that integrates the time-lapse seismic derived pressure and saturation change data with well production data. Although our approach relies on streamline-based sensitivity calculations to relate pressure and saturation responses to the reservoir parameters, it can be applied with either streamline simulators or conventional finite difference simulators. For finite difference simulators, the streamline and time of flight can be computed via post processing of the velocity field (Cheng et al. 2005). We have demonstrated the effectiveness of our proposed approach through synthetic and the Brugge field applications. Some of the conclusions from this section are summarized below.

- We have proposed a novel methodology for streamline-based analytic approaches to compute parameter sensitivities that relate the time-lapse seismic derived pressure and saturation changes to reservoir properties.

- Our numerical experiments validate the proposed sensitivity calculations for the saturation and pressure drop by comparison with numerical perturbation method. However, unlike numerical perturbation, our proposed approach to sensitivity computations only requires a single forward simulation.

- Five-spot synthetic example shows the importance of accounting for both saturation and pressure changes in the reservoir responses in order to constrain the history matching solutions.

- The proposed approach can account for the model geologic uncertainty by updating ensemble of realizations as demonstrated in the Brugge field case.

4. INTEGRATION OF 4D SEISMIC AND PRODUCTION DATA FOR RESERVOIR MANAGEMENT-APPLICATION TO THE NORNE FIELD*

4.1 Summary

This section summarizes a structured workflow for time-lapse seismic and production data history matching and field-scale production optimization thorough the Norne field application. Our proposed method follows a two-step approach: global and local model calibrations. In the global step, we reparameterize the field permeability heterogeneity, at grid cell resolution, with a Grid Connectivity-based Transformation (GCT) as basis coefficient parameters and use a Pareto-based multi-objective evolutionary algorithm to integrate field cumulative production responses and time-lapse seismic derived acoustic impedance change data. The method generates a suite of solutions accounting for the trade-off in fitting production and seismic data.

In the local step, first the time-lapse seismic data is integrated using semi-analytical, streamline-derived sensitivities of acoustic impedance at grid cell resolution to perturbations in gridblock permeability, thus, capturing fluid movement in-between time-lapse seismic surveys. Next, well by well production data is integrated by using a generalized travel time inversion method to resolve fine-scale permeability variations between well locations.

For production optimization, we use the ensemble of history matched models and develop an optimal rate control strategy to maximize sweep efficiency by equalizing flood front arrival times at all producers while accounting for geologic uncertainty.

*Part of this section is from "Multiscale Parameterization and Streamline-based Dynamic Data Integration for Production Optimization: Application to the Norne Field" by Watanabe, S., Han, J., Ekkawong, P., Datta-Gupta, A., 2013. A presentation prepared for at the SPE Workshop "Integration of 4D Seismic & Production Data for Reservoir Management-Application to Norne" held in Trondheim, Norway 25-27 June. The view expressed in this section are the views of the authors and do not necessarily reflect the views of Statoil and the Norne license partners.

4.2 Introduction

The Norne field was discovered in December 1991 and development drilling began in August 1996. Oil production started in November 1997 and the field has been operated by Statoil. The field has high quality 4-D seismic data, production data and well logs in addition to the reservoir model. The geological model consists of five reservoir zones. They are the Garn, Not, Ile, Tofte and Tilje. Oil is mainly found in the Ile and Tofte Formations, and gas in the Garn formation. The sandstones are buried at the depth of 2,500-2,700 m. The porosity is in the range of 25-30% while permeability varies from 20 to 2,500 md (Steffensen and Karstad 1995; Osdal et al. 2006).

We demonstrate the practical feasibility of our approach by carrying out full field history matching of the Norne field. The reservoir model consists of 44,431 active cells and it contains 36 wells (9 injectors and 27 producers) as shown in **Fig. 4.1**. We consider the time frame from 1997 to 2006 as the history matching period. The actual simulation model containing all information and properties was provided by the operator. In addition, production and injection data from 1997 to the end of 2006, and multiple sets of 4-D seismic data for the same period (2003-2001, 2004-2003, 2006-2004) were provided. The production data include water, oil, and gas rates and bottom-hole pressures at the producers. The seismic data were externally processed and provided for the model calibration as near, mid, far, and full offset stacked 3-D volumes of the reflection amplitude together with the corresponding horizons for the top and base of the reservoir. Also, the time-lapse differences of the reflection amplitude were provided with interpreted horizons used for identification of movement of the water-oil contacts. The details of the data set can be found in Rwechugura et al. (2012).

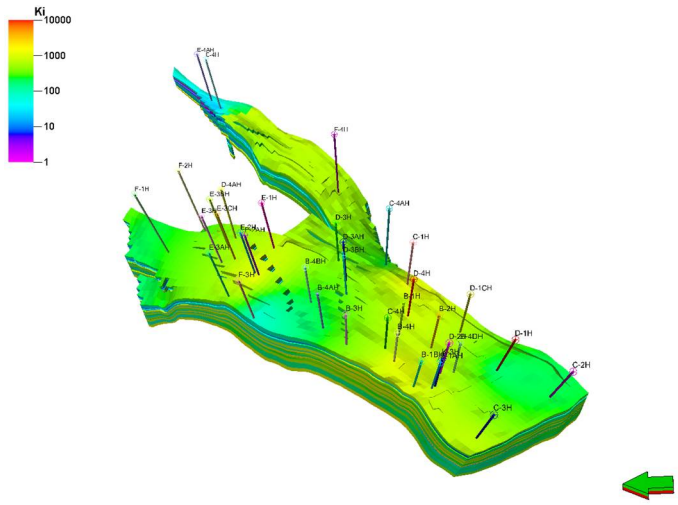

Fig. 4.1—Structure of the Norne field showing reservoir permeability.

4.3 Approach

4.3.1 Petro-Elastic Model

Unlike the Brugge field case in the previous section, where interpreted saturation and pressure changes are provided as part of the field data, this is a much more realistic case in which seismic response is provided instead. To our strategy of using streamline-based sensitivities to the inversion problem, we now need to introduce a petro-elastic model (PEM) and develop seismic response (acoustic impedance) sensitivities to changes in reservoir properties, as we have done for pressure and saturation sensitivities in the previous section.

A petro-elastic model is a set of equations which relates reservoir properties (pore volume, pore fluid saturations, reservoir pressures and rock composition) to seismic rock elastic parameters (P-wave and S-wave velocities, V_P and V_S, respectively). Variations in rock elastic properties are functions of temperature, compaction, fluid saturation and reservoir pressure, although we may neglect the effects of tempera-

ture in this field. The Gassman equation (1951) and Hertz-Mindlin contact theory (Mindlin 1949) are used to estimate seismic rock elastic parameter changes caused by fluid saturation and reservoir pressure changes, respectively. The Hertz-Mindlin model is used to compute seismic rock elastic parameter changes from pressure changes (Mavko et al. 1998). The effective bulk modulus of a dry random identical sphere pack are given by

$$K_{HM} = K_{ma} \sqrt[n]{P_{eff} \Big/ (P_{ext} - P_i)}, \tag{4.1}$$

where K_{HM} is the bulk modulus at critical porosity (Dadashpour et al. 2009, 2010). Here, P_{eff} is the effective pressure, which is the difference between the lithostatic pressure, P_{ext} and the hydrostatic pressure, P (Christensen and Wang 1985), K_{ma} is the bulk modulus of the matrix, and n is the coordination number. For the Norne field application, the initial pressure, P_i is set to 270 bar and the lithostatic pressure depends on the true vertical depth (TVD) as given by

$$P_{ext} = 0.0981 \times (9 \times 10^{-5} \times \text{TVD} + 1.7252) \times \text{TVD}. \tag{4.2}$$

The Hertz-Mindlin theory assumes that velocity varies with P_{eff} raised to the 1/6 th power, while some laboratory measurements on samples suggest other values. We use n equal to 5 in Eq. (4.1) from the literature (Dadashpour et al. 2009) for this field application.

The Gassman equation expresses the bulk modulus of a fluid saturated rock from three terms: (1) the bulk modulus of the mineral matrix, K_{HM} , (2) the bulk modulus of the porous rock frame, K_{fr} , (3) the bulk modulus of the pore-filling fluids, K_f as

given by the following formula (Dadashpour et al. 2009),

$$K_{sat} = K_{fr} + \frac{(K_{HM} - K_{fr})^2}{K_{HM}\left(1 - \phi + \phi\frac{K_{HM}}{K_f} - \frac{K_{fr}}{K_{HM}}\right)}. \tag{4.3}$$

Here ϕ is the effective porosity of the medium and the bulk modulus of the pore fluids (oil, water, and gas), K_f is estimated by Wood's law given (Reuss 1929) as

$$\frac{1}{K_f} = \frac{S_o}{K_o} + \frac{S_w}{K_w} + \frac{S_g}{K_g}. \tag{4.4}$$

Here S_o, S_w and S_g are oil, water and gas saturations, respectively, and K_o, K_w, and K_g are bulk moduli for oil, water, and gas, respectively. For the Norne field application, the rock elastic properties are provided in **Table 4.1**. The density of the saturated rock is given by the weighted average of the densities of the components:

$$\rho_{sat} = (1 - \phi)\rho_{ma} + \phi(S_o\rho_o + S_w\rho_w + S_g\rho_g). \tag{4.5}$$

Here ρ_o, ρ_w, ρ_g and ρ_{ma} are the densities of oil, water, gas and the rock matrix, respectively. With the saturated rock bulk modulus and shear modulus and density, we can compute the compressional (p-wave) velocity for an isotropic, layered, elastic medium (Kennett 1983) as

$$V_P = \sqrt{\frac{K_{sat} + \frac{4}{3}G_{fr}}{\rho_{sat}}}. \tag{4.6}$$

Here the shear modulus, G_{fr} is the frame shear modulus which is not affected by

TABLE 4.1—INPUT PARAMETERS FOR THE PETRO-ELASTIC MODEL IN NORNE FIELD.			
Shale properties			
Shale type 1 (Not formation)	P-wave velocity, m/s	Vpsh1	3200
	S- wave velocity, m/s	Vssh1	1600
	Shale density, kg/m^3	ρsh1	2300
Shale type2 (overburden)	P-wave velocity, m/s	Vpsh2	3350
	S- wave velocity, m/s	Vssh2	1800
	Shale density, kg/m^3	ρsh2	2450
Shale type 3 (underburden)	P-wave velocity, m/s	Vpsh3	3350
	S- wave velocity, m/s	Vssh3	1900
	Shale density, kg/m^3	ρsh3	2450
Sand properties			
Garn formation (layer 1-3)	Frame bulk modulus, Gpa	K_{fr}	18.8-36.8ϕ
	Frame shear modulus, Gpa	G_{fr}	11.8-21.4ϕ
	Matrix bulk modulus, Gpa	K_{ma}	37
	Matrix density, kg/m^3	ρ_{ma}	2650
Garn formation (layer 5-22)	Frame bulk modulus, Gpa	K_{fr}	18.5-27.4ϕ
	Frame shear modulus, Gpa	G_{fr}	10.9-13.0ϕ
	Matrix bulk modulus, Gpa	K_{ma}	37
	Matrix density, kg/m^3	ρ_{ma}	2650
Fluid properties			
Fluid bulk modulus (at temperature 98.3 °C) from Batzle and Wang (1992)	Oil bulk modulus, Gpa	Ko	1.35
	Water bulk modulus, Gpa	Kw	2.79
	Gas bulk modulus, Gpa	Kg	6.49×10-2
Fluid density	Oil density, kg/m^3	ρo	860
	water density, kg/m^3	ρw	1000
	Gas density, kg/m^3	ρg	190

fluid saturations. The acoustic (p-wave) impedance can be computed as

$$Z_P = \rho_{sat} V_P = \sqrt{\rho_{sat}\left(K_{sat} + \frac{4}{3}G_{fr}\right)}. \tag{4.7}$$

With the above PEM model for the Norne field application, we examined the sensitivity of the acoustic impedance calculation with pressure and saturation changes. In a simple two phase (oil, water) system, **Fig. 4.2a** shows the increase of acoustic

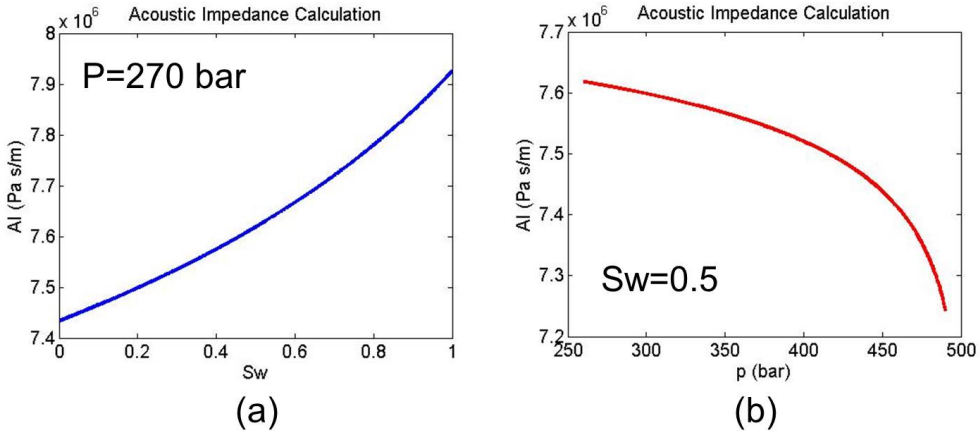

Fig. 4.2—Acoustic impedance calculation sensitivity by PEM model in oil and water 2 phase system, (a) with respect to water saturation changes under a fixed pressure (270 bar) and (b) with respect to pressure changes under a fixed saturation value (Sw=0.5).

impedance with increasing water saturation for a fixed pressure. **Fig. 4.2b** shows the decrease of acoustic impedance with increasing pressure with fixed saturation values.

4.3.2 Seismic Data Processing

The first step in our data calibration procedure is to invert the seismic volumes of reflection amplitude to changes in acoustic (p-wave) impedance. Using a commercial software, we conduct seismic data processing which consists of (1) time to depth data conversion, (2) well log quality check and acoustic impedance log calculation, and (3) genetic inversion for generating an acoustic impedance map from the seismic amplitude data. The detail procedures are described in **APPENDIX C**. As for the post-stack seismic sections, we decided to use near-offset stacked data set, because the acoustic (p-wave) impedance changes are more evident in the small angle reflection waves in AVO analysis (Aki and Richards 1980). A mathematical justification is explained in **APPENDIX B.4**.

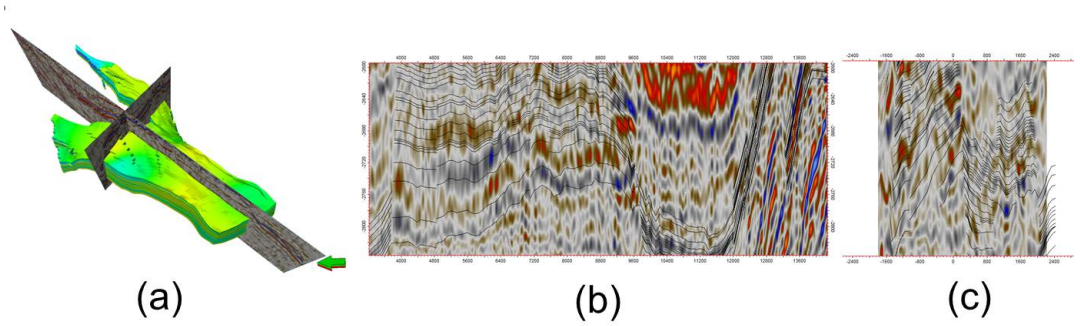

Fig. 4.3—Time to depth data conversion. (a) Reservoir model intersected by the depth domain seismic amplitude inline and crossline slices, (b) the Inline slice with reservoir model layer horizons, and (c) the crossline slice with reservoir model layer horizons.

Time to depth data conversion is achieved by using a velocity model that the operator used for the reservoir model construction. The layering of the reservoir model is consistent with the depth converted seismic amplitude data as shown in **Fig. 4.3**. Well log data quality is reviewed especially for the density logs and the P-wave sonic logs with the aim of computing P-wave acoustic impedance at the well locations shown in **Fig. 4.4**. We adapt a genetic inversion of the seismic amplitude, as proposed by Veeken et al. (2009). The method only requires the post-stack seismic cube as input. The acoustic impedance logs at the wells are used as training data for a neural network to construct the non-linear operator that transforms the seismic traces into the equivalent acoustic impedance response. The weights of the operator are updated by a genetic algorithm to minimize the difference between the predicted acoustic impedance response and the training acoustic impedance logs at wells.

The neural network derived operator is applied to the seismic cube to generate acoustic impedance map estimates as shown in **Fig. 4.5**. The acoustic impedance changes correspond to the interpreted motion of the water oil contact between surveys. They are consistent with the PEM model responses: the positive change reflects

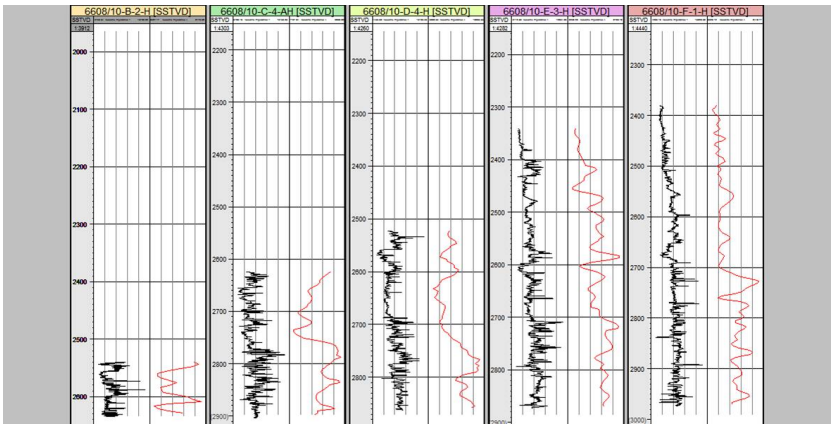

Fig. 4.4—The acoustic impedance log comparisons. The calculated acoustic impedance log (black) and the response extracted from the acoustic-impedance cube as a result of genetic inversion (red).

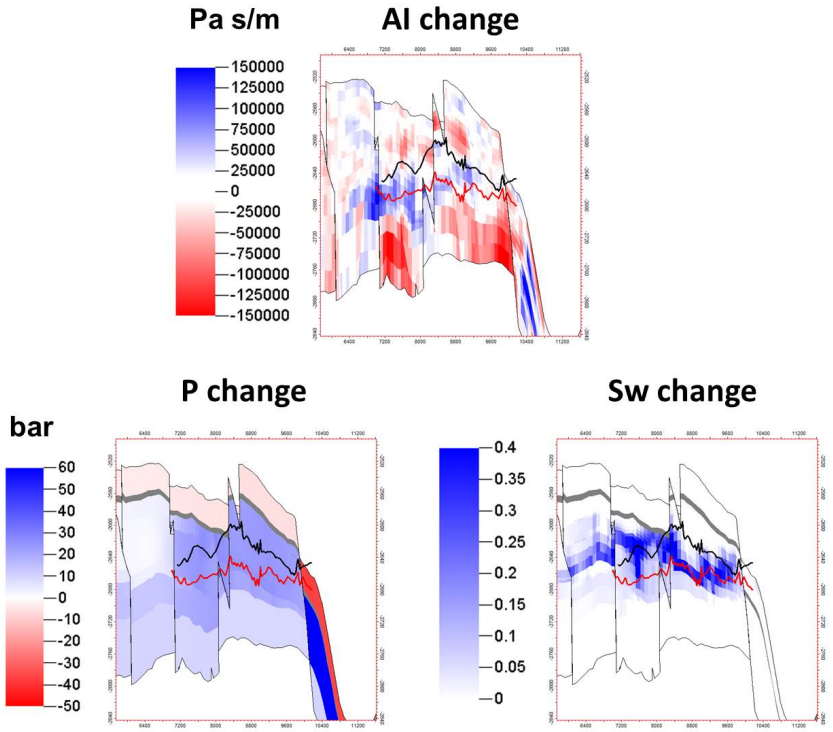

Fig. 4.5—Acoustic impedance change data in an inline slice between 2003 and 2001 surveys from genetic inversion. Water oil contact interpretations are superimposed (red line is at 2001 survey and black line is at 2003 survey). The water saturation and pressure changes from the initial model are compared.

the aquifer encroachment and the negative changes below the water oil contact corresponds to the simulated pressure increases in **Fig. 4.5**. The cross validation of the predicted acoustic impedance values from the genetic inversion and the training acoustic impedance logs show overall agreement (**Fig. 4.4**).

4.3.3 Global to Local Hierarchical History Matching Workflow

The reservoir model provided by the operator was already calibrated to match the reservoir energy (regional pressure and pore volume). They adjusted fault transmissibility multipliers, regional relative permeability parameters, and large-scale absolute permeability and porosity heterogeneity using regional and constant multipliers. Our objective was to minimally update the permeability at locations and scales required to improve large scale transport within the reservoir induced by the production, water injection and aquifer support, but to otherwise leave the prior unchanged. We apply a hierarchical history matching workflow that consists of two stages (Yin et al. 2011): a global update and a local update. For the global update, the geological model is first parameterized using a Grid Connectivity Transform (GCT) (Bhark et al. 2011). It is a linear transformation where the heterogeneity is updated in a transform domain that is characterized by the spectral modes of the reservoir model grid. This change of basis from the spatial to spectral domain is performed by multiplication of the heterogeneity field with the GCT basis, which is constructed from the eigenvectors of a grid Laplacian. This parameterization method is efficient for parameter estimation by reducing the parameter dimensionality. A discrete spatial field is mapped to the transform domain using orthogonal transforms,

$$\mathbf{v} = \mathbf{\Phi}^{\top}\mathbf{u} \Longleftrightarrow \mathbf{\Phi}\mathbf{v}, \tag{4.8}$$

where $\mathbf{u}$ represents a spatial field and has dimension $N \times 1$, where N is the discretization of the property field. The column vector $\mathbf{v}$ is M-length spectrum of transform coefficients, or parameter set in the transform domain, and $\mathbf{\Phi}$ is a $(N \times M)$ matrix containing M-columns that define the discrete basis functions, each of length N. For model calibration, a spatial multiplier field has been posed in the multiplicative formulation as follows,

$$\mathbf{u} = \mathbf{u}_0 \circ \mathbf{\Phi v}, \tag{4.9}$$

where $\mathbf{u}_0$ is the prior property field, also called initial model, and $\mathbf{\Phi v}$ defines the multiplier field in the spatial domain and $(\circ)$ is the element-wise multiplication (Schur product). This honors the prior permeability heterogeneity in the model updates.

Further, we utilize a Pareto-based multi-objective history matching workflow proposed by Park et al. (2013) to update the GCT coefficients leading to the global changes in the geologic model. This approach is particularly well suited for minimizing the multiple, and potentially conflicting, objectives involved in matching both seismic data and production data. For the local update, the gridblock permeability changes are introduced via the streamline-based inversion algorithm, introduced in the current study. The time-lapse acoustic impedance changes and well by well water cut production data are further integrated and the fine scale permeability variations between well locations are refined. The diagram of the workflow is shown in **Fig. 4.6**.

Before the permeability adjustment, based on the previous history matching report of E-segment of Norne field (Rwechungura et al. 2012), the history improvement at well E-3AH required lowering of the WOC in layers 1 through 3 from 2,618.0 m to 2,648.2 m TVD, increasing the oil rim by this difference. The initial oil and water phase rates at this well were grossly under- and over-predicted, respectively. The gas

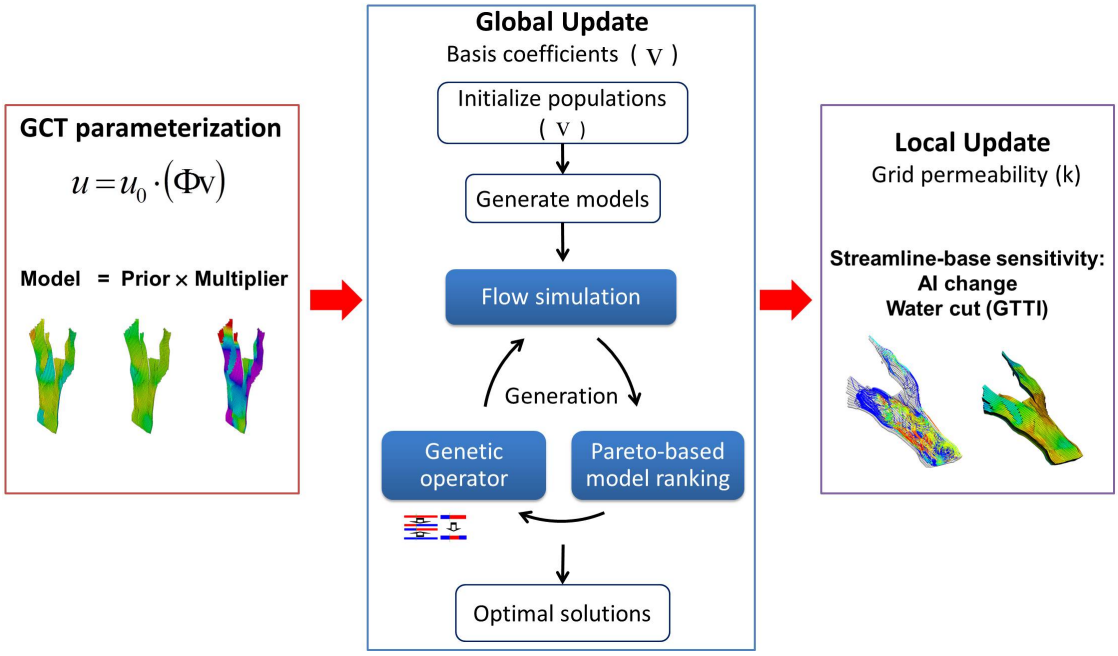

Fig. 4.6—Global to local hierarchical history matching workflow.

rate was approximately matched. In the simulation model, E-3AH has seven completion intervals in layers 1 and 2 that intersect the WOC. Therefore, adjustment of permeability, relative permeability or other transport parameters was unable to change the produced phase proportions. The well is fluid volume rate controlled in the simulation model, and because this net volume target was met, the evident choice to re-apportion the water and oil phase rates was to lower the WOC. Similarly, for C and D segment of Garn formation, we changed the WOC from 2,692.0 m to 2,658.2 m TVD to increase the level of initial water cut response at well D-4AH.

For the global update, we first parameterize the permeability field by each layer individually to preserve the vertical stratification. The GCT parameterization of a multiplier field is shown in **Fig. 4.7**. In this case, we used a total of 420 coefficients (20 basis vectors per layer × 21 active layers) to represent the geologic model consisting of 44,431 active cells.

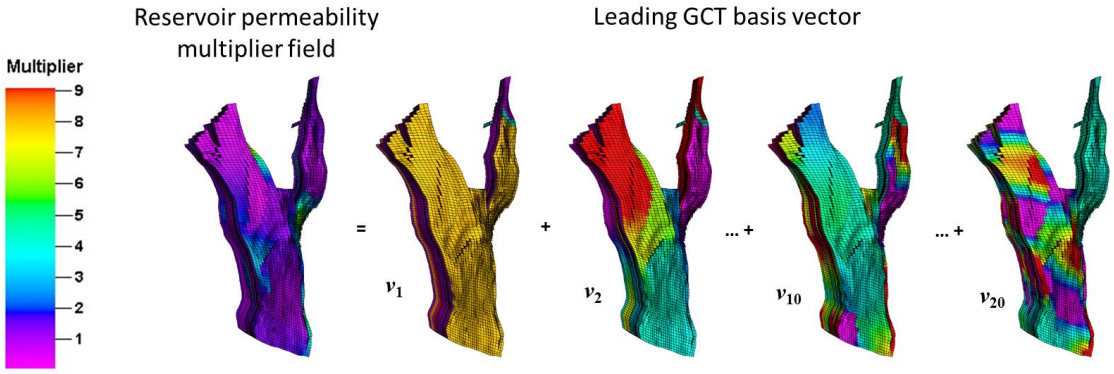

Fig. 4.7—Parameterization of the permeability multiplier field as the weighted linear combination of leading GCT basis vectors.

As for the Pareto-based multi-objective minimization, we define three objective functions: (1) gridblock acoustic impedance change misfit ($AI = Z_p$), (2) cumulative field water production ($FWPT$) misfit, and (3) cumulative field gas production ($FGPT$) misfit expressed as

$$obj1 = \sum_{time=1}^{3} \sqrt{\sum_{i=1}^{Ncell} \left(\delta AI_{i,time}^{\text{obs}} - \delta AI_{i,time}^{\text{cal}}\right)^2}, \tag{4.10}$$

$$obj2 = \sum_{j=1}^{Nwell} \sqrt{\sum_{i=1}^{Ntime} \left(FWPT_{i,j}^{\text{obs}} - FWPT_{i,j}^{\text{cal}}\right)^2}, \tag{4.11}$$

$$obj3 = \sum_{j=1}^{Nwell} \sqrt{\sum_{i=1}^{Ntime} \left(FGPT_{i,j}^{\text{obs}} - FGPT_{i,j}^{\text{cal}}\right)^2}, \tag{4.12}$$

Here $time$ is the time-lapse period, $Ncell$ is the total number of gridblocks, $Nwell$ is the total number of history matching wells, and $Ntime$ is the total number of timesteps. **Fig. 4.8** shows the results of the multi-objective function minimization in the global step of the model calibration. The Pareto-based evolutionary algorithm produces a suite of optimal solutions from the diverse initial population around the prior model in a multi-dimensional objective space. In the two-dimensional projection

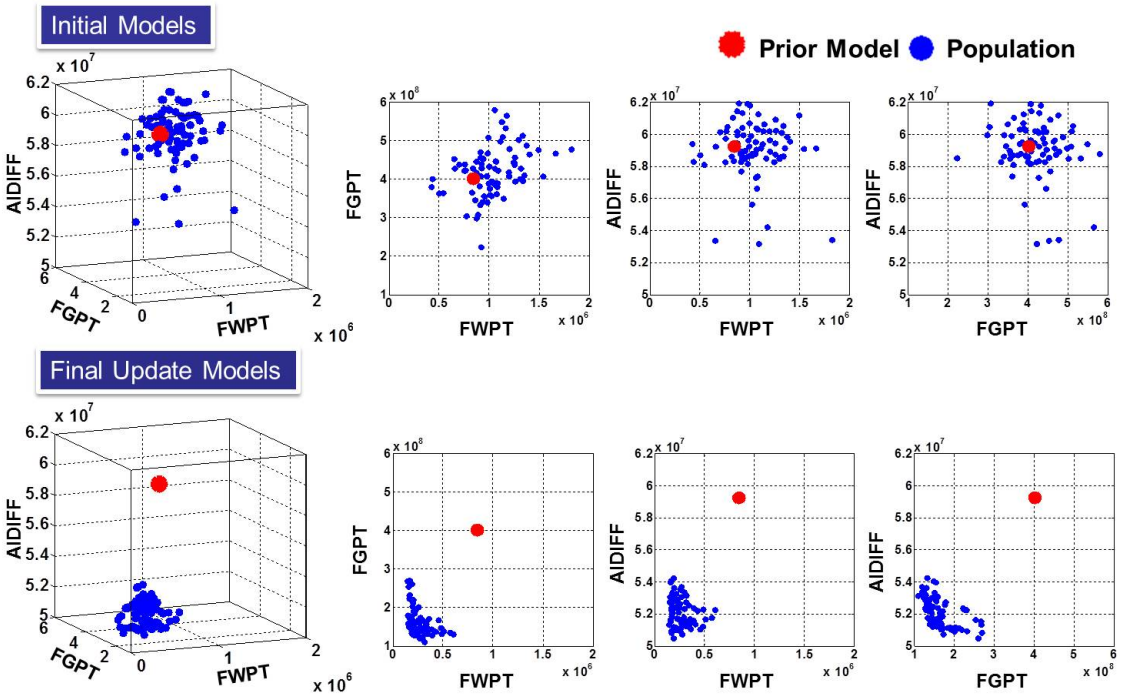

Fig. 4.8—Multi-objective function comparisons between initial models and the final models in the global step model calibration.

spaces in Fig. 4.8, the Pareto-fronts are clearly shown to depict the trade-off between objectives.

4.3.4 Time-Lapse Acoustic Impedance Change and Production Data Integration

After the global calibration step, we select a few candidate models for the local updates by a cluster analysis in the objective space as shown in Fig. 4.8. For the local update, we need the sensitivity of the acoustic impedance with respect to gridblock permeability. This can be obtained via a chain rule,

$$S_{Z_P} = \frac{\delta d_{Z_P}}{\delta k} = \left[\frac{\partial Z_P}{\partial S_w} \frac{\delta S_w}{\delta k} + \frac{\partial Z_P}{\partial S_g} \frac{\delta S_g}{\delta k} + \frac{\partial Z_P}{\partial P} \frac{\delta P}{\delta k} \right]. \tag{4.13}$$

Here the partial derivatives of acoustic impedance, $\frac{\partial Z_P}{\partial S_w}$, $\frac{\partial Z_P}{\partial S_g}$, and $\frac{\partial Z_P}{\partial P}$ are computed by numerical perturbation from the current saturation and pressure gridblock values using Eq. (4.7), while water saturation sensitivity $\frac{\delta S_w}{\delta k}$ is computed by Eq. (3.26). Notice that we have ignored porosity dependence in Eq. (4.13) and assumed that the changes in porosity because of compaction are not significant. For the gas saturation sensitivity, $\frac{\delta S_g}{\delta k}$, we follow the same derivation as for the water saturation sensitivity in Eq. (3.26). This assumption applies mainly for gas-oil two phase system near the top layers of the Norne field where the free gas cap and oil rim are located. For the pressure sensitivity we utilize the pressure drop sensitivity given by Eq. (3.35).

As discussed before, our history matching follows a sequential approach. To start with, the pressure effects on acoustic impedance changes are integrated to calibrate the model. Next, the saturation effects on the acoustic impedance changes are integrated to update the model. Water saturation sensitivity and gas saturation sensitivity are separately integrated in the inversion process. The diagram of the local step model calibration workflow is shown in **Fig. 4.9**. The inversion performance for acoustic impedance change is shown in **Fig. 4.10** for one of the models. The majority of the reduction of the acoustic impedance change data misfit was achieved in the global step of the model calibration. Finally, the generalized travel time inversion is applied to integrate water cut data. The well by well water cut responses are improved as shown in **Fig. 4.11**. The final updated model is shown in **Fig. 4.12**. The final model responses in terms of acoustic impedance changes are compared in **Fig. 4.13**.

For the second time-lapse period (2004-2003), a large negative time-lapse acoustic impedance change (red color) misfit in the prior model in the north right part of

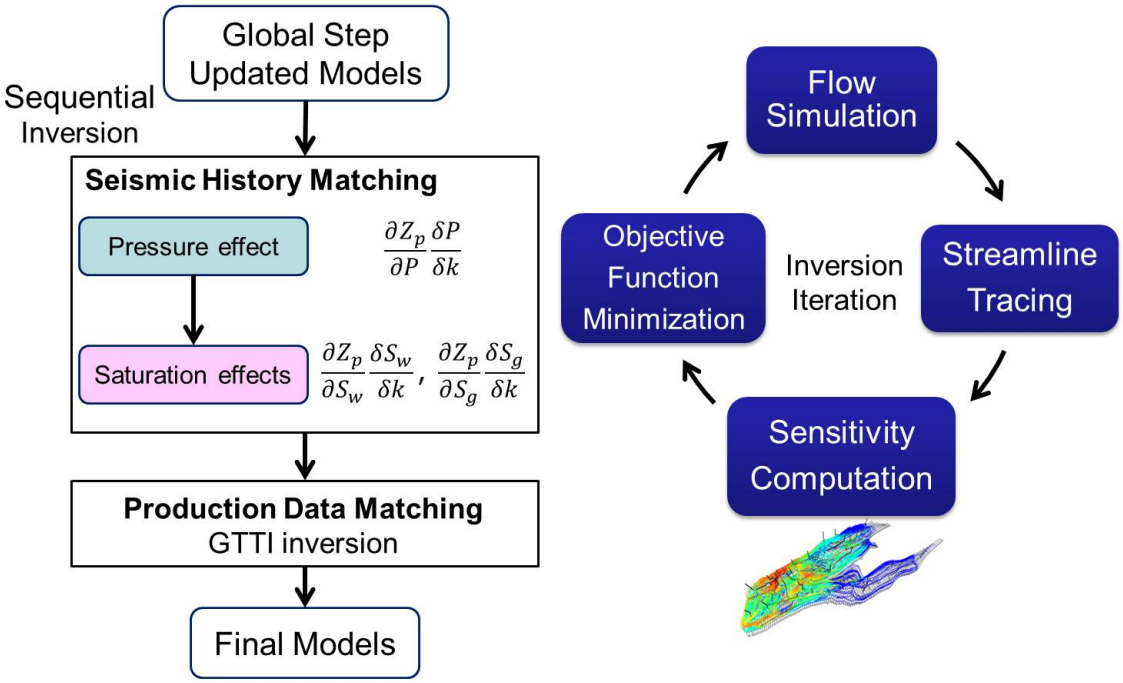

Fig. 4.9—Local step streamline-based model calibration workflow.

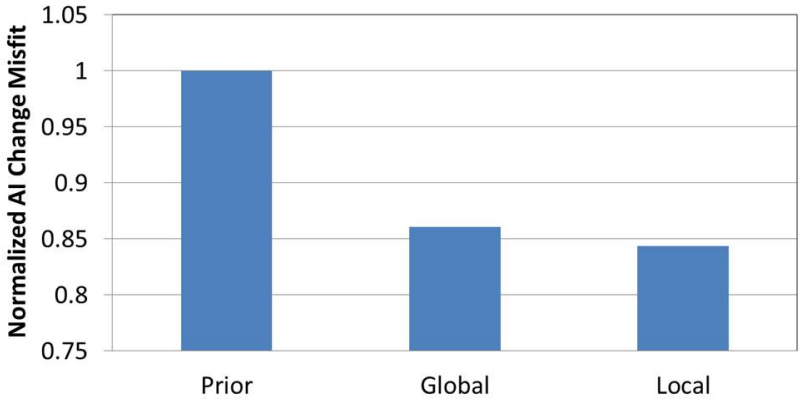

Fig. 4.10—The objective function misfit for acoustic impedance change data integration comparisons among the prior model, global step calibrated model, and the final updated model from the local step calibration.

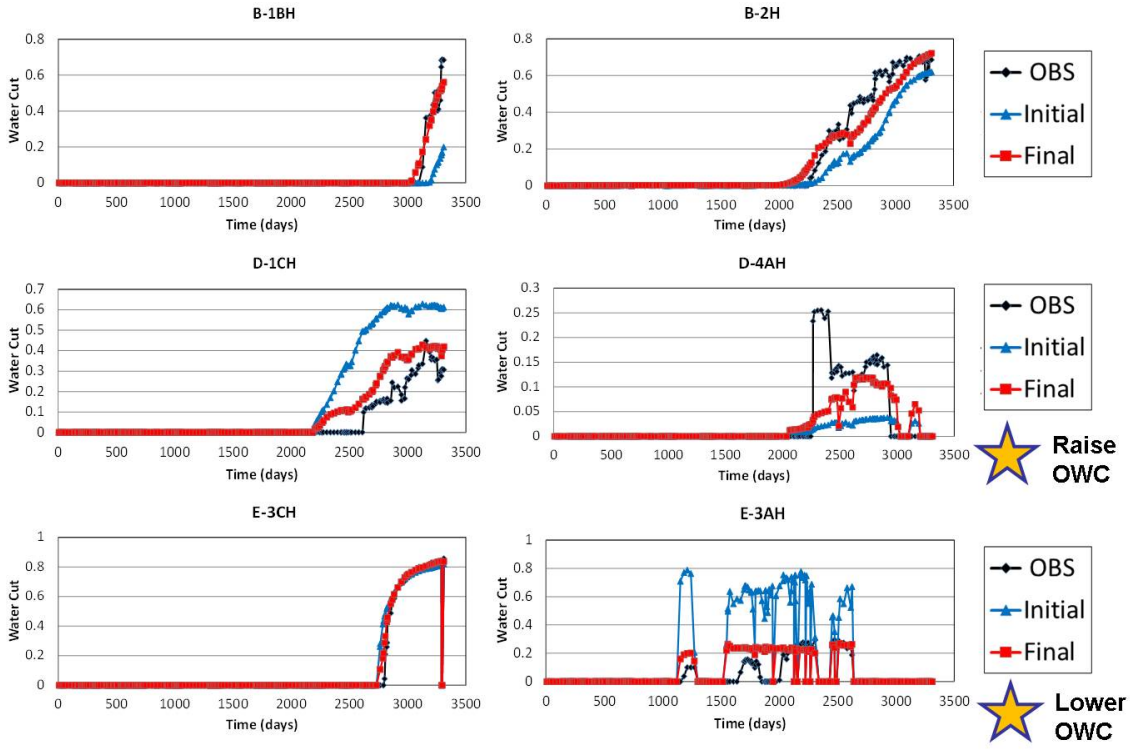

Fig. 4.11—Water cut production data history matching comparisons between the initial model and the final updated model.

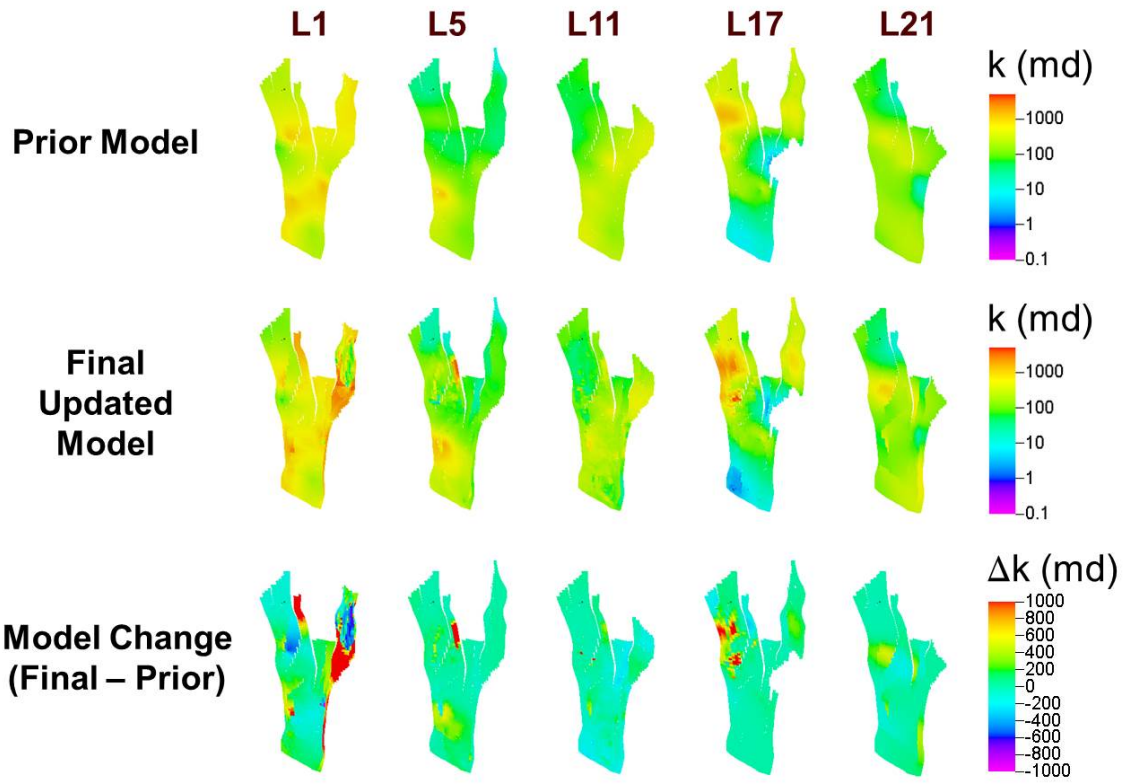

Fig. 4.12—Permeability model update comparison by layers. The prior model (Top), The final updated model (middle), and the model changes between the prior and the final models.

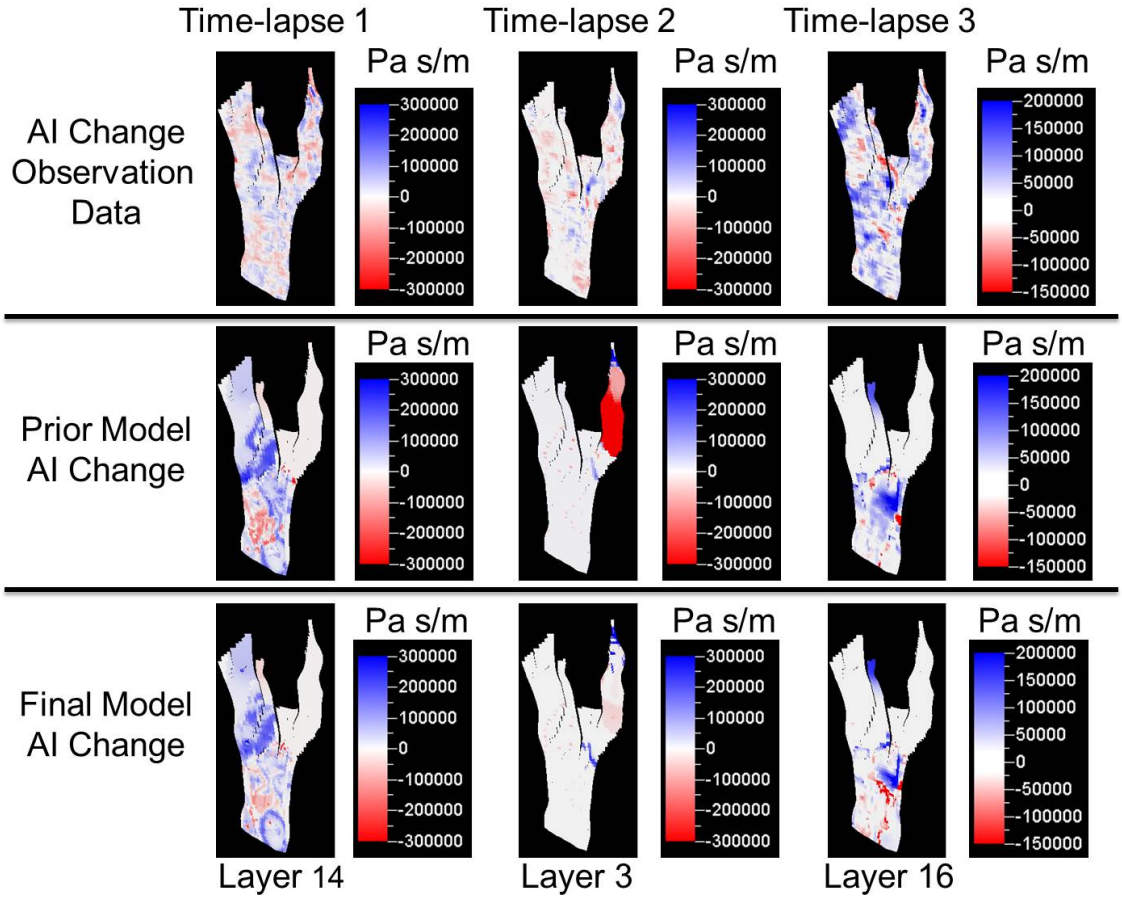

Fig. 4.13—Time-lapse acoustic impedance changes comparisons in selected layers among the observation data, the prior model responses and the final updated model responses.

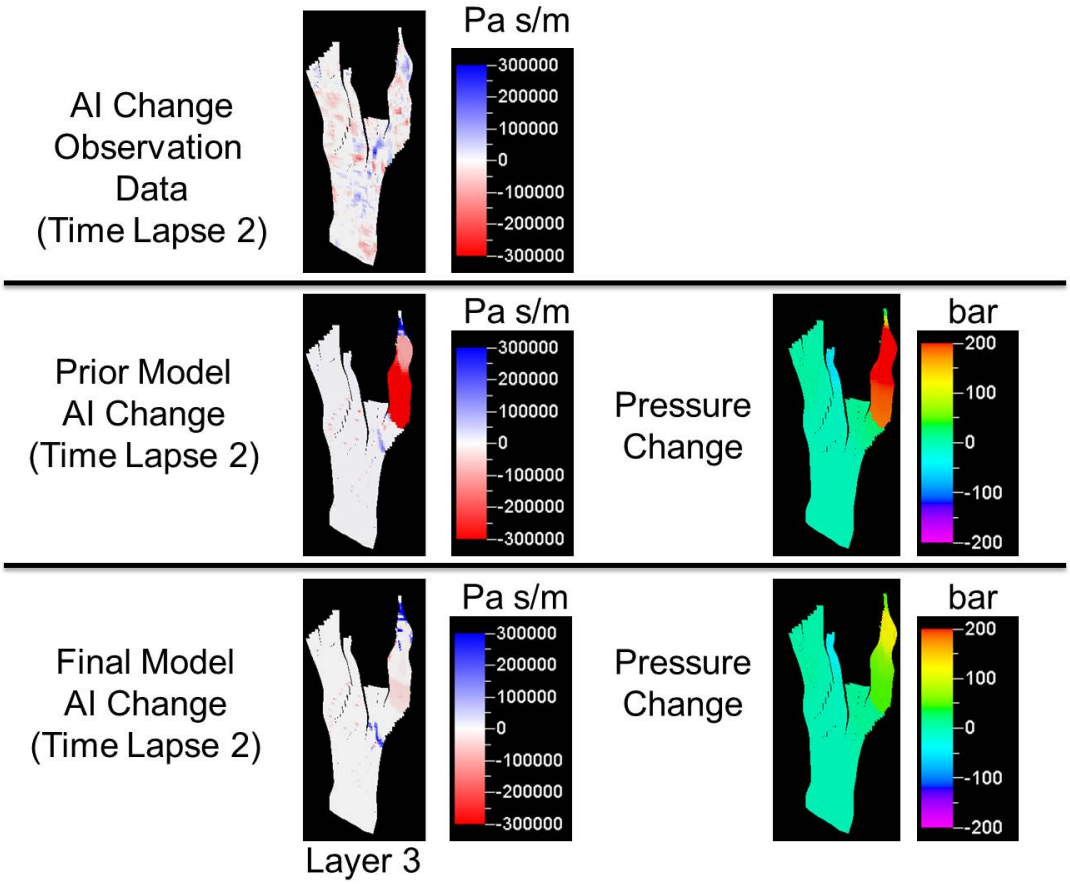

Fig. 4.14—Time-lapse acoustic impedance changes between 2003 and 2004 comparisons in selected layers among the observation data, the prior model responses and the final updated model responses and corresponding pressure change responses.

reservoir (G-segment) was corrected by the inversion. This resulted from an improved matching of the time-lapse pressure change in the final updated model as shown in **Fig.4.14**. Also for the third time-lapse period (2006-2004), there is a correspondence between the negative changes of acoustic impedance data (red color) and the gas saturation change model responses shown in **Fig.4.15**. Overall, the misfit of the time-lapse acoustic impedance change and well production response are improved substantially from the prior model.

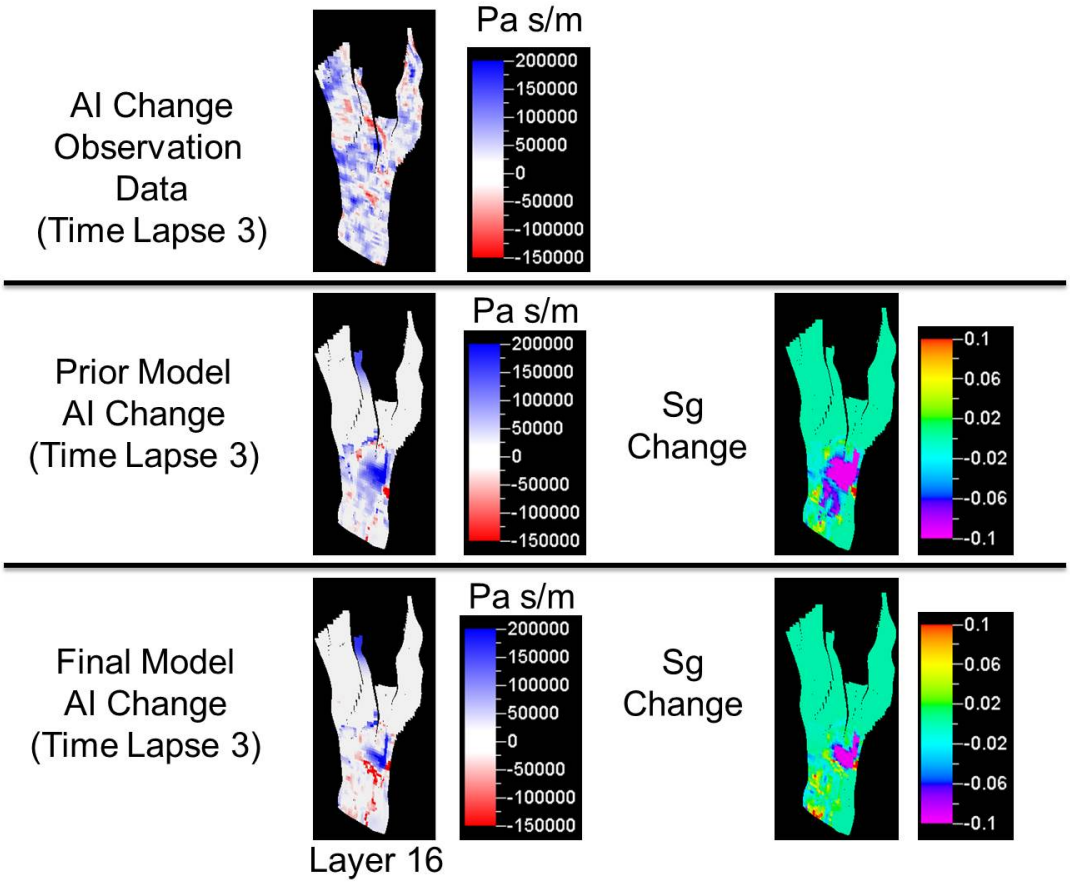

Fig. 4.15—Time-lapse acoustic impedance changes between 2004 and 2006 comparisons in selected layers among the observation data, the prior model responses and the final updated model responses and corresponding gas saturation change responses.

TABLE 4.2—ECONOMIC PARAMETERS.	
Discount rate, %/year	10
Oil price, $/bbl	75
Water production/Injection cost, $/bbl	6
Gas injection cost, $/Mscf	1.2

TABLE 4.3—PRODUCTION CONSTRAINTS.	
Max. injection BHP, bar	450
Min. production BHP, bar	150
Max. water injection rate, sm^3/day	12,000
Max. liquid production rate, sm^3/day	6,000
Max. water cut, %	95

4.3.5 Streamline-Based Rate Optimization

After the models are calibrated from the history matching process, the production and the injection rates of each well are optimized with the streamline-based rate optimization algorithm (Alhuthali et al. 2007). The reference base case for this optimization problem assumes all wells keep production/injection rates as their latest history rates at the end of history matching period from Jan. 2007 to Dec. 2016. The optimization is based on two scenarios: improving sweep efficiency to maximize oil recovery and accelerating production to maximize NPV. To account geologic uncertainty, the optimization is performed with three different calibrated models simultaneously. The economic and production constraints during the optimization are listed in **Table 4.2** and **Table 4.3** respectively.

The optimal rate strategy is developed with the objectives of (1) improving sweep efficiency by equalizing flood front arrival time at all producers and (2) production

acceleration by reducing arrival time at all producer for NPV improvement. The objective function consists of the following two (Taware et al. 2010):

$$p(\mathbf{q}) = \min \sum_{i=1}^{Nprod} \left(\bar{t}(\mathbf{q}) - t_i'(\mathbf{q})\right)^2 + \eta \sum_{i=1}^{Nprod} \left(t_i'(\mathbf{q})\right)^2. \tag{4.14}$$

The variable t_i is the calculated arrival time of producer i. The term $\bar{t}$ is an arithmetic average of all arrival time t_i from all producers. The arrival time is a function of the vector $\mathbf{q}$, which contains production/injection rates and has the dimension equal to the number of well rates, $Nprod$, to be optimized.

Minimization of the first term of Eq. (4.14) ensures that the flood front arrives nearly at the same time within the well pattern, thereby maximizing sweep efficiency. The second or acceleration term ensures that the magnitude of the arrival time is also reduced, with the effect of accelerating injection/production rates, and ensures that the optimization doesn't over-penalize highly productive wells in the attempt to improve sweep. The trade-off between equalizing arrival time and production acceleration can be controlled by the norm weight, η.

After water/gas breakthrough, the optimization is performed by incorporating the effect of unfavorable phase production into the objective function in order to reduce the allocation of production rates to wells with high water/gas production. The arrival time (t_i) is modified to include effect of unfavorable phase production as follows.

$$t_i'(\mathbf{q}) = t_i(\mathbf{q}) \times (1 - \mathrm{UF})^{0.5}, \tag{4.15}$$

and

$$\mathrm{UF} = \frac{\mathrm{ratio}_w \times \mathrm{cost}_{w,inj} \times q_{w,inj} + \mathrm{ratio}_g \times \mathrm{cost}_{g,inj} \times q_{g,inj}}{\text{gas price} \times q_{g,prd} + \text{oil price} \times q_{o,prd}}, \tag{4.16}$$

where

$$\text{ratio}_w = \frac{\text{water flux from injector}}{\text{water flux from injector+water flux from expansion}}, \tag{4.17}$$

$$\text{ratio}_g = \frac{\text{gas flux from injector}}{\text{gas flux from injector+gas flux from expansion}}. \tag{4.18}$$

Here the utility factor (UF) is the ratio of the total cost of injection to the profit from hydrocarbon production. The money from production can be calculated directly from a product of each phase production price and individual phase production rate while the money from injection is required to multiply by normalizing ratios (Eq. (4.17) and Eq. (4.18)) to separate between the flux from injected fluids and the one from the reservoir fluid expansions (e.g., aquifer and gas cap). These ratios can be acquired by individual phase streamlines tracing to identify the sources of production. From the expression in Eq. (4.15), the arrival time (t_i) is re-scaled to incorporate the defined utility factor. Before water/gas breakthrough, the utility factor is equal to zero since there is no gas and water fluxes from injectors and ratios are calculated as zero in Eq. (4.17) and Eq. (4.18). The modified arrival time (t_i') is then the same as the original arrival time. After water/gas breakthrough, the utility factor is greater than zero. Then the original arrival time (t_i) is reduced. This reduction of arrival time makes the algorithm allocate relatively smaller production to the well with high UF. In this study, the economic factors are summarized to **Table 4.2**.

To account for the geologic uncertainty, Eq. (4.14) needs to be generalized with multiple realizations. This is accomplished in terms of an expected value of the misfit values from multiple realizations penalized by its standard deviation as

$$f(\mathbf{q}) = E\Big[p(\mathbf{q})\Big] + r\sigma\Big[p(\mathbf{q})\Big], \tag{4.19}$$

and this can be derived within the decision analysis framework (Alhuthali et al. 2008). The variable r is the risk coefficient that weights the trade-off between the expected value and the standard deviation. A positive r means that the decision maker is risk averse, while a negative r means that the decision maker is risk prone. In this work, the optimization is done based on the risk neutral assumption ($r = 0$) which means the objective function is an arithmetic average from all realizations.

This optimization workflow to reduce the objective function in Eq. (4.19) is performed with five major steps as follows (**Fig. 4.16**):

1. **Running forward simulation**: run forward simulations with current rate conditions for all realizations from the current timestep to generate phase fluxes.

2. **Tracing streamlines**: use phase fluxes to trace streamlines and calculate time of flight (TOF) (Datta-Gupta and King 2007). The time of flight is utilized for computing the arrival time of the flood front to all producers.

3. **Sensitivity computation**: we compute sensitivity of arrival time to the current well rates. The calculation can be done analytically which provide significant advantages for calculation efficiency (Alhuthali et al. 2007).

4. **Stochastic objective function computation**: the model responses from multiple realizations are gathered to calculate stochastic objective function, and its gradient and Hessian.

5. **Minimization and optimal rate allocation**: Sequential Quadratic Programing (SQP) technique (Nocedal and Wright 2006) is used to minimize the objective function under operational constraints in **Table 4.3** and update the rate conditions.

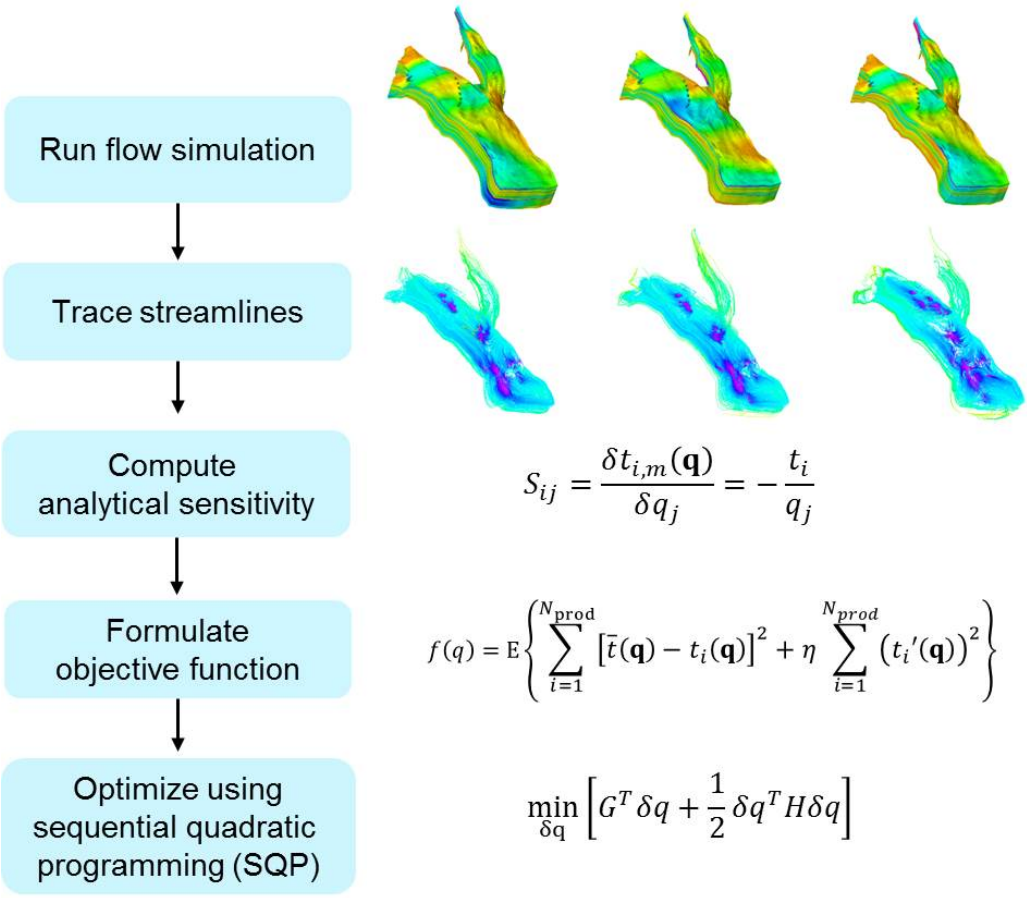

Fig. 4.16—Streamline-based rate optimization under geologic uncertainty workflow.

6. Repeat 1.-5. until the convergence criteria meet and go to the next optimization timestep.

The improvements in the recovery factor (RF) and the net present value (NPV) from rate optimization are shown in **Figs. 4.17a and 4.17b**, respectively and **Table 4.4** summarizes the optimization results. When the acceleration term is ignored ($\eta = 0$), the arrival time equalization results in the improved sweep efficiency and the increased oil recovery. In case of imposing production acceleration ($\eta = 100$), the algorithm increases more on production rates at the early time of optimization period

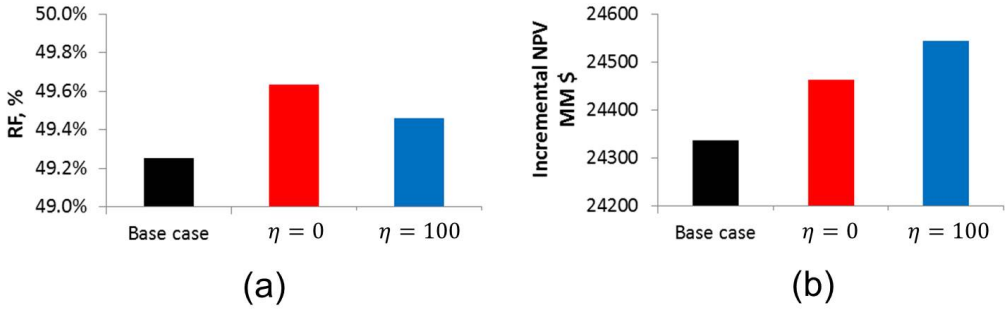

Fig. 4.17—Rate optimization results: (a) ultimate recovery factor comparisons of base case and two optimized cases: $\eta = 0$ and $\eta = 100$, (b) final NPV comparisons of base case and two optimized cases: $\eta = 0$ and $\eta = 100$.

and less emphasize on the sweep efficiency improvement. This situation provides better NPV result but with smaller ultimate oil recovery. During the early period, the case with the acceleration term ($\eta = 100$) produced more oil than the case with only maximized flood efficiency ($\eta = 0$) as shown in **Fig. 4.18b**. However, in the later time, the maximize flood efficiency case provides more oil production than the production acceleration scenario resulting in more ultimate oil recovery. In term of NPV, the production acceleration case maintained better NPV than the maximized flood efficiency case through the optimization period. Even though the ($\eta = 0$) case provides more oil production in the later time, we found that the optimization also results in higher water injection/production rates than the acceleration case which are expensive and deteriorate economic response in the later time as shown in **Fig. 4.18a**. As a comparison, the total cumulative production of oil and water and gas from each case are shown in **Fig. 4.19**.

In conclusion, this application shows the feasibility of field scale rate optimization using the streamline based algorithm under geologic uncertainty. We can maximize the sweep efficiency and/or accelerate production rate by using the norm constraint.

TABLE 4.4—RATE OPTIMIZATION RESULTS.		
	RF (%)	Incremental NPV, (MM $)
Base case	49.25%	24336
Norm = 0	49.63%	24463
Norm = 100	49.46%	24544

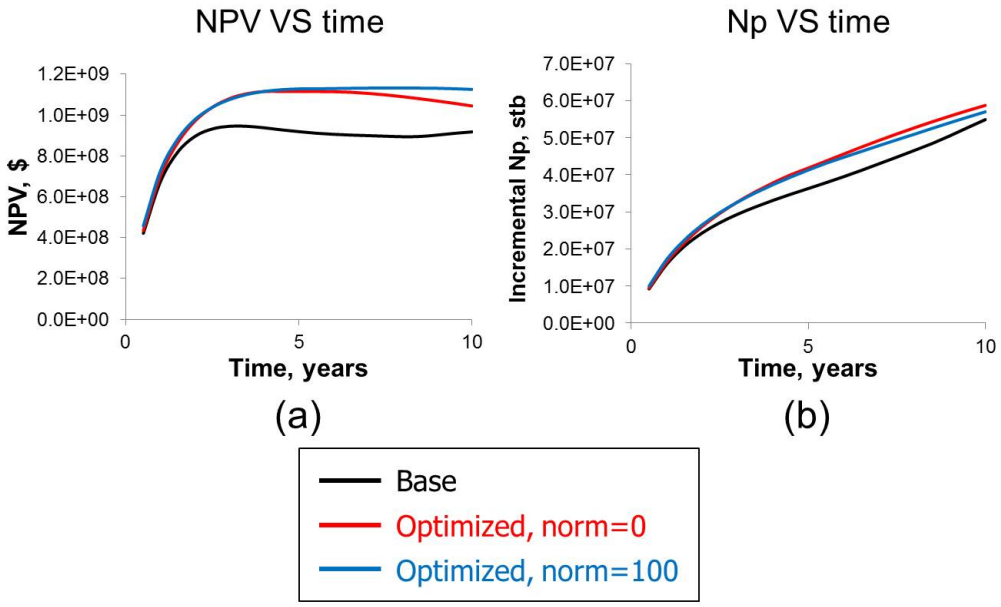

Fig. 4.18—Rate optimization results: (a) NPV comparison with respect to optimization period for base case and two optimized cases: $\eta = 0$ and $\eta = 100$, (b) Incremental oil production comparison with respect to optimization period from base case and two optimized cases: $\eta = 0$ and $\eta = 100$.

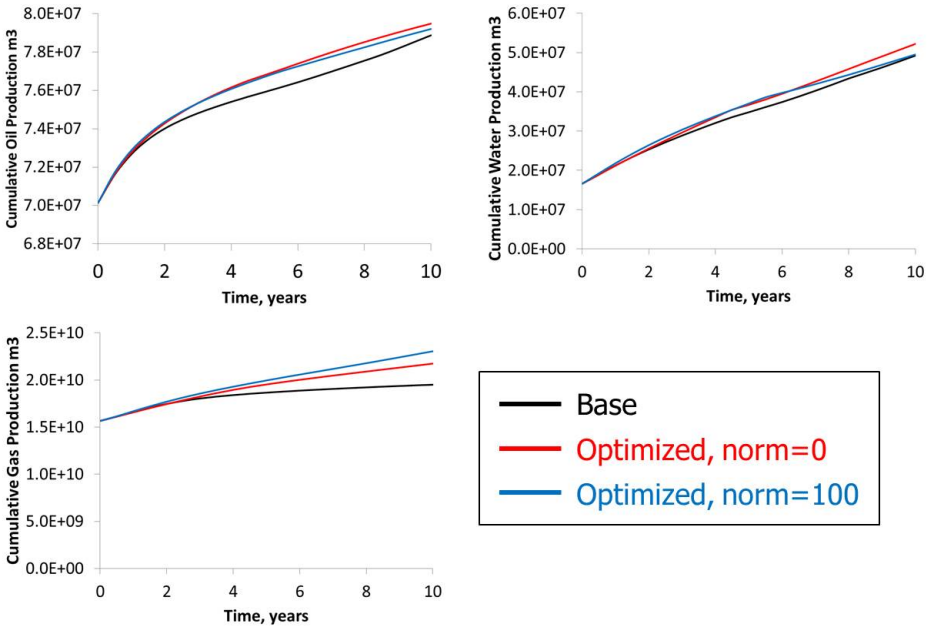

Fig. 4.19—Rate optimization results: Cumulative production rate comparison from each case.

4.4 Conclusions

The Norne field application demonstrates the practical feasibility of the structured workflow of time-lapse seismic data and production data integration using seismic data processing, petro-elastic modeling, and the efficient streamline-based data integration. The calibrated model shows the targeted global and fine scale model updates and improvement of the acoustic impedance changes between time-lapse surveys. The well by well water cut data matching also improved substantially.

For production optimization, we use the ensemble of history matched models and develop an optimal rate control strategy to maximize sweep and injection efficiency by equalizing flood front arrival times and accelerating production at all producers while accounting for geologic uncertainty. Our results show the incremental improvement of ultimate recovery factor and NPV values from calibrated model responses.

5. CONCLUSIONS AND RECOMMENDATIONS

5.1 Conclusions

This study summarized two distinct classes of inversion methods: stochastic and deterministic approaches.

For stochastic inversion method development, ensemble Kalman filter data assimilation performances were improved by the use of phase streamline based covariance localization that physically relates the underlying reservoir flow dynamics and extracts flow relevant cross correlation between model parameters and model responses. Our developed algorithm was compared to other localization method through synthetic history matching applications and outperformed those in capturing high contrast of reservoir heterogeneity in the geologic continuities that affect the flow paths between well locations.

For deterministic inversion method development, streamline-based analytic sensitivity calculations are reviewed and derived for fluid saturation and pressure drop changes with respect to reservoir parameters along streamline trajectories. The accuracy of the derived sensitivity calculation was validated with numerical experiments and the efficiency of the calculations was confirmed through field scale applications. History matching examples of time-lapse seismic derived saturation and pressure map integration showed the importance of both pressure and saturation matching to further constrain the uniqueness of parameter estimation. Norne field application demonstrated the feasibility of the proposed structured workflow to integrate both production and time-lapse seismic data into high resolution reservoir model. The hierarchical approach of global to local model calibration defines the different level of data integration.

The global step accounts for reservoir energy matching by a global adjustment of permeability using a Grid Connectivity Transform parameterization and Pareto-based multi-objective minimization. Local model calibration resolves the fine scale variation of permeability between wells through streamline derived sensitivities. The systematic combination of genetic algorithms in the global step and gradient-based inversion in the local step retain both the flexibility and the consistency of the entire workflow.

Also, through the field seismic data integration, we are able to incorporate the seismic data in the form of acoustic impedance data and relate the reservoir simulation responses of pressure and fluid saturation via petro-elastic modeling.

After the model calibration process, we utilized the ensemble of reservoir models to develop an optimal production strategy via streamline-based flow rate optimization. Our results show increased ultimate recovery and NPV values in the future predictions that can facilitate decision making process in the field development.

5.2 Recommendations

There are several recommendations that can be drawn from this study.

1. The phase streamline based covariance localization in ensemble Kalman filter needs to be applied for a real field scale model such as Norne field for the further investigation of the benefits and the limitations of the method. Relevant questions are as follows:

    - What are the good combinations of various localization methods to dynamically improve the data assimilation under changing field conditions (ex. shut-in wells, injection production well conversion etc.)?
    - How can we determine an appropriate probability threshold value to identify the common localization region intersected by phase streamlines from

all ensemble models?

- Can we extend the phase localization method to seismic data integration with EnKF using derived pressure and saturation sensitivities?

2. The streamline-based inversion methods need to be improved in several aspects. Some of the topics are as follows:

   - Rigorous comparisons of simultaneous and sequential data integration with pressure and saturation sensitivities to identify the pros and cons of both approaches such as computation expense and convergence speed and solution stability.
   - Comparisons of different objective function minimization algorithms with streamline sensitivities (e.g., LSQR, LBFGS, Gauss-Newton, PSO (particle swarm optimization))
   - Adaptive adjustment algorithm development of relative weights of norm and smoothness regularization terms in the objective function.
   - Efficient treatment of three-phase conditions (ex. data localization, data transformation (ex. frequency domain), and pressure and saturation effects separation during inversion iterations.)

3. Time-lapse seismic data integration needs a systematic comparison between time domain time delay data analysis and amplitude changes as discussed in **APPENDIX B**. The acoustic impedance responses should be modeled stochastically with uncertainty in petro-elastic model parameters rather than deterministically as treated in this study. Scale differences between reservoir grid, well log and seismic grid needs to be accounted in the proposed multiscale data integration workflow in a quantitative manner such as changing

the basis number in the global step with different data scales and/or upscaling/downscaling of streamline sensitivity calculations in the local step.

4. For optimal flow rate development, include well placement optimization using streamline flow dynamics to identify the unswept and undrained locations with time-lapse seismic signatures of bypassed oil pockets or gas preferential flow regions, pressure barriers etc.

REFERENCES

Aanonsen, S., Nævdal, G., Oliver, D., Reynolds, A., and Vallès, B. 2009. The ensemble kalman filter in reservoir engineering–a review. *SPE J.*, **14**(3):393–412.

Aki, K. and Richards, P. G. 1980. *Quantitative seismology*, volume 1424. Freeman San Francisco.

Alhuthali, A., Datta-Gupta, A., Yuen, B., and Fontanilla, J. 2008. Optimal rate control under geologic uncertainty. pages Paper SPE 113628 presented at the SPE/DOE Symposium on Improved Oil Recovery, Tulsa, Oklahoma, USA, 20–23 April.

Alhuthali, A., Oyerinde, A., and Datta-Gupta, A. 2007. Optimal waterflood management using rate control. *SPE Reservoir Evaluation & Engineering*, **10**(5):539–551.

Anderson, J. L. 2007. Exploring the need for localization in ensemble data assimilation using a hierarchical ensemble filter. *Physica D: Nonlinear Phenomena*, **230**(1):99–111.

Arenas, E., Kruijsdijk, C. V., and Oldenziel, T. 2001. Semi-automatic history matching using the pilot point method including time-lapse seismic data. pages Paper SPE71634 presented at the SPE Annual Technical Conference and Exhibition, New Orleans, Louisiana, USA, 30 September–3 October.

Arroyo-Negrete, E., Devegowda, D., Datta-Gupta, A., and Choe, J. 2008. Streamline assisted ensemble kalman filter for rapid and continuous reservoir model updating. *SPE Reservoir Evaluation & Engineering*, **11**(6):1046–1060.

Barker, J., Maarten, C., and Lars, H. 2001. Quantifying uncertainty in production forecasts: Another look at the punq-s3 problem. *SPE J.*, **6**(4):433–441.

Batycky, R., Blunt, M. J., and Thiele, M. R. 1997. A 3d field-scale streamline-based

reservoir simulator. *SPE Reservoir Engineering*, 12(4):246–254.

Behrens, R., Condon, P., Haworth, W., Bergeron, M., Wang, Z., and Ecker, C. 2002. 4d seismic monitoring of water influx at bay marchand: the practical use of 4d in an imperfect world. *SPE Reservoir Evaluation & Engineering*, **5**(5):410–420.

Behrens, R., MacLeod, M., Tran, T., and Alimi, A. 1998. Incorporating seismic attribute maps in 3d reservoir models. *SPE Reservoir Evaluation & Engineering*, **1**(2):122–126.

Bhark, E. W., Jafarpour, B., and Datta-Gupta, A. 2011. A generalized grid connectivity–based parameterization for subsurface flow model calibration. *Water Resources Research*, **47**(6).

Burkhart, T., Hoover, A. R., and Flemings, P. B. 2000. Time-lapse (4-d) seismic monitoring of primary production of turbidite reservoirs at south timbalier block 295, offshore louisiana, gulf of mexico. *Geophysics*, **65**:351.

Chen, Y. and Oliver, D. 2010a. Ensemble-based closed-loop optimization applied to brugge field. *SPE Reservoir Evaluation & Engineering*, **13**(1):56–71.

Chen, Y. and Oliver, D. S. 2010b. Cross-covariances and localization for enkf in multiphase flow data assimilation. *Computational Geosciences*, **14**(4):579–601.

Cheng, H., Datta-Gupta, A., and He, Z. 2005a. A comparison of travel time and amplitude inversion for production data integration into geologic models: Sensitivity, non-linearity and practical implications. *SPE J.*, **10**(1):75–90.

Cheng, H., Dehghani, K., and Billiter, T. 2008. A structured approach for probabilistic-assisted history matching using evolutionary algorithms: Tengiz field applications. pages Paper SPE 116212 presented at the SPE Annual Technical Conference and Exhibition, Denver, Colorado, USA, 21–24 September.

Cheng, H., Kharghoria, A., He, Z., and Datta-Gupta, A. 2005b. Fast history matching of finite-difference models using streamline-based sensitivities. *SPE Reservoir*

Evaluation & Engineering, **8**(5):426–436.

Cheng, H., Oyerinde, A., Datta-Gupta, A., and Milliken, W. 2007. Compressible streamlines and three-phase history matching. *SPE J.*, **12**(4):475–485.

Cheng, H., Wen, X., Milliken, W., and Datta-Gupta, A. 2004. Field experiences with assisted and automatic history matching using streamline models. pages Paper SPE 89857 presented at the SPE Annual Technical Conference and Exhibition, Houston, Texas, USA, 26–29 September.

Christensen, N. and Wang, H. 1985. The influence of pore pressure and confining pressure on dynamic elastic properties of berea sandstone. *Geophysics*, **50**(2):207–213.

Clifford, P., Robert, T., Parr, R., Moulds, T., Tim, C., and Allan, P. 2003. Integration of 4d seismic data into the management of oil reservoirs with horizontal wells between fluid contacts. pages Paper SPE 83956 presented at Offshore Europe, Aberdeen, United Kingdom, 2–5 September.

Dadashpour, M., Ciaurri, D. E., Mukerji, T., Kleppe, J., and Landrø, M. 2010. A derivative-free approach for the estimation of porosity and permeability using time-lapse seismic and production data. *Journal of Geophysics and Engineering*, **7**(4):351–368.

Dadashpour, M., Echeverría-Ciaurri, D., Kleppe, J., and Landrø, M. 2009. Porosity and permeability estimation by integration of production and time-lapse near and far offset seismic data. *Journal of Geophysics and Engineering*, **6**(4):325–344.

Dadashpour, M., Landrø, M., and Kleppe, J. 2008. Nonlinear inversion for estimating reservoir parameters from time-lapse seismic data. *Journal of Geophysics and Engineering*, **5**(1):54–66.

Datta-Gupta, A. and King, M. J. 1995. A semianalytic approach to tracer flow modeling in heterogeneous permeable media. *Advances in Water Resources*, **18**(1):9–24.

Datta-Gupta, A. and King, M. J. 2007. *Streamline simulation: Theory and practice*, volume **11**. Society of Petroleum Engineers, Richardson, TX.

Datta-Gupta, A., Kulkarni, K. N., Yoon, S., and Vasco, D. 2001. Streamlines, ray tracing and production tomography: Generalization to compressible flow. *Petroleum Geoscience*, **7**:S75–S86.

Datta-Gupta, A., Yoon, S., Barman, I., and Vasco, D. 1998. Streamline-based production data integration. *Journal of Petroleum Technology*, **50**(12):72–76.

Deutsch, C. V. and Journel, A. G. 1992. *Geostatistical software library and user's guide*, volume 1996. Oxford university press New York.

Devegowda, D., Arroyo-Negrete, E., and Datta-Gupta, A. 2010. Flow relevant covariance localization during dynamic data assimilation using enkf. *Advances in Water Resources*, **33**(2):129–145.

Domenico, S. 1976. Effect of brine-gas mixture on velocity in an unconsolidated sand reservoir. *Geophysics*, **41**(5):882–894.

Dong, Y. and Oliver, D. 2005. Quantitative use of 4d seismic data for reservoir description. *SPE J.*, **10**(1):91–99.

Doyen, P., Psaila, D., and Jans, D. 1997. Reconciling data at seismic and well log scales in 3-d earth modelling. pages Paper SPE 38698 presented at the SPE Annual Technical Conference and Exhibition, San Antonio, Texas, USA, 5–8 October.

Eastwood, J., Lebel, P., Dilay, A., and Blakeslee, S. 1994. Seismic monitoring of steam-based recovery of bitumen. *The Leading Edge*, **13**(4):242–251.

Emerick, A. and Reynolds, A. 2011. Combining sensitivities and prior information for covariance localization in the ensemble kalman filter for petroleum reservoir applications. *Computational Geosciences*, **15**(2):251–269.

Evensen, G. 1994. Sequential data assimilation with a nonlinear quasi-geostrophic model using monte carlo methods to forecast error statistics. *Journal of Geophys-*

ical Research: Oceans (1978–2012), **99**(C5):10143–10162.

Evensen, G. 2003. The ensemble kalman filter: Theoretical formulation and practical implementation. *Ocean Dynamics*, **53**(4):343–367.

Evensen, G. 2006. *Data Assimilation: The Ensemble Kalman Filter*. Springer-Verlag New York, Inc.

Fahimuddin, A., Aanonsen, S., and Skjervheim, J.-A. 2010. 4d seismic history matching of a real field case with enkf: use of local analysis for model updating. pages Paper SPE 134894 presented at the SPE Annual Technical Conference and Exhibition, Florence, Italy, 19–22 September.

Falcone, G., Gosselin, O., Maire, F., Marrauld, J., and Zhakupov, M. 2004. Petroelastic modelling as key element of 4d history matching: a field example. pages Paper SPE 90466 presented at the SPE Annual Technical Conference and Exhibition, Houston, Texas, USA, 26–29 September.

Fanchi, J. R. 2001. Time-lapse seismic monitoring in reservoir management. *The Leading Edge*, **20**(10):1140–1147.

Feng, T. and Mannseth, T. 2010. Impact of time-lapse seismic data for permeability estimation. *Computational Geosciences*, **14**(4):705–719.

Floris, F., Bush, M., Cuypers, M., Roggero, F., and Syversveen, A. R. 2001. Methods for quantifying the uncertainty of production forecasts: a comparative study. *Petroleum Geoscience*, **7**(S):S87–S96.

Foster, D. 2007. The bp 4-d story: Experience over the last 10 years and current trends. pages Paper IPTC 11757 presented at International Petroleum Technology Conference, Dubai, U.A.E., 4–6 December.

Gaspari, G. and Cohn, S. E. 1999. Construction of correlation functions in two and three dimensions. *Quarterly Journal of the Royal Meteorological Society*, **125**(554):723–757.

Gassmann, F. 1951. Elastic waves through a packing of spheres. *Geophysics*, **16**(4):673–685.

Gosselin, O., Aanonsen, S., Aavatsmark, I., Cominelli, A., Gonard, R., Kolasinski, M., Ferdinandi, F., Kovacic, L., and Neylon, K. 2003. History matching using time-lapse seismic (huts). pages Paper SPE 84464 presented at the SPE Annual Technical Conference and Exhibition, Denver, Colorado, USA, 5–8 October.

Gosselin, O., van den Berg, S., and Cominelli, A. 2001. Integrated history-matching of production and 4d seismic data. pages Paper SPE 71599 presented at the SPE Annual Technical Conference and Exhibition, New Orleans, Louisiana, USA, 30 September–3 October.

Gu, Y. and Oliver, D. 2007. An iterative ensemble kalman filter for multiphase fluid flow data assimilation. *SPE J.*, **12**(4):438–446.

Hamill, T. M., Whitaker, J. S., and Snyder, C. 2001. Distance-dependent filtering of background error covariance estimates in an ensemble kalman filter. *Monthly Weather Review*, **129**(11):2776–2790.

Harris, J. M., Langan, R. T., Fasnacht, T. M., Melton, D. M., Smith, B. M., Sinton, J. M., and Tan, H. M. 1996. Experimental verification of seismic monitoring of co2 injection in carbonate reservoirs. pages Expanded Abstracts presented at the SEG Annual Meeting, Denver, Colorado, USA, November 10 – 15.

Hatton, L., Worthington, M. H., and Makin, J. 1986. Seismic data processing: theory and practice. Technical report, Merlin Profiles Ltd.

He, Z., Datta-Gupta, A., and Vasco, D. 2006. Rapid inverse modeling of pressure interference tests using trajectory-based traveltime and amplitude sensitivities. *Water Resources Research*, **42**(3).

He, Z., Yoon, S., and Datta-Gupta, A. 2002. Streamline-based production data integration with gravity and changing field conditions. *SPE J.*, **7**(4):423–436.

Hohl, D., Jimenez, E., and Datta-Gupta, A. 2006. Field experiences with history matching an offshore turbiditic reservoir using inverse modeling. pages Paper SPE 101983 presented at the SPE Annual Technical Conference and Exhibition, San Antonio, Texas, USA, 24–27 September.

Houtekamer, P. L. and Mitchell, H. L. 1998. Data assimilation using an ensemble kalman filter technique. *Monthly Weather Review*, **126**(3):796–811.

Houtekamer, P. L. and Mitchell, H. L. 2001. A sequential ensemble kalman filter for atmospheric data assimilation. *Monthly Weather Review*, **129**(1):123–137.

Huang, X., Meister, L., and Workman, R. 1997. Reservoir characterization by integration of time-lapse seismic and production data. pages Paper SPE 38695 presented at the SPE Annual Technical Conference and Exhibition, San Antonio, Texas, USA, 5–8 October.

Ikelle, L. and Amundsen, L. 2005. *Introduction to petroleum seismology*. Society of Exploration Geophysicists Tulsa, OK.

Jafarpour, B. and McLaughlin, D. 2009. Reservoir characterization with the discrete cosine transform. *SPE J.*, **14**(1):182–201.

Jenkins, S., Waite, M., and Bee, M. 1997. Time-lapse monitoring of the duri steamflood: A pilot and case study. *The Leading Edge*, **16**(9):1267–1274.

Jimenez, E., Sabir, K., Datta-Gupta, A., and King, M. J. 2007. Spatial error and convergence in streamline simulation. *SPE Reservoir Evaluation & Engineering*, **10**(3):221–232.

Kennett, B. 1983. *Seismic wave propagation in stratified media*. Cambridge University Press, Canberra ACT 0200, Australia.

Kumar, S., Datta-Gupta, A., and Jimenez, E. 2009. Understanding reservoir mechanisms using phase and component streamline tracing and visualization. pages Paper SPE 124252 presented at the SPE Annual Technical Conference and Exhi-

bition, New Orleans, Louisiana, USA, 4–7 October.

Landa, J. and Horne, R. 1997. A procedure to integrate well test data, reservoir performance history and 4-d seismic information into a reservoir description. pages Paper SPE38653 presented at the SPE Annual Technical Conference and Exhibition, San Antonio, Texas, USA, 5–8 October.

Landrø, M., Digranes, P., and Strønen, L. 2001. Mapping reservoir pressure and saturation changes using seismic methods: possibilities and limitations. *First Break*, **19**(12):671–677.

Landro, M., Solheim, O. A., Hilde, E., Ekren, B. O., and Stronen, L. K. 1999. The gullfaks 4d seismic study. *Petroleum Geoscience*, **5**(3):213–226.

Li, G. and Reynolds, A. 2009. Iterative ensemble kalman filters for data assimilation. *SPE J.*, **14**(3):496–505.

Lumley, D. and Behrens, R. 1998. Practical issues of 4d seismic reservoir monitoring: What an engineer needs to know. *SPE Reservoir Evaluation & Engineering*, **1**(6):528–538.

Lumley, D. E. 2001. Time-lapse seismic reservoir monitoring. *Geophysics*, **66**(1):50–53.

Lumley, D. E., Behrens, R. A., and Wang, Z. 1997. Assessing the technical risk of a 4-d seismic project. *The Leading Edge*, **16**(9):1287–1292.

Luo, Y. and Schuster, G. T. 1991. Wave-equation traveltime inversion. *Geophysics*, **56**(5):645–653.

Mavko, G., Mukerji, T., and Dvorkin, J. 1998. *The Rock Physics Handbook: Tools for Seismic Analysis in Porous Media, 329 pp.* Cambridge Univ. Press, Cambridge, UK.

Mindlin, R. D. 1949. Compliance of elastic bodies in contact. *Journal of Applied Mechanics*, **16**:259–268.

Nocedal, J. and Wright, S. J. 2006. *Numerical optimization*. Springer, New York.

Nur, A. 1989. Four-dimesional seismology and (true) direct detection of hydrocarbons: The petrophysical basis. *The Leading Edge*, **8**(9):30–36.

Nur, A., Tosaya, C., and Vo-Thanh, D. 1984. Seismic monitoring of thermal enhanced oil recovery processes. pages Expanded Abstracts presented at the SEG Annual Meeting, Atlanta, Georgia, December 2 – 6.

Nævdal, G., Johnsen, L., Aanonsen, S., and Vefring, E. 2005. Reservoir monitoring and continuous model updating using ensemble kalman filter. *SPE J.*, **10**(1):66–74.

O'Donovan, A., Smith, S., and Pal, K. 2000. Foinaven 4d seismic-dynamic reservoir parameters and reservoir management. pages Paper SPE 63294 presented at the SPE Annual Technical Conference and Exhibition, Dallas, Texas, USA, 1–4 October.

Osdal, B., Husby, O., Aronsen, H. A., Chen, N., and Alsos, T. 2006. Mapping the fluid front and pressure buildup using 4d data on norne field. *The Leading Edge*, **25**(9):1134–1141.

Oyerinde, A., Datta-Gupta, A., and Milliken, W. 2009. Experiences with streamline-based three-phase history matching. *SPE Reservoir Evaluation & Engineering*, **12**(4):528–541.

Paige, C. C. and Saunders, M. A. 1982. Lsqr: An algorithm for sparse linear equations and sparse least squares. *ACM Transactions on Mathematical Software (TOMS)*, **8**(1):43–71.

Park, H.-Y., Datta-Gupta, A., and King, M. 2013. Handling conflicting multiple objectives using pareto-based evolutionary algorithm for history matching of reservoir performance. pages Paper SPE 163623 presented at the SPE Reservoir Simulation Symposium, The Woodlands, Texas, USA, 18–20 February.

Peters, L., Arts, R., Brouwer, G., Geel, C., Cullick, S., Lorentzen, R., Chen, Y.,

Dunlop, N., Vossepoel, F., and Xu, R. 2010. Results of the brugge benchmark study for flooding optimization and history matching. *SPE Reservoir Evaluation & Engineering*, **13**(3):391–405.

Pullin, N., Matthews, L., and Hirsche, K. 1987. Techniques applied to obtain very high resolution 3-d seismic imaging at an athabasca tar sands thermal pilot. *The Leading Edge*, **6**(12):10–15.

Reuss, A. 1929. Berechnung der fließgrenze von mischkristallen auf grund der plastizitätsbedingung für einkristalle. *ZAMM-Journal of Applied Mathematics and Mechanics/Zeitschrift für Angewandte Mathematik und Mechanik*, **9**(1):49–58.

Rey, A., Bhark, E., Gao, K., Datta-Gupta, A., and Gibson, R. 2012. Streamline-based integration of time-lapse seismic and production data into petroleum reservoir models. *Geophysics*, **77**(6):M73–M87.

Rey, A., Datta-Gupta, A., and Ballin, P. 2011. Assisted history matching in the presence of frequent well intervention using generalize travel time inversion. *Journal of Petroleum Science and Engineering*, **78**(2):415–430.

Rwechungura, R., Bhark, E., Miljeteig, O., Suman, A., Kourounis, D., Foss, B., Hoier, L., and Kleppe, J. 2012. Results of the first norne field case on history matching and recovery optimization using production and 4d seismic data. pages Paper SPE 157112 presented at the SPE Annual Technical Conference and Exhibition, San Antonio, Texas, USA, 8–10 October.

Sarma, P. and Chen, W. 2009. Generalization of the ensemble kalman filter using kernels for nongaussian random fields. pages Paper SPE 119177 presented at the SPE Reservoir Simulation Symposium, The Woodlands, Texas, USA, 2–4 February.

Seiler, A., Evensen, G., Skjervheim, J.-A., Hove, J., and Vabø, J. G. 2009. Advanced reservoir management workflow using an enkf based assisted history matching method. pages Paper SPE 118906 presented at the SPE Reservoir Simulation

Symposium, The Woodlands, Texas, USA, 2–4 February. SPE Reservoir Simulation Symposium, 2-4 February 2009, The Woodlands, Texas, USA.

Skjervheim, J.-A., Evensen, G., Aanonsen, S., Ruud, B. O., and Johansen, T.-A. 2007a. Incorporating 4d seismic data in reservoir simulation models using ensemble kalman filter. *SPE J.*, **12**(3):282–292.

Skjervheim, J.-A., Evensen, G., Aanonsen, S., Ruud, B. O., and Johansen, T.-A. 2007b. Incorporating 4d seismic data in reservoir simulation models using ensemble kalman filter. *SPE J.*, **12**(3):282–292.

Steffensen, I. and Karstadt, P. 1996. Norne field development-fast track from discovery to production. *Journal of Petroleum Technology*, **48**(4):296–299, 339.

Stovas, A. and Arntsen, B. 2006. Vertical propagation of low-frequency waves in finely layered media. *Geophysics*, **71**(3):87–94.

Taware, S., Sharma, M., Alhuthali, A. H., and Datta-Gupta, A. 2010. Optimal water flood management under geological uncertainty using accelerated production strategy. pages Paper SPE 133882 presented at the SPE Annual Technical Conference and Exhibition, Florence, Italy 19–22 September.

Toinet, S. 2004. 4d feasibility and calibration using 3d seismic modeling of reservoir models. pages Paper SPE 88783 presented at Abu Dhabi International Conference and Exhibition, Abu Dhabi, United Arab Emirates,10–13 October.

Tura, A. and Lumley, D. 2000. Estimating pressure and saturation changes from time-lapse avo data. pages Paper OTC 12130 presented at Offshore Technology Conference, Houston, Texas, USA, 1–4 May.

Vasco, D. and Datta-Gupta, A. 1999. Asymptotic solutions for solute transport: A formalism for tracer tomography. *Water Resources Research*, **35**(1):1–16.

Vasco, D. and Karasaki, K. 2006. Interpretation and inversion of low-frequency head observations. *Water Resources Research*, **42**(5).

Vasco, D., Yoon, S., and Datta-Gupta, A. 1999. Integrating dynamic data into high-resolution reservoir models using streamline-based analytic sensitivity coefficients. *SPE J.*, **4**(4):389–399.

Vasco, D. W., Datta-Gupta, A., Behrens, R., Condon, P., and Rickett, J. 2004. Seismic imaging of reservoir flow properties: Time-lapse amplitude changes. *Geophysics*, **69**(6):1425–1442.

Veeken, P. C., Priezzhev, I. I., Shmaryan, L. E., Shteyn, Y. I., Barkov, A. Y., and Ampilov, Y. P. 2009. Nonlinear multitrace genetic inversion applied on seismic data across the shtokman field, offshore northern russia. *Geophysics*, **74**(6):WCD49–WCD59.

Wang, Z., Hirsche, W. K., and Sedgwick, G. 1991. Seismic monitoring of water floods?-a petrophysical study. *Geophysics*, **56**(10):1614–1623.

Wang, Z. and Nur, A. 1988. Effect of temperature on wave velocities in sands and sandstones with heavy hydrocarbons. *SPE Reservoir Engineering*, **3**(1):158–164.

Watanabe, S., Datta-Gupta, A., Efendiev, Y., and Devegowda, D. 2009. A hybrid ensemble kalman filter with coarse scale constraint for nonlinear dynamics. pages Paper SPE 124826 presented at the SPE Annual Technical Conference and Exhibition. New Orleans, Louisiana, USA, 4–7 October.

Williams, M., Keating, J., and Barghouty, M. 1998. The stratigraphic method: a structured approach to history matching complex simulation models. *SPE Reservoir Evaluation & Engineering*, **1**(2):169–176.

Wu, Z. and Datta-Gupta, A. 2002. Rapid history matching using a generalized travel time inversion method. *SPE J.*, **7**(2):113–122.

Yin, J., Park, H.-Y., Datta-Gupta, A., King, M. J., and Choudhary, M. K. 2011. A hierarchical streamline-assisted history matching approach with global and local parameter updates. *Journal of Petroleum Science and Engineering*, **80**(1):116–130.

APPENDIX A

WATER SATURATION CHANGE SENSITIVITY

In the water saturation sensitivity derivation, we assumed that the streamline trajectory is fixed from the initial condition to the particular time of interest for calculating the sensitivity. Also, we used the self-similar solution to estimate partial derivatives in Eq.(3.21) and Eq. (3.22), which assumes uniform initial conditions. In order to generalize the formulation to account for changing field conditions, we separate the total time t into small timestep sizes as

$$t = \sum_{i=1}^{N} \Delta t_i \tag{A.1}$$

and the total change in the arrival time as the weighted average of arrival time change for each timestep as follows

$$\delta t = \sum_{i=1}^{N} \frac{\Delta t_i}{t} \delta t_i. \tag{A.2}$$

Then, the arrival time sensitivity becomes

$$\begin{aligned}
\left.\frac{\delta t}{\delta k}\right|_{\tau_0} &= \sum_{i=1}^{N} \left[\frac{\Delta t_i}{t} \left.\frac{\delta t_i}{\delta k}\right|_{\tau_0,t_i} \right] \\
&= \sum_{i=1}^{N} \left[\frac{\Delta t_i}{t} \left.\frac{\partial t_i}{\partial \tau}\right|_{\tau_0,t_i} \left.\frac{\delta \tau}{\delta k}\right|_{\tau_0,t_i} \right] \\
&= \sum_{i=1}^{N} \left[\frac{\Delta t_i}{t} \frac{t}{\tau_{0,i}} \left.\frac{\delta \tau}{\delta k}\right|_{\tau_0,t_i} \right] \\
&= \sum_{i=1}^{N} \left[\frac{\Delta t_i}{\tau_{0,i}} \left.\frac{\delta \tau}{\delta k}\right|_{\tau_0,t_i} \right]
\end{aligned} \tag{A.3}$$

Substituting Eq. (A.3) into Eq. (3.26), we obtain the generalized form of saturation sensitivity at grid block location $\mathbf{x}$ as

$$\begin{aligned}\frac{\delta S_w(\boldsymbol{\tau}_0,t)}{\delta k(\mathbf{x})} &= \frac{\partial S_w(\boldsymbol{\tau}_0,t)}{\partial t}\cdot\sum_{i=1}^{N}\left[\frac{\Delta t_i}{t}\frac{\delta t_i}{\delta k(\mathbf{x})}\bigg|_{\boldsymbol{\tau}_0,t_i}\right] \\ &\approx \frac{S_w(\boldsymbol{\tau},t)-S_w(\boldsymbol{\tau},t-\Delta t)}{\Delta t}\sum_{i=1}^{N}\left[-\frac{\Delta t_i}{\tau_{0,i}}\frac{\delta \boldsymbol{\tau}}{\delta k(\mathbf{x})}\bigg|_{\boldsymbol{\tau}_0,t_i}\right]. \end{aligned} \tag{A.4}$$

To account for the changing field conditions, the streamlines are traced for every time interval Δt_i and the saturation sensitivity in Eq. (A.4) is computed by integrating the sensitivity values for the entire time interval. Also, if the streamlines do not change, Eq.(A.4) reverts back to Eq. (3.26). Now the saturation change sensitivity can be computed by calculating the saturation sensitivities at two different times $(t=t_1, t=t_2, t_1<t_2)$ as follows

$$\begin{aligned}\frac{\delta \Delta S_w(\boldsymbol{\tau}_0)}{\delta k(\mathbf{x})}\bigg|_{t_1}^{t_2} &= \frac{\delta S_w(\boldsymbol{\tau}_0,t_2)}{\delta k(\mathbf{x})}-\frac{\delta S_w(\boldsymbol{\tau}_0,t_1)}{\delta k(\mathbf{x})} \\ &= \frac{\partial S_w(\boldsymbol{\tau}_0,t_2)}{\partial t}\sum_{i=1}^{N_2}\left[-\frac{\Delta t_i}{\tau_{0,i}}\frac{\delta \boldsymbol{\tau}}{\delta k(\mathbf{x})}\bigg|_{\boldsymbol{\tau}_0,t_i}\right]-\frac{\partial S_w(\boldsymbol{\tau}_0,t_1)}{\partial t}\sum_{i=1}^{N_1}\left[-\frac{\Delta t_i}{\tau_{0,i}}\frac{\delta \boldsymbol{\tau}}{\delta k(\mathbf{x})}\bigg|_{\boldsymbol{\tau}_0,t_i}\right] \end{aligned} \tag{A.5}$$

where the saturation time partial derivatives can be approximated by a backward differencing from the simulation responses as in Eq. (A.4).

APPENDIX B

TIME-LAPSE SEISMIC DATA ANALYSIS*

Seismic surveys acquired at different stages in the life of an oil or gas reservoir can provide time-lapse snapshots of the fluid distribution over production time. This technique, called four-dimensional (4D) seismic reservoir monitoring, is helping the E&P industry delineate bypassed hydrocarbons and optimize recovery. Our objective here is to show that the difference between the two surveys acquired at different stages in the life of an oil or gas reservoir can be analyzed and characterized using the second- and third-order correlations.

To facilitate our discussion here, let us consider the geophysical model in **Fig. B.1a**. The response to this model is given in **Fig. B.2a**. We consider this response to correspond to the baseline survey (or reference survey). **Fig. B.1b** shows the same geophysical model after a couple of months. The data corresponding to the monitoring survey are given in **Fig. B.2b**. We can see that the two datasets are quite similar, yet there are differences between the two surveys, as we can see in **Fig. B.2c**. In real cases, the differences between surveys are often affected by changes in the acquisition systems between the two surveys and by the difficulties involved in duplicating the geographical positions of sources and receiver positions and environmental conditions from one survey to another. **Fig. B.3** shows that these errors can color the differences between surveys and lead to erroneous analysis.

*Part of this section is reprinted with permission from the preparation of the second edition of "Introduction to Petroleum Seismology" by Ikelle, L.T., Amundsen, L, 2005., Society of Exploration Geophysicists Tulsa, OK.

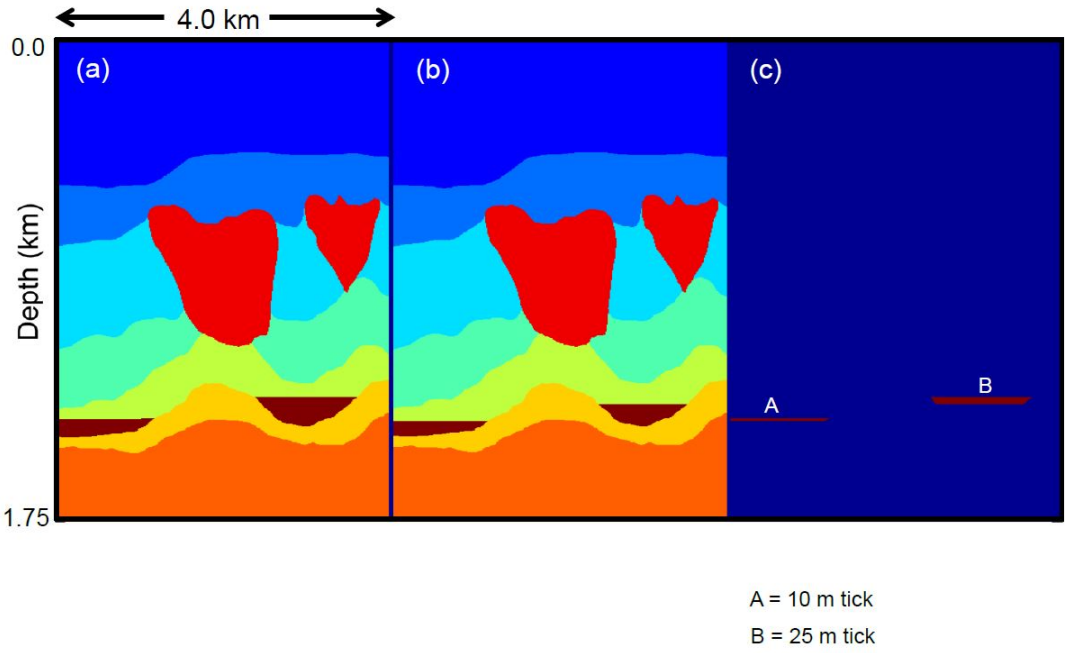

Fig. B.1—Geophysical models: (a) at baseline survey time, (b) at monitoring survey time, (c) differences between two survey times.

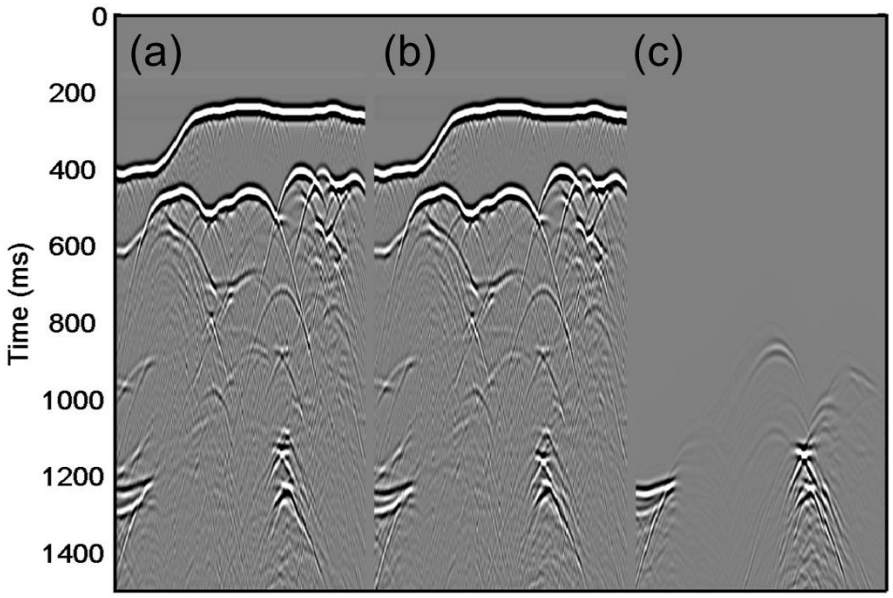

Fig. B.2—Geophysical model responses: (a) baseline survey, (b) monitoring survey and (c) differences between two surveys.

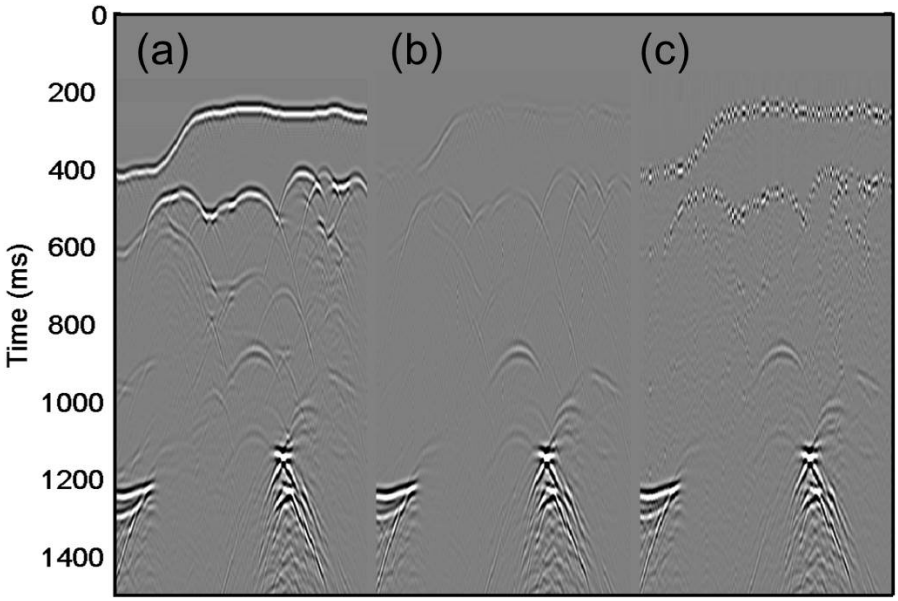

Fig. B.3—Geophysical model responses of differences between two surveys affected by different errors in the receiver positions: (a), (b), and (c).

B.1 Correlation

In addition to computing the differences between the two surveys, one can also analyze the similarities between surveys. The coherence correlation allows us to measure the similarities between signals. Because of the characteristics of coherence correlation, it is useful to separate the analysis of the traveltime from that of amplitude similarities.

One way of measuring traveltime differences between the baseline survey and the monitoring survey is to estimate the time delays between the two fields. At each point (x, t) of the data, we can obtain this time delay by computing the coherence correlation between the baseline survey and the monitoring survey for a small portion of data, made of J time samples and I traces, around the point (x, t). The time lag corresponding to the maximum value of the coherence correlation provides the desired

time delay. For the cases in which the crosscorrelation is too small for an accurate calculation of the coherence correlation, because the data are almost zero, the time delay is set to zero. **Fig. B.4** shows the time delay between the baseline survey and the monitoring surveys. We have used the data of the monitoring surveys with the errors in the receiver positions described in **Fig. B.3**. The window used for our computations of the coherence correlation, and subsequently for the computation of time delays between the two fields, was 20 ms $\times$ 9 traces around each point (x, t) of data. We can see that the time delays between the baseline survey and the monitoring survey, which are due to the changes in the geophysical model, are clearly detected by the coherence correlation.

Notice that time differences between the baseline survey and the monitoring surveys, which are due to variations in acquisition systems between the two surveys, are smoothed over by the crosscorrelation and therefore almost undetectable by this approach. In other words, by using the difference in Fig. B.3 and the time delays in Fig. B.4, we can separate the regions of the data in Fig. B.3 related to data acquisition errors from the regions associated with changes in the physical model.

One way of measuring amplitude differences between the baseline survey and the monitoring survey is to compute the correlation energy between these two surveys. This energy can be obtained from the coherence correlation used in the computation of the time delay in Fig. B.4. **Fig. B.5** shows the correlation energy between the baseline survey and the monitoring surveys. Again, we have used the data of the monitoring surveys with the errors in the receiver positions described in Fig. B.3. The window used for the computation of time delays between the baseline survey and the monitoring survey is the same as in Fig. B.4. Notice that the range of variation of the correlation energy between the surveys is about 5 dB.

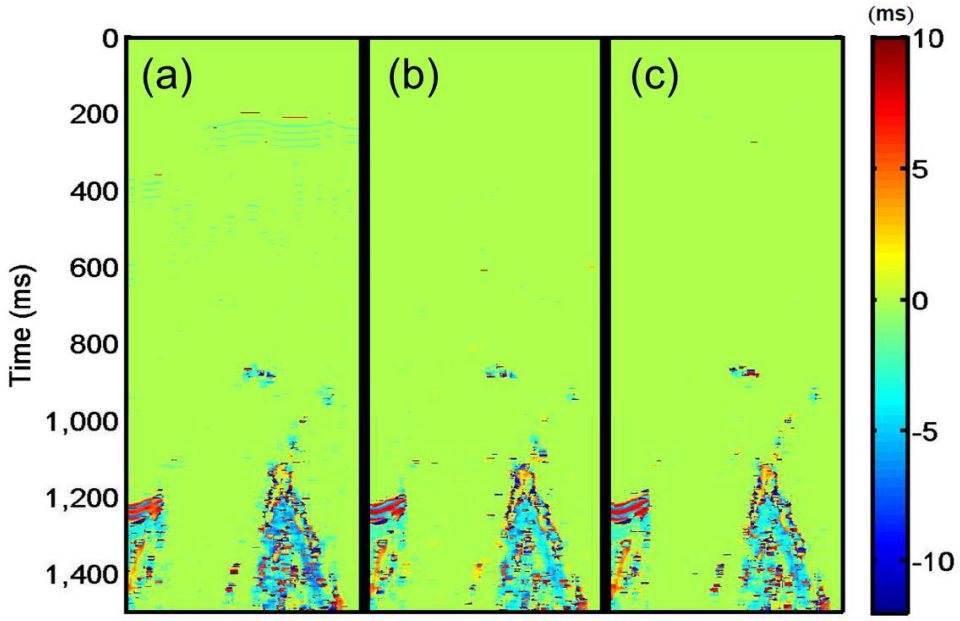

Fig. B.4—Time delay between the baseline survey and the monitoring surveys affected by different errors in the receiver positions: (a), (b), and (c).

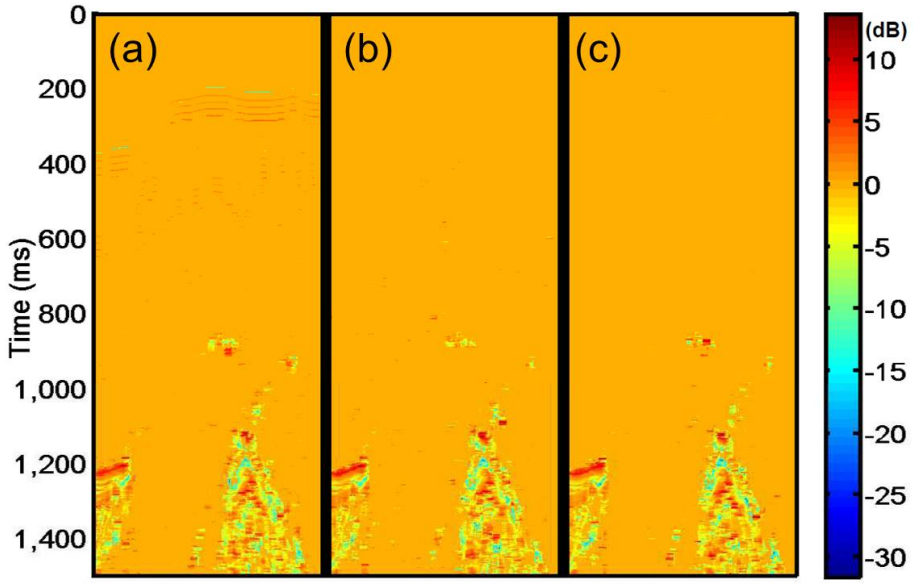

Fig. B.5—The correlation energy between the baseline survey and the monitoring surveys affected by different errors in the receiver positions: (a), (b), and (c).

B.2 Phase Extension

Seismic data are today uniformly sampled in time at 2 ms- or 4 ms-intervals. However, the time delays between the baseline and monitoring surveys are not necessarily integer multiples of these sampling periods. Moreover, they can be even smaller than 2 ms. So the question is how we can estimate time delays which are not integer multiples of the sampling period or smaller than the sampling periods.

One approach is to use the fact that the data are not aliased in time. Therefore we can interpolate the data using the following formula:

$$x_c(t) = \Delta t \sum_{n=-\infty}^{+\infty} x(n) \frac{\sin 2\pi f_N (t - n\Delta t)}{\pi (t - n\Delta t)}, \tag{B.1}$$

where $x_c(t)$ is the continuous signal and $x(n)$ is the discrete signal, Δt is the time interval, and $f_N = 1/2\Delta t$. We can then use the interpolated data for more-precise time-delay estimation.

B.3 The Signal-To-Noise Ratio

The signal-to-noise ratio is a particularly abused concept, not only in petroleum seismology but in other disciplines, too. It is an attempt to compare the "size" of a signal embedded in noise with the size of that noise. The problem is that there is no unique definition for a signal-to-noise ratio. Here are the two definitions generally cited in petroleum seismology literature (e.g., Hatton et al. 1986):

$$\mathcal{R} = \frac{\text{RMS of the signal}}{\text{RMS of the noise}} \tag{B.2}$$

and

$$\mathcal{R} = \frac{\text{average absolute amplitude of the signal}}{\text{average absolute amplitude of the noise}}. \tag{B.3}$$

These two ratios can differ markedly, depending on the spectrum and distribution of the noise.

The practical problem associated with the definitions in Eq. (B.2) and Eq. (B.3) is that they assume that for their computation, the signal and the noise can be separated, whereas the seismic trace contains a signal plus noise. Fortunately, we can show that, under reasonable assumptions, signal-to-noise ratios can be related to correlation functions.

Assume that there are at least M seismic traces which contain the same source signature, perhaps with some relative time shifts and different realizations of additive noise. The general composite trace, which is the time reflection signal plus noise, can be written

$$u(t,k) = a(k)w(t-\tau_k) + n(t,k), \quad k = 1, ..., M, \tag{B.4}$$

where $w(t)$ is the (noise-free) time-reflection signal, τ_k is the time shift on trace k, $a(k)$ is the weight of the time reflection signal on trace k, and $n(t,k)$ is the additive noise on trace k.

For the case in which the noise is zero-mean and uncorrelated with the signal, we have the following properties:

$$\mathrm{E}[u(t,k)n(t+\tau,l)] = 0, \qquad k \neq l, \tag{B.5}$$

$$\mathrm{E}[a(k)w(t)n(t+\tau,l)] = 0, \quad \text{for all } k \text{ and } l. \tag{B.6}$$

Also we define the continuous-time crosscorrelation of traces $u(t,k)$ and $u(t,l)$ as a function of lag, τ, as

$$r_{u_k,u_l}(\tau) = \mathrm{E}[u(t,k)n(t+\tau,l)]. \tag{B.7}$$

Then, using Eq. (B.4), Eq. (B.5), and Eq. (B.6), we arrive at

$$\begin{aligned} r_{u_k,u_l}(\tau) &= a(k)a(l)\,\mathrm{E}[w(t-\tau_k)w(t-\tau_l+\tau)] \\ &= a(k)a(l)r_{w,w}[\tau-(\tau_l-\tau_k)], \end{aligned} \tag{B.8}$$

where $r_(w,w)(\tau)$ is the autocorrelation function of the time reflection signal, w, at τ. Similarly, from Eq. (B.4) , the autocorrelation of trace $u(t,k)$ is

$$\begin{aligned} r_{u_k,u_k}(\tau) &= \mathrm{E}[u(t,k)u(t+\tau,k)] \\ &= a^2(k)r_{w,w}(\tau)+r_{n_k,n_k}(\tau), \end{aligned} \tag{B.9}$$

where $r_{n_k,n_k}(\tau)$ is the autocorrelation of the noise at lag τ .

The continuous-time normalized crosscorrelation (coherence correlation) may be defined using Eq. (B.8) and Eq. (B.9) as

$$\begin{aligned} \gamma_{u_k,u_l}(\tau) &= \frac{r_{u_k,u_l}(\tau)}{\sqrt{r_{u_k,u_k}(0)r_{u_l,u_l}(0)}} \\ &= \frac{a(k)a(l)r_{w,w}[\tau-(\tau_l-\tau_k)]}{\sqrt{[a^2(k)r_{w,w}(0)+r_{n_k,n_k}(0)][a^2(k)r_{w,w}(0)+r_{n_l,n_l}(0)]}}. \end{aligned} \tag{B.10}$$

As we have already noted, the autocorrelation has its maximum value when the lag is zero; hence γ_{u_k,u_l} is a maximum for $\tau=\tau_l-\tau_k$, and the maximum value is given by

$$[\gamma_{u_k,u_l}]_M = \frac{a(k)a(l)r_{w,w}(0)}{\sqrt{[a^2(k)r_{w,w}(0)+r_{n_k,n_k}(0)][a^2(k)r_{w,w}(0)+r_{n_l,n_l}(0)]}}. \tag{B.11}$$

This is the desired result, but there remains the question of how it can be used. Let us recall that our objective is to relate the crosscorrelation to a signal-to-noise ratio, $\mathcal{R}$. Consider choice Eq. (B.3). Since the zero-lag value of the autocorrelation is no

more than the sum of squared magnitudes, it follows that

$$[\mathcal{R}]_k = \frac{\text{average absolute amplitude of the signal}}{\text{average absolute amplitude of the noise}} = a(k)\sqrt{\frac{r_{w,w}(0)}{r_{n_k,n_k}(0)}}. \tag{B.12}$$

for trace k. Combining Eq. (B.11) and Eq. (B.12) gives

$$[\gamma_{u_k,u_l}]_M = \frac{1}{\sqrt{\left[1+\frac{1}{[\mathcal{R}]_k^2}\right]\left[1+\frac{1}{[\mathcal{R}]_l^2}\right]}}. \tag{B.13}$$

Note that since

$$0 \leq [\mathcal{R}]_{k,l} \leq +\infty, \tag{B.14}$$

then

$$0 \leq |\gamma_{u_k,u_l}| \leq 1, \tag{B.15}$$

as before.

As it stands, Eq. (B.13) gives one equation and two unknowns, the two signal-to-noise ratios. One solution is that

$$[\mathcal{R}] = [\mathcal{R}]_k = [\mathcal{R}]_l; \tag{B.16}$$

That is, if the signal-to-noise ratios on traces k and l are assumed to be identical, then

$$[\mathcal{R}] = \sqrt{\frac{[\gamma_{u_k,u_l}]_M}{1-[\gamma_{u_k,u_l}]_M}}. \tag{B.17}$$

B.4 Norne Field Seismic Data Cross Correlation

We are provided sets of post-stack seismic amplitude section from Norne field, namely near-, mid-, far-, full-offset stacked data. Each stacking process uses a different

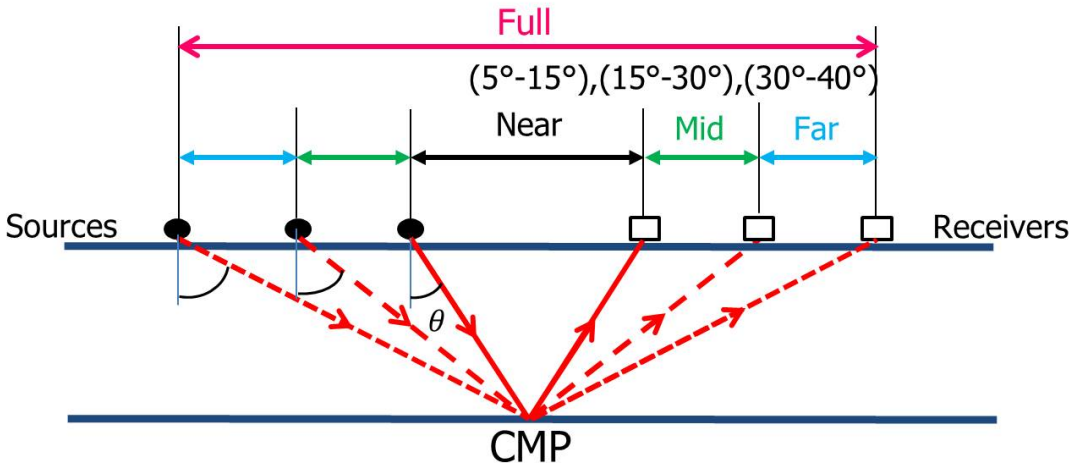

Fig. B.6—Different angle stacking data processing configurations.

distance in the offset (or incident angle) from CMP (common midpoint) gather data shown in **Fig. B.6**.

Approximate expression of transmission and reflection coefficients can be derived using, for instance, the impedance matrix formulation.

Let V_P, V_S, and ρ be arithmetic averages of velocities and densities above and below the interface, defined as follows:

$$V_P = \frac{V_{P2} + V_{P1}}{2}, \tag{B.18}$$

$$V_S = \frac{V_{S2} + V_{S1}}{2}, \tag{B.19}$$

$$\rho = \frac{\rho_2 + \rho_1}{2}. \tag{B.20}$$

If we assume that the incident and transmitting media have similar properties, the

following ratios,

$$\frac{\Delta V_P}{V_P} = \frac{V_{P2} - V_{P1}}{V_P}, \tag{B.21}$$

$$\frac{\Delta V_S}{V_S} = \frac{V_{S2} - V_{S1}}{V_S}, \tag{B.22}$$

$$\rho = \frac{\rho_2 + \rho_1}{\rho}, \tag{B.23}$$

are all much less than unity. Therefore based on the linearized Zoeppritz's equations near small angle ($\sim 30^\circ$), P-wave reflection coefficient, R_{PP}, can be approximated as (Aki and Richards 1980):

$$R_{PP} \approx \frac{1}{2}\frac{\Delta Z}{Z} + \left(\frac{1}{2}\frac{\Delta V_P}{V_P} - 2\frac{V_S^2}{V_P^2}\frac{\Delta \mu}{\mu}\right)\sin^2\theta_i, \tag{B.24}$$

where

$$\frac{\Delta Z}{Z} = \frac{\Delta \rho}{\rho} + \frac{\Delta V_P}{V_P}, \quad \frac{\Delta \mu}{\mu} = \frac{\Delta \rho}{\rho} + 2\frac{\Delta V_P}{V_P}, \tag{B.25}$$

are the relative differences change in P-wave impedance and in shear modulus respectively and θ_i is the incident wave angle. Thus, we can express Eq. (B.24) as

$$R_{PP} = A_{PP} + B_{PP}\sin^2\theta_i. \tag{B.26}$$

This means for the smaller incident angle the second term contribution becomes smaller and ultimately at the normal incident ($\theta_i = 0^\circ$), it becomes

$$R_{PP} = \frac{\rho_2 V_{P2} - \rho_1 V_{P1}}{\rho_2 V_{P2} + \rho_1 V_{P1}}, \tag{B.27}$$

which is the ratio of p-wave acoustic impedance differences to the sum of the p-wave acoustic impedance across two different rock layers.

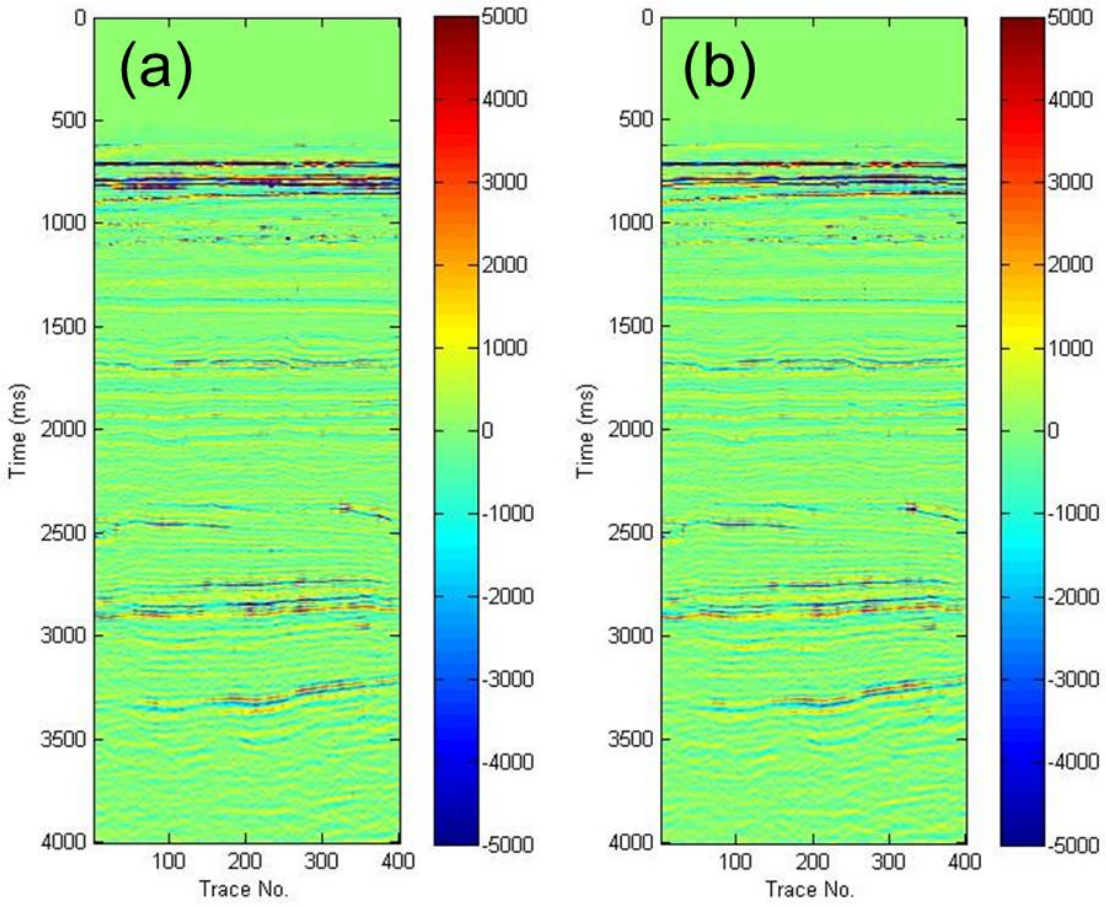

Fig. B.7—An inline slice of near-offset staked seismic amplitude data: (a) baseline survey at 2001, (b) monitoring survey at 2003.

Therefore we decided to use near-offset staked data to extract the p-wave impedance change between two surveys effectively. **Fig. B.7** shows the one inline slice of near-offset staked seismic amplitude data from base line survey at 2001 and monitoring survey at 2003. Visually, two datasets are quite similar, but the difference will be shown up in time delays from the cross correlation of two survey data shown in **Fig 8a**.

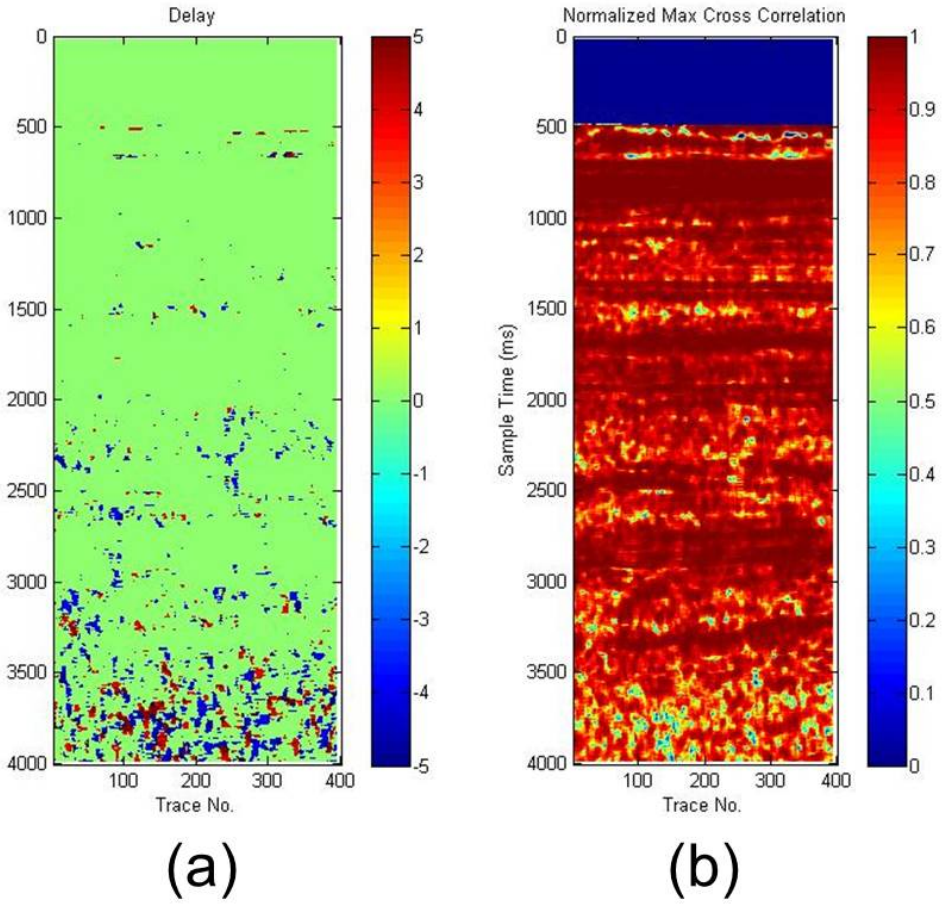

Fig. B.8—Cross correlation calculations of an inline slice of near-offset staked seismic amplitude data between baseline survey at 2001 and monitoring survey at 2003: (a) time delay (b) coherence correlation.

The window used for our computations of the coherence correlation, and subsequently for the computation of time delays between the two fields, was 16 ms $\times$ 8 traces around each point (x, t) of data. Coherent correlation is also computed and shown in **Fig. 8b**. These time shift and amplitude change can indicate the fluid saturation movement and acquisition errors between two time-lapse surveys and be utilized to improve time-lapse seismic data integration for reservoir model calibration.

APPENDIX C

SEISMIC DATA PROCESSING

Procedures of acoustic impedance mapping from seismic data of Norne field in *Petrel* (ver. 2009.2/2010.2) are as follows:

1. Input well data.

   - Well heads (\wells\well_header\norne-ntntu46-WellHeaders-only.ASC)

     DATA FORMAT:

     Wellname - X-position[m] - Y-position[m] - Total Length(measured depth)[m]

   - Well path/deviation (ex. \wells\position\norne-660810-E-2_H-PosLog.ASC)

     DATA FORMAT:

     Measure Depth: Measured Depth [m] MD: 2

     TVD-Depth: True Vertical Depth [m] TVD: 3

     TVDSS Depth: True Vertical Depth Subsea Depth [m]

     X-offset: measured from starting point(0) in x-direction [m] DX: 5

     Y-offset: measured from starting point(0) in y-direction [m] DY: 6

     Input the reference depth which is recorded in the first depth.

   - Well logs (ex. \wells\well_logs\660810-E-2H.LAS)

     DATA FORMAT:

Depth: Measured Depth [m]

TVD: True Vertical Depth [m]

TVDSS: True Vertical Depth Subsurface [m]

DT: Delta T[us(micro seconds)/ft]

DTS: Delta T Shear [us(micro seconds)/ft]

GR: Gamma Ray [API]

KLOGH: Horizontal Permeability [mD]

NPHI: Neutreon Porosity [v/v_desimal]

PHIF: Effective Fracture Porosity of Dual Porosity System [v/v_decimal]

RHOB: Bulk Density [g/cm3]

Sw: Water Saturation [v/v_decimal]

VSH: Volumetric fraction of shale [v/v_decimal]

2. Input seismic volume SEG-Y format data.

   - Survey data (ex. \SEISMIC\2001\ESEG-NORNE-2001-FULL.SGY)
   - Survey difference data (ex. \SEISMIC\Differences\ESEG-NORNE-03-01-FULL.SGY)

3. Input seismic interpretation data (horizons).

   - Top of the reservoir in time domain (\horisons\horisons\Top_Not2_2003_Time.txt) (Seisworks 3D interpretation ASCII format)
   - Base of the reservoir in time domain (\horisons\horisons\Top_Aare_2003_Time.txt)

(Seisworks 3D interpretation ASCII format)

- Oil water contact in depth domain (\horisons\horisons\bosd-4D_OWC 2001_OFFICIAL_DEPTH) (Seisworks 3D interpretation ASCII format)

4. Import average velocity data in time domain.

   - Input the file

     (time-depth-conversion\St0103_Norne_2003_depthconversion.AVF) as Petrel points with attributes (ASCII)*

     *Eliminate #comment lines and keep the check on negate depth z box.

     DATA FORMAT:

     Function ID - X-position[m] - Y-position[m] - Z-position(Time) - Average Velocity

     After inputting the value, change the attribute setting from elevation depth to elevation time. Look at the value of T and chop the data from 0 ms to 4000 ms for the reservoir part of the analysis by calculations tub in the property setting.

5. Make an interpolation 3D grid.

   Go to Processes window and click to Utilities tub.

   - Make/edit polygons

     Open a new 2D window in the top tub panel and click one seismic survey data. Create a boundary that covers the seismic area by start new rectangle button in the right tub panel.

   - Make/edit surface

Put one seismic interpretation horizon data as Input data and create surface plane by using the created polygon as boundary data and in the geometry tub click the automatic grid size and position. Copy and paste this surface to replicate for top and bottom surfaces of the 3D grid. Change the depth of the surfaces by settings of the icon and in calculations tub assign Z=0(ms) for top surface and Z=-4000(ms) for the bottom surface. Also in "More" tub, expand surfaces to the widest by clicking Expand button.

- Make simple grid

  Create new 3D grid by inserting created top and bottom surfaces in respective order in Input data tub. In Geometry tub, assign Automatic grid size (ex. 100m $\times$ 100m) and position and click OK button.

  Go to Processes window and click to Corner point gridding tub.

- Layering

  Create number of layers of 3D grid by changing the value in zone division blank and click OK. (ex. 200)

6. Scale up point velocity data to 3D grid.

   Go to Processes window and click to Property modeling tub.

   - Scale up well logs Input point attribute of seismic average velocity data as V_{ave}.

7. Interpolate average velocity in 3D grid.

   Go to Processes window and click to Property modeling tub.

   - Petrophysical Modeling Input upscaled seismic average velocity data. Choose

method for interpolation as Moving average with default parameters and click OK. Change the property template as average velocity.

8. Make a velocity model with interpolated velocity 3D grid.

   Go to Processes window and click to Geophysics tub.

   - Make velocity model

     Create new Velocity model that converts time domain to depth domain. Insert top and bottom surfaces as Base column and input average property of interpolated velocity 3D grid and click OK.

9. Time to Depth conversion of seismic volume data by the created velocity model.

   Go to Processes window and click to Geophysics tub.

   - Volume attributes

     Select the tub to "Depth conversion methods" and click "General depth converter". In input/output tub, select Realize and input the seismic volume data z and in parameters tub, input the created velocity model and interpolation is smooth and the direction is forward and click OK. Right click on the converted seismic volume object and click Insert virtual cropped volume to crop the domain for the inversion calculation by cropping the depth in the settings (ex. [-2300 $\sim$ -3200]).

10. Genetic inversion of acoustic impedance volume with converted seismic volume and global well log.

    - Acoustic impedance calculation from global well log

      Right click on the Global well logs object under wells input, create acoustic impedance by checking on density log and sonic log boxes and click OK.

Notice the unit is KPa.s/m.

Go to Processes window and click to Geophysics tub.

- Volume attributes

  Select the tub to “Stratigraphic methods” and click “Genetic inversion”. In input/output tub, select Realize and input the cropped seismic volume data and in parameters tub, input the seismic cube and well folder of well logs (only well logs with density log and sonic log and eliminate others) and calculated acoustic impedance to global well log blank and with following default parameters and click OK.

11. Map the acoustic impedance volume on reservoir model.

    Go to Processes window and click to Property modeling tub.

    - Geometrical Modeling

      Create new property by setting “Seismic resampling” as Select method and property template is “Seismic(default)”. And input Acoustic impedance volume and Quality tub as “Exact” and Average method as “Arithmetic” and click OK.

12. Smoothing operation.

    Copy the generated the acoustic impedance maps as original results under properties object. Double click the copied object. And go to Operation tab and expand Property operations. And click Smooth icon and chose as many iterations as you want in the below box to smooth the property values.

13. Output the results.